



**HAL**  
open science

**Mesures de télédétection satellitaires appliquées à la  
sismotectonique, à la bathymétrie, au volcanisme.  
Mémoire d'Habilitation à Diriger des Recherches**

Marcello de Michele

► **To cite this version:**

Marcello de Michele. Mesures de télédétection satellitaires appliquées à la sismotectonique, à la bathymétrie, au volcanisme. Mémoire d'Habilitation à Diriger des Recherches. Geophysics [physics.geo-ph]. Ecole Normale Supérieure de Paris - ENS Paris, 2018. tel-02375885

**HAL Id: tel-02375885**

**<https://brgm.hal.science/tel-02375885>**

Submitted on 22 Nov 2019

**HAL** is a multi-disciplinary open access archive for the deposit and dissemination of scientific research documents, whether they are published or not. The documents may come from teaching and research institutions in France or abroad, or from public or private research centers.

L'archive ouverte pluridisciplinaire **HAL**, est destinée au dépôt et à la diffusion de documents scientifiques de niveau recherche, publiés ou non, émanant des établissements d'enseignement et de recherche français ou étrangers, des laboratoires publics ou privés.

BRGM, Orleans  
Ecole Normale Supérieure, Paris

**Mesures de télédétection satellitaires appliquées à la sismotectonique,  
à la bathymétrie, au volcanisme**

Mémoire d’Habilitation à Diriger des Recherches

**Marcello de Michele, Phd**

BRGM, 3 av. C. Guillemin, 45000, Orléans

Redaction du 18 janvier 2018

Avis favorable du Conseil Scientifique de l’Ecole Normale Supérieure, Paris, le 09 Avril 2018

Habilitation soutenue le 05 novembre 2018 à l’Ecole Normale Supérieure de Paris  
en face d’une Jury composé par :

Pierre Briole, CNRS/ENS (F) .....	Correspondant HdR
Remi Michel, CEA (F) .....	Rapporteur / President du Jury
Riccardo Lanari, CNR/IREA (I).....	Rapporteur
Freysteinn Sigmundsson, University of Reykjavik (IS) .....	Rapporteur
Juliette Lambin, CNES (F) .....	Examinatrice
Tim Wright, University of Leeds (UK) .....	Examineur

“Color is only beautiful when it means something.”

## Remerciements

Je tiens à remercier tous les collègues et coauteurs qui ont participé et contribué à ce travail. Je souligne le cran de certains, qui ont été suffisamment ouvert d’esprit pour me suivre sur quelques-uns des sujets précurseurs présentés dans ces documents. Un clin d’œil à mes deux co-inventeurs Deborah Idier et Daniel Raucoules. Je remercie le BRGM pour avoir soutenu financièrement et intellectuellement la démarche d’Habilitation, notamment Gilles Grandjean et Jean Christophe Gourry. Je remercie l’Ecole Normale Supérieure de Paris, notamment Pierre Briole, pour avoir accepté d’accompagner ce projet et avoir fourni le cadre intellectuel et administratif pour bien le mener. Je remercie les étudiants que j’ai eu l’honneur d’accompagner et encadrer, Guillaume Bacques, Claudio Trovato, Adrien Poupardin, Yann Gueguen, Nadia Khezami et Konstantinos Derdelakos, dont les travaux sont résumés dans ce manuscrit : à leurs côtés j’ai appris beaucoup de choses, humainement et scientifiquement, à travers leur travail. Je tiens à remercier les membres du jury, Juliette Limbin, Tim Wright, Remi Michel, Riccardo Lanari et Freysteinn Sigmudsonn pour l’évaluation élogieuse de mon manuscrit d’habilitation et la discussion scientifique encourageante qui a suivi la soutenance orale. Une pensée va aux amis et à la famille qui étaient présents lors de la soutenance orale et à ma compagne Carole dont le soutien sans faille va au-delà du domaine scientifique.

## Résumé

Ce document résume mon parcours scientifique et mes recherches dans le domaine de la télédétection satellitaire appliquée à la Terre Solide. Ce document est rédigé à titre de mémoire d’Habilitation à Diriger des Recherches auprès de l’Ecole Normale Supérieure de Paris, France. Ce document est rédigé en anglais pour permettre une relecture auprès d’un jury international.

In this manuscript I present part of my work dedicated to the study of kinematic processes related to seismo tectonics and, more broadly, to the study of geological phenomena related to solid Earth, from space. In my work I mainly used Synthetic Aperture Radar (SAR) and optical sensors onboard satellite platforms. Since the beginning of my work as a scientist, my research is shared between methodological developments and the understanding of the geophysical processes behind the measurements. In this manuscript, I present a review of my scientific education, my involvement in different research projects, the background questions that push my research and the tools that I used to observe, to measure and to interpret. I also describe the work of PhD students, which research activities I had the opportunity to co-supervise. I also try to give some personal ideas of future research activities and a vision of future methodological developments related to my field of work.

## TABLE of CONTENTS

### 1. INTRODUCTION

#### 1.1 WHICH ARE THE INSTRUMENTS and TECHNIQUES THAT I USED

##### 1.1.1 Subpixel correlation technique – offset tracking

###### 1.1.1.1 Optical Domain

###### 1.1.1.2 SAR Domain

### 2. CURRICULUM VITAE

### 3. SYNTHESIS of my SCIENTIFIC ACTIVITY

#### 3.1 Mémoire de synthèse

#### 3.2 Research and applied research

##### 3.2.1 International Charter on Space and Major Disasters & Cellule d’Intervention et expertise Scientifique et Technique

##### 3.2.2 European funded projects, within the 6<sup>th</sup> and 7<sup>th</sup> framework program for research and development.

##### 3.2.4 ESA funded projects

##### 3.2.5 Some of the BRGM research framework programs, 100% funded by BRGM

#### 3.3 PhDs, POSTOCS, INTERNSHIP SUPERVISION.

### 4. PRESENTATION and PERSPECTIVES of MY RESEARCH WORK

#### 4.1 introduction

#### 4.2. Article n°1 **Volcanic Plume Elevation Model and its Velocity Derived From Landsat 8**

#### 4.3. Article N°2 **Synthetic Aperture Radar (SAR) Doppler anomaly detected during the 2010 Merapi (Java, Indonesia) eruption**

#### 4.4. Article N°3 **Revisiting the shallow Mw 5.1 Lorca earthquake (southeastern Spain) using C-band InSAR and elastic dislocation modelling**

#### 4.5. Article n°4 **Direct measurement of ocean waves velocity field from a single SPOT-5 dataset**

#### 4.5. Article n°5 **Water depth inversion from a single SPOT-5 dataset**

### 5. PERSPECTIVES

### 6. CITED BIBLIOGRAPHY

## 1. INTRODUCTION

Over two past decades, the advances in new space based geodetic tools have supported the investigations of the kinematics, structure, and dynamics of the solid Earth. In this field, the rapid technological change has fostered new interdisciplinary research opportunities. This keeps on going even today. Remote sensing applications to Geodesy have grown; I had the extraordinary opportunity to grow with it and to participate to accompany the development of some applications in a range of scientific fields. My field of applications ranges from crustal deformation mapping and modelling, to bathymetric mapping from space up to the measurements of the height and speed of a volcanic cloud from space. In my published work, I try to concentrate both on the development of new techniques (or methodologies) and to the geophysical interpretations that benefit from that development. This document aims at reviewing new and emerging research activities I have been involved in the last 15 years. This document also summarizes few keys areas where, in my opinion, additional research is still needed to further improve our understanding of dynamic systems within the solid earth, atmosphere and hydrosphere, related to my field of study.

In the following paragraphs, I summarize some of the challenges addressed in my past and present work.

### **How do tectonic plates deform?**

The advent of space geodesy improved our capability of measuring ongoing deformation of the Earth crust at a millimeter level across global scale distances. This technical breakthrough enabled the measurements of neo-tectonic processes across and between continents, with precision. With investigations made at a variable spatial and temporal scale, we have been able to detect deformation in some areas of plate interiors, previously thought as stable. Furthermore, the accommodation of relative plate motion at plate boundaries involves considerable complexity, with fault slipping irregularly in time during large earthquakes, along with the recognition and characterization of post seismic strain and a variety of other transient deformation phenomena.

### **Can we precisely measure the height of a volcanic cloud and what physical process controls the injection height and the speed of a volcanic plume ?**

Volcanic eruptions have an impact on society. This includes changing temporally the global climate patters, shutting down airports and destruction of life and properties. The retrieval of both height and velocity of a volcanic plume is an important issue in volcanology. As an example, it is known that large volcanic eruptions can temporarily alter the climate, causing global cooling and shifting precipitation patterns; the ash/gas dispersion in the atmosphere, their impact and lifetime around the globe, greatly depends on the injection altitude. Plume height information is critical for ash

dispersion modelling and air traffic security. Furthermore, plume height during explosive volcanism is the primary parameter for estimating mass eruption rate. The plume altitude is also important to retrieve the amount of SO<sub>2</sub> concentration from dedicated spaceborne spectrometers.

**Will we be able to map tectonic fault motion under water and can we measure differential bathymetry ?**

Seventy five percent of Earth crust lies under water and it is thus unobservable using the electromagnetic energy employed by spaceborne remote sensing techniques. However, since coastal bathymetry controls swell celerities and swell wavelengths, and since we are able to measure swell celerities and swell wavelength from quasi synchronous optical satellite images, we can potentially retrieve coastal bathymetry from space, indirectly. At least up to ~100 meters depth. Therefore, potentially, the answer to this challenge is “yes”. After the discovery of a measurable baseline and a time lag between the panchromatic bands and the multispectral bands of virtually every optical (multispectral) spaceborne system, we exploited this lag to measure swell velocity from space. This led us to present a potential new technique for retrieving bathymetry from space. Many applications are foreseen, the one I am more interested in is shallow seafloor geodesy (or differential bathymetry) applied to seismotectonics. My vision is that one day we would be able to map bathymetry kinematics from space with precision, which is of great importance as many geological phenomena occur under water.

1.1 WHICH ARE THE INSTRUMENTS and TECHNIQUES THAT I USED:

In the last 20 years, remote sensing methods of ground displacement based on Differential Radar Interferometry (DInSAR) and on the optical and radar image correlation allowed on the one hand to contribute to confirm the theory of Plate Tectonics and on the other to improve our knowledge about the mechanisms that deform the Earth. This is of course in complement with Global Positioning System (GPS), which I am not writing about here as it is not my principal research tool.

As a detailed technical review of InSAR concepts exceeds the scope of the present document, we suggest the reader to refer to specialized literature (e. g. Massonnet et al., 1993; Massonnet and Feigl, 1998; Hanssen, 2001; Hooper, 2006, Ferretti et al., 2001) for a technical review of the SAR instrument, systems, SAR interferometry algorithms and image formation concepts. We describe below just the few concepts, mainly borrowed from Hanssen (2001) and Hooper (2006) that would help the non-specialized reader to familiarize with the very basics of SAR and understand the findings described further in this manuscript.

A Synthetic Aperture Radar (SAR) system can be seen as an extension of the classical Radio Detection and Ranging (radar) systems; it employs both the pulse compression techniques and the synthetic aperture concept that enable the data spatial resolutions to be improved by the order of meters (instead of kilometers) with relatively small physical antennas. Compared to visible remote sensing, the radar has several advantages; it is an active system (so data acquisition does not depend on the daylight); radar waves pass through clouds, which makes the SAR a potentially «all weather» instrument. Space-borne SAR instruments were initially used for the investigation of planetary surfaces with the first Earth orbiting SAR instrument launched in 1978, aboard the NASA (National Aeronautics and Space Administration) SEASAT satellite. The launch of the ESA (European Space Agency) satellite ERS-1 in 1991, led to a large amount of SAR data available for InSAR and made InSAR widely applicable. SAR systems operate with a side-looking geometry and illuminate the Earth with a series of microwave pulses and record the phase and amplitude of echoes of previous pulses, scattered from the Earth. The raw data collected by the SAR is then focused to form an «image» or «scene». Each time the spacecraft passes over a specific area it can acquire a «scene». The data focusing is achieved in the direction perpendicular to the flight direction (the range direction) through knowledge of the time delay, and in the flight direction (the azimuth direction) through combination of echoes from multiple locations to synthesize a large antenna aperture (i. e. the synthetic aperture concept). Focusing is based on the consideration (the compression process) of the frequency modulation in a given bandwidth both in range and azimuth directions. In range direction, both the bandwidth and the frequency variation that make compression possible are provided by the nature of the emitted pulse (i.e. the design of the instrument) and the frequency is linearly modulated. Whereas in azimuth direction, bandwidth and frequency variation are naturally provided by the Doppler generated by the movement of the sensor relative to the Earth.

The basic concept of differential SAR interferometry (InSAR) can be summarized as the phase differences of the radar waves between multiple radar scenes. For our researches, the main objective of SAR interferometry is to estimate the deformation field occurring on the surface of the Earth between two radar acquisitions. Given exactly the same data acquisition geometry (the orbital baselines are supposed to be very small respect to the satellite-earth distance), the phase differences between multiple radar scenes acquired over the same area is proportional to a number of physical phenomena such as ionospheric or tropospheric waves refraction (resulting in signal phase delay), random changes of the earth surface, ground surface movements and noise. In seismotectonics, we are interested in the InSAR signal due to ground surface movements. Therefore, we will try to model the undesired signals and remove them from the interferometric phase, after which we can use the SAR system to create maps and time series of surface displacements. Many algorithms have been

proposed as each study area has to be treated as a case-study depending on the geographic area and local atmospheric properties and conditions.

### 1.1.1 Subpixel correlation technique – offset tracking

Image correlation techniques represent a valuable complement to Differential Synthetic Aperture Radar Interferometry (DInSAR) for monitoring Earth surface displacements. In particular, near fault/fracture zones where large displacement results in poorly coherent SAR signal. This technique has been successfully applied using SAR amplitude images and satellite/airborne photos in different fields of study. In particular, in seismotectonics (e. g. Van Puymbroeck et al. 2000; Michel & Avouac 1999; Michel & Avouac 2002; Dominguez et al. 2003, Binet & Bollinger, 2005; Fialko et al. 2005, Klinger et al., 2006; Michel & Avouac, 2006, de Michele et al., 2010 ), on volcano deformation (Tobita et al. 2001, de Michele and Briole, 2007) and gravitational movements assessment (e.g. Delacourt et al. 2004; Berthier et al. 2005 ; Raucoules et al., 2013). Recently, we push this methodology forward by applying it to quasi synchronous sub-band multispectral images to measure ocean swell celerity (de Michele et al., 2012) and to extract digital elevation models of volcanic plumes (de Michele et al., 2016). Image correlation technique relies on the statistical analyses of two sets of data (e.g. digital satellite imagery). This technique matches two or more images at each point on a grid analyzing the degrees of local correlation at each step. Differences in the local instantaneous frequency of the images result in sub-pixel spatial differences in ground patterns (e. g. Crippen, 1992). The results are an expression of both movements in the ground surface and image distortions. Sources of image distortions are discussed in Van Puymbroeck et al. (2000), Michel & Avouac (2006) and Leprince et al. (2007). They can be potentially modelled and removed so that ground surface displacements can be highlighted and measured with high precision. Measurements must be performed with subpixel accuracy, because the amplitude of the ground displacement -a few meters for large earthquakes- is typically lower than the resolution of the images except for new generation HRV sensors with improved spatial resolution and air-photos.

#### 1.1.1.1 Optical domain

Sub-pixel image correlation technique for measuring ground surface displacements was firstly conceptualized by Robert Crippen (1992) and applied to satellite visible imagery. Crippen (1992) gave the technique the name of “imageodesy”. The premise of the method is that extensive, sub-resolution spatial differences in ground patterns between images acquired at differing times can be measured accurately to high precision and also can be distinguished from systematic image

differences, such as those due to sensing-system attitude variations. If each pixel value is a measure of radiance weighted at sub-resolution scales by the point-spread function that is imposed by the atmosphere and sensor optics, each pixel value is, therefore, variable in relation to its geographic position at sub-resolution scales and thereby indirectly measures geographic position.

The images should be previously resampled to the DEM geometry so that they are in a common cartographic projection but recently some other methodologies are being proposed if a precise DEM is not available, such as the three pass image correlation (de Michele et al., 2008) and the use of the perpendicular-to-the-epipolar-plane images (Renaud Binet, personal communication). Residual offsets remain that relate to residual uncertainty in estimates of satellite parameters, errors in DEM (if a DEM is used), and deformation induced by earthquakes. Those offsets are characterized by gradients typically lower than 0.1% except within a few tens of meters of faults (Michel & Avouac, 2006). For more technical details on the methodology we suggest the reader to refer to the pioneering work of Van Puymbroek et al., 2000 or Leprince et al., 2007. The latter, within the Californian Institute of Technology, develop and maintain dedicated software for optical image correlation.

#### 1.1.1.2 SAR domain

Sub-pixel image correlation technique for measuring ground surface displacements can be applied to SAR amplitude images. The main differences are due to the radar acquisition geometry so that instead of having East-West and North-South offsets, one must deal with slant range offsets and Azimuth offset. This is in a way intriguing as azimuth offset are «topography free» and slant range offsets are calculated in the Line Of Sight (LOS) of the satellite and therefore contains a contribution from vertical offsets depending on the viewing angle. For details on this methodology, also called “offset tracking” in literature, we suggest the reader to look at Michel & Rignot (1999) and Michel et al., (1999), who used it with SIR-C (L-band; SIR is Shuttle Imaging Radar) and European Remote-Sensing Satellite (ERS) radar amplitude images. The technique of offsets provides a measurement of the ground displacement from the analysis of the geometrical deformation between the two SAR amplitude images. Usually SAR images with a small as possible baseline are chosen in order to reduce the stereoscopic effect and geometric decorrelation. In the studies presented in the present work, we estimate the range and azimuth offset fields using cross correlation optimization of the input intensity images. This algorithm is implemented in the GAMMA software with the name of «offsets tracking» (Strozzi et al., 2002).

Le dossier qui suit, représente le dossier scientifique comprenant :

Chapter 2. CV détaillé

Chapitre 3. Mémoire de synthèse original (parcours et travaux, responsabilités collectives, conférences)

Chapitre 4. Résumé des cinq productions les plus significatives

Chapitre 5. Un projet de recherches à quatre ans (4 pages maximum)

Chapitre 6. Un exemplaire des travaux scientifiques publiés ou inédits (sur cle USB)

## 2. CURRICULUM VITAE

I was born in Milan, Italy, the 4th of May 1973.

### **My education:**

January 2009 - November 2010

**Université Pierre et Marie Curie, Paris VI, ED-398**, Paris (France). PhD, “Observations Sismo-tectoniques par Télédétection”. Laboratoires d’accueil : Ecole Normale Supérieure de Paris (ENS), UPMC et BRGM.

October 2001- October 2002

**University College London, Imperial College of Science Technology and Medicine**, London (UK). Master of Science (M.Sc.) en télédétection satellitaire et traitement d’images.

October 1992 - March 2000

**Università degli studi di Pavia**, Italy. ‘Laurea’ (Master2) in Geological Sciences. Specialization : petrography, mineralogy and volcanology.

October 1987 - June 1992

**Liceo scientifico ‘Luigi Cremona’**, Milan, Italie. Scientific Baccalauréat (high school diploma).

### **Synthesis of my working records**

November 2005 - today

**Bureau de Recherche Géologiques et Minières (BRGM)**, Orléans, France. Researcher/engineer, expert in satellite remote sensing.

May – July 2005

**Institut de Physique du globe de Paris (IPGP), UMR CNRS 7531**, Paris, France. Synthetic Aperture Radar engineer.

November 2004 - February 2005

**T.R.E. (Telerilevamento Europa, S. r. l.)**, Milan, Italy. Remote sensing engineer

May 2004

**Institut de Physique du globe de Paris (IPGP), Laboratoire Physique e Chimie des Systèmes Volcaniques**, Paris, France. In the frame of UN-OCHA Nyiragongo Relief Fund project, remote sensing engineer.

December 2002 - December 2003

**Institut de Physique du globe de Paris (IPGP), UMR CNRS 7531**, Paris, France.

Remote sensing engineer in the frame of CNES-CNRS project « Space volcanoes Observatory » (SVO) and ROBOVOLC (6<sup>e</sup> PCRD).

#### **Administrative responsibilities:**

Work Package (WP) Leader, project Aphorism (Advanced Procedures for Volcanic and Seismic Monitoring), Seventh Framework Program of the European Commission. WP 2 leader « User requirements and integrated product definition », 2013-2016.

Project leader (BRGM) for the French ANR (Agence Nationale de la Recherche) project KalHAITI « a database for research, risk management and sustainable reconstruction in Haiti. », 2011-2015.

Project Leader (BRGM) for the French projet CENdReS « Calcul de modèles numériques d’Elévation des Nuages de cendres volcaniques Depuis une Restitution Satellitaire : Plume Elevation Models (PEMs) ». 2017.

Project leader for the ESA-BRGM project Bathysent « water depth inversion from Sentinel 2 data ». 2018. ESA/AO/1-9101/17/I-NB EO Science For Society Permanently Open Call For Proposals, grant n°4000124021/18/I-NB.

#### **Member of Scientific Committees**

Ciest, Cellule d’intervention scientifique et technique, 2006-2010.

Pole Nationale “Terre Solide” Form@ter. French National Solid Earth Group. Member of the scientific board (2014-2017).

MIST, French GDR (Groupe de Recherche en construction). National research group on volcanic plumes. Member of the scientific board. Since 2017

Geohazards Office. ESA-CNES-BRGM funded bureau on geohazards. Member of the scientific board. 2018-2020.

### PhD and Post Doc co-supervision

Guillaume Bacques, « Étude de variations spatio-temporelles de glissements asismiques le long de failles majeures par Interférométrie RADAR Différentielle satellitaire : Cas du séisme lent de 2009-2010 de Guerrero (Mexique) - Cas de la déformation postsismique suite au séisme de Parkfield (2004, Mw6, Californie) ». PhD supervisor : Fabrice Cotton, Université de Grenoble (France). PhD funded by CNES and BRGM. PhD defended in 2013.

Claudio Trovato, « Séismes à Longue Période (LP) sur le Mt. Etna (Italie): inversion du tenseur des moments et incertitudes liées à leur interprétation ». PhD supervisor: Hideo Aochi, BRGM, and Bruno Scaillet, Institut de Science de la Terre d’Orléans, France. PhD funded by Marie Curie EU program NEMO and BRGM. PhD defended in 2015.

Yann Gueguen, « Etude des mouvements de surface en environnement minier à partir d'interférométrie radar et identification des origines des déformations : l'exemple du bassin Nord/Pas-de-Calais ». PhD supervisor : Benoit Deffontaine, Université Marne-la-Vallée (France). PhD funded by CIFRE and Charbonnage de France. PhD defended in 2008.

Adrien Poupardin, “water depth inversion from a single spot 5 dataset”. Postdoc funded by BRGM and Institut Carnot. 2014

### Publications (peer reviewed)

*Theme: ocean*

A. Poupardin, D. Idier, **M. de Michele**, D. Raucoules Water depth inversion from a single SPOT-5 dataset, *IEEE Transactions on Geoscience and Remote Sensing*, 54, 4. (2016), pp. 2329–2342.

A. Poupardin, D. Idier, **M. de Michele**, D. Raucoules, Method for determining bathymetry from quasi-synchronous optical satellite images, *PATENT WO 2016132068 A1* (2015).

**de Michele M.**, Leprince S., Thiebot J., Raucoules D., Binet R., Direct measurement of ocean waves velocity field from a single SPOT-5 dataset, *Remote Sensing of Environment*, 119, 266-271 (2012).

*Theme: seismo tectonics*

**de Michele M**, Ergintav S, Aochi H, Raucoules D (2017). An L-band interferometric synthetic aperture radar study on the Ganos section of the north Anatolian fault zone between 2007 and 2011: Evidence for along strike segmentation and creep in a shallow fault patch. *PLOS ONE* 12(9): e0185422.

Bacques G., **de Michele M.**, Raucoules D., Hideo Aochi H., Rolandone F., (2018), Shallow deformation of the San-Andreas fault 5 years following the 2004 Parkfield earthquake (Mw6) combining ERS2 and Envisat InSAR, *Scientific Reports*, volume 8, Article number: 6032, doi:10.1038/s41598-018-24447-3.

**de Michele M.**, P. Briole, D. Raucoules, A. Lemoine, and A. Rigo (2013), Revisiting the shallow Mw 5.1 Lorca earthquake (southeastern Spain) using C-band InSAR and elastic dislocation modelling, *Remote Sens. Lett.*, 4(9), 863–872.

Barbot, S., P. Agram, and **M. de Michele**, "Change of Apparent Segmentation of the San Andreas Fault Around Parkfield from Space Geodetic Observations Across Multiple Periods." *Journal of Geophysical Research: Solid Earth*, 118, 12 (2013).

Parker, R. N., Densmore, A. L., Rosser, N. J., **de Michele, M.**, Yong, L., Runqiu, H., Whadcoat, S., Petley, D. N., Mass wasting triggered by the 2008 Wenchuan earthquake greater than orogenic growth, *Nature Geoscience*, 10.1038/NGEO1154 (2011).

**de Michele M.**, Raucoules D., Salichon J., Lemoine A., Aochi H., Spatiotemporal evolution of surface creep in the Parkfield region of the San Andreas Fault (1993- 2004) from Synthetic Aperture Radar, *Earth and Planetary Science Letters*, 308, 141-150 (2011).

Raucoules, D., Ristori, B., **de Michele, M.**, Briole, P., Surface displacement of the  $M_w$  7 Machaze earthquake (Mozambique): Complementary use of multiband InSAR and radar amplitude image correlation with elastic modelling, *Remote Sensing of the Environment*, 114, 10, 2211-2218 (2010).

**de Michele M.**, D. Raucoules, J. de Sigoyer, M. Pubellier, N. Chamot-Rooke, Three-dimensional surface displacement of the 12 May 2008 Sichuan earthquake (China) from Synthetic Aperture Radar: evidences for rupture on a blind thrust, *Geophysical Journal International*, 183, 3, 1097-1103 (2010).

**de Michele M.**, D. Raucoules, C. Lasserre , E. Pathier ,Y. Klinger, J. Van Der Woerd , J. de Sigoyer , X. Xu., The Mw 7.9, 12 May 2008 Sichuan earthquake rupture measured by sub-pixel correlation of ALOS PALSAR amplitude images, *Earth Planets and Space* , doi:10.5047/eps.2009.05.002 (2010).

**de Michele M.**, D. Raucoules, H. Aochi, N. Baghdadi and C. Carnec, Measuring coseismic deformation on the northern segment of the Bam-Baravat escarpment associated with the 2003 Bam (Iran) earthquake, by correlation of very-high-resolution satellite imagery, *Geophysical Journal International*, 173, 459–464, doi: 10.1111/j.1365-246X.2008.03743.x (2008).

*Theme: volcanology*

**de Michele, M.**, D. Raucoules, and P. Arason (2016), Volcanic plume elevation model and its velocity derived from Landsat 8, *Remote Sens. Environ.*, 176, 219–224.

Bignami, C., Corradini, S., Merucci, L., **de Michele, M.**, Raucoules, D., De Astis, G., Stramondo, S., Piedra, J., Multisensor Satellite Monitoring of the 2011 Puyehue-Cordon Caulle Eruption . *IEEE Selected Topics in Applied Earth Observations and Remote Sensing* ,7, 7 (2014).

**de Michele, M.**, Raucoules, D., Wegmuller, U., Bignami, C., Synthetic Aperture Radar (SAR) Doppler Anomaly Detected During the 2010 Merapi (Java, Indonesia) Eruption., *IEEE Geoscience and Remote Sensing Letters*, 10, 6 (2013)

**de Michele, M.**, Briole, P., Deformation between 1989 and 1997 at Piton de la Fournaise volcano retrieved from correlation of panchromatic airborne images, *Geophysical Journal International*, 169, 357–364 (2007).

N. Houlié , J.C. Komorowski M., **de Michele M.**, Kasereka, H. Ciraba, Early detection of eruptive dykes revealed by normalized difference vegetation index (NDVI) on Mt. Etna and Mt. Nyiragongo, *Earth and Planetary Science Letters*, 246 , 231–240 (2006).

J-C Komorowski, M Halbwegs , M. Kasereka, B. Balupu, P. Briole, J-C Dupin, N. Houlié, H. Hamaguchi, A. Lemarchand, J. Lockwood , Y. Mapendano, C. Mateso , A. Mbilizi, **M. de Michele**, F. Munyololo, C. Newhall, L. N’Yombo Watuk, J. Ruch, M. Serugendo, M. Tuluka, M. Wafula (2004). The January 2002 flank eruption of Nyiragongo volcano (Democratic Republic of Congo): chronology, evidence for a tectonic rift trigger, and impact of lava flows on the city of Goma. *Acta Vulcanologica*, Vol. 14 (1-2), 2002 and Vol. 15 (1-2) 2003, 27-61 (2004).

*Theme: land subsidence*

Woppelmann, G., Le Cozannet, G., **de Michele, M.**, Raucoules, D., Cazenave, A., Garcin, M., Hanson, S., Marcos, M., Is land subsidence increasing the exposure to sea level rise in Alexandria, Egypt?. *Geophysical Research Letters*, American Geophysical Union, 2013, 40 (12), pp.2953-295

Gueguen, Y., Deffontaines B., Fruneau, B., Al Heib, M., **de Michele, M.**, Raucoules, D., Guise, Y., Planchenault, J., Monitoring residual mining subsidence of Nord/Pas-de-Calais coal basin from differential and Persistent Scatterer Interferometry (Northern France), *Journal of Applied Geophysics*, 69, 1, 24-34 (2009).

*Theme: methodology*

Raucoules, D., **de Michele, M.**, Malet, J.-P., Ulrich, P. Time-variable 3D ground displacements from high-resolution synthetic aperture radar (SAR). Application to La Valette landslide (South French Alps). *Remote Sens. Environ* 2013, 139, 198–204.

Raucoules D., Raffard D., Rohmer J., Loschetter A., **de Michele M.**, and Yann Le Gallo, Potential of diffuse scatterer interferometry for monitoring CO2 storage sites in European contexts (land cover types), *International Journal of Remote Sensing*, 36:11, 2800-2815, DOI: 10.1080/01431161.2015.1043158 (2015).

Raucoules D., **de Michele M.**, Assessing ionospheric influence on L-band SAR data: Implications on co-seismic displacement measurements of the 2008 Sichuan Earthquake, *IEEE Geoscience and Remote Sensing Letters*, 7, 2, 286-290 (2010).

Raucoules D., B. Bourguin, **M. de Michele**, G. Le Cozannet, L. Closset, C. Bremmer, H. Veldkamp, D. Tragheim, L. Bateson, M. Crosetto, M. Agudo, M. Engdahl, Validation and intercomparison of Persistent Scatterers Interferometry: PSIC4 project results, *Journal of Applied Geophysics*, 68, 335–347 (2009).

**Proceedings in Conferences**

**Marcello de Michele**, Daniel Raucoules, Guillaume Bacques, Sylvain Barbot, Pyiush Agram, Frederique Rolandone, and Pierre Briole. 20 years of InSAR observations on the Parkfield-Cholame section of the San Andreas Fault (California, USA): insights on the behavior of a transition zone. In

EGU General Assembly 2014, Vienna, Austria, April 2014. URL <https://hal-brgm.archives-ouvertes.fr/hal-00952247> (**Invited**).

Daniel Raucoules, **Marcello de Michele**, and Bertrand Aunay. Landslide motion observation on la Reunion Island (Indian ocean) seen by ALOS-2/PALSAR-2 based on image correlation techniques and SAR interferometry. In FRINGE 2017, Helsinki, Finland, June 2017a. URL <https://hal-brgm.archives-ouvertes.fr/hal-01507082>.

Daniel Raucoules, Goneri Le Cozannet, Cyril Poitevin, **Marcello de Michele**, and Guy Woppelmann. Observation of ground surface deformation in coastal areas by SAR Interferometry . In ISRSE 37, Tshwane, South Africa, May 2017b. URL <https://hal-brgm.archives-ouvertes.fr/hal-01463068>.

**Marcello de Michele**, Daniel Raucoules, Stefano Corradini, and Luca Merucci. The Use of High Resolution Pleiades Images to Extract Volcanic-Cloud Top Heights and Plume Elevation Models: examples on Mount Etna (Italy) and Mount Ontake (Japan). In European Geoscience Union General Assembly 2017, volume 19, pages 2017 – 15308, Vienne, Austria, April 2017. URL <https://hal-brgm.archives-ouvertes.fr/hal-01482699>.

**Marcello de Michele**. L band InSAR study on the Ganos section of the North Anatolian Fault Zone (NAFZ). In European Geoscience Union 2016, Vienna, Austria, April 2016. URL <https://hal.archives-ouvertes.fr/hal-01292567>.

**Marcello de Michele**, Daniel Raucoules, Porur Arason, Claudia Spinetti, Stefano Corradini, and Luca Merucci. Volcanic Plume Elevation Model Derived From Landsat 8: examples on Holuhraun (Iceland) and Mount Etna (Italy). In European Geoscience Union, Venna, Austria, April 2016. URL <https://hal.archives-ouvertes.fr/hal-01292575>.

Daniel Raucoules, Guy Woppelmann, Goneri Le Cozannet, and **Marcello de Michele**. Use of Differential SAR Interferometry for vertical ground motions monitoring in coastal cities. In Our Common Future under Climate Change (CFCC) Conference : International scientific conference, Paris, France, July 2015. URL <https://hal-brgm.archives-ouvertes.fr/hal-01196634>.

**Marcello de Michele**, Daniel Raucoules, and Christian Minet. Spaceborne Synthetic Aperture Radar (SAR) Doppler anomalies due to volcanic eruption induced phenomena. In EGU 2015, General

Assembly, Vienne, Austria, April 2015. European Geosciences Union. URL <https://hal-brgm.archives-ouvertes.fr/hal-01120980>.

Jeremy Rohmer, Annick Loschetter, Daniel Raucoules, **Marcello de Michele**, Yann Le Gallo, and Damien Raffard. Improving Persistent Scatterers Interferometry (PSI) analysis in highly vegetal / agricultural areas for long term CO<sub>2</sub> storage monitoring. In 12th Greenhouse Gas Control Technologies conference : GHGT12, Austin, United States, October 2014. URL <https://hal-brgm.archives-ouvertes.fr/hal-00999538>.

**Marcello de Michele**, Jeremy Rohmer, Daniel Raucoules, Annick Loschetter, Y. Le Gallo, and Damien Raffard. Limits, complementarity and improvement of Advanced SAR Interferometry monitoring of anthropogenic subsidence/uplift due to long term CO<sub>2</sub> storage. In AGU Fall meeting 2013, page `a suivre, San Francisco, United States, December 2013a. URL <https://hal-brgm.archives-ouvertes.fr/hal-00912855>.

Daniel Raucoules, **Marcello de Michele**, and J.P. Mallet. Mapping La Valette Landslide (French Alps) displacement Using High Resolution SAR Image Correlation. In ESA Living Planet Symposium 2013, Edinburgh, United Kingdom, September 2013. URL <https://hal-brgm.archives-ouvertes.fr/hal-00846898>. <http://www.livingplanet2013.org/abstracts/843509.htm>.

Guy Woppelmann, Goneri Le Cozannet, **Marcello de Michele**, Daniel Raucoules, Anny Cazenave, Manuel Garcin, Marta Marcos, and Alvaro Santamaría-Gómez. Land subsidence on Alexandria observed by SAR interferometry techniques, implications for exposure to sea level rise. In ESA Living Planet Symposium 2013, Edinburgh, United Kingdom, September 2013. URL <https://hal-brgm.archives-ouvertes.fr/hal-00846892> <http://www.livingplanet2013.org/abstracts/833211.htm>.

**Marcello de Michele**, Daniel Raucoules, Urs Wegmuller, and Christian Bignami. Synthetic Aperture Radar Doppler anomaly detected during the 2010 Merapi eruption. In ESA Living Planet Symposium 2013, Edinburgh, United Kingdom, September 2013b. URL <https://hal-brgm.archives-ouvertes.fr/hal-00846903>. <http://www.livingplanet2013.org/abstracts/850246.htm>.

Goneri Le Cozannet, Guy Woppelmann, **Marcello de Michele**, Daniel Raucoules, Manuel Garcin, and Marcos Marta. Using a series of satellite methods to assess land subsidence in Alexandria. In AGU fall meeting 2012, San Francisco, United States, December 2012. URL <https://hal-brgm.archives-ouvertes.fr/hal-00846903>.

ouvertes.fr/hal-00723323. G10: Geodetic and Oceanographic Tools for Assessing the Impacts of Future Sea Level Rise.

Daniel Raucoules and **Marcello de Michele**. Glissements de terrain sur le Cirque de Salazie observes par correlation d’images radar. In Rencontres « 10 ans de Kalideos », Toulouse, France, October 2012a. URL <https://hal-brgm.archives-ouvertes.fr/hal-00734615>.

Guillaume Bacques, Daniel Raucoules, **Marcello de Michele**, Hideo Aochi, and Frederique Rolandone. The 2004 Parkfield earthquake (Mw 6) post-seismic surface displacement observed by coupling ERS and ENVISAT InSAR between 2005 and 2010. In Wegener 2012, Strasbourg, France, September 2012. URL <https://hal-brgm.archives-ouvertes.fr/hal-00729072>.

Thomas Ulrich, **Marcello de Michele**, and Hideo Aochi. Testing finite differences method for retrieving the slip partitioning of thrust fault branches of the 2008 Wenchuan (Sichuan) China earthquake (MW 7.9). In European Seismological Commission 33-rd General Assembly (ESC 2012), Moscow, Russia, August 2012. URL <https://hal-brgm.archives-ouvertes.fr/hal-00701929>.

**Marcello de Michele**, Sebastien Leprince, Jerome Thiebot, Daniel Raucoules, and Renaud Binet. Measurement of ocean waves velocity fields from a single spot-5 dataset using correlation between panchromatic and multispectral bands. In IEEE International Geoscience and Remote Sensing Symposium : IGARSS ’12 : Remote Sensing for a Dynamic Earth, page paper number #1681, Munchen, Germany, July 2012a. URL <https://hal-brgm.archives-ouvertes.fr/hal-00697335>.

**Marcello de Michele**, Pierre Briole, and Daniel Raucoules. InSAR observation of the shallow MW 5.1 Lorca earthquake (Spain). Comparison with elastic dislocated model. In IEEE International Geoscience and Remote Sensing Symposium : IGARSS ’12 : Remote Sensing for a Dynamic Earth, page congress paper #1674, Munchen, Germany, July 2012b. URL <https://hal-brgm.archives-ouvertes.fr/hal-00697302>.

Daniel Raucoules and **Marcello de Michele**. SAR high resolution image sub-pixel correlation for landslide monitoring. Application to Salazie (La Reunion Island) and La Valette (Alps) landslides. In IEEE International Geoscience and Remote Sensing Symposium : IGARSS ’12 : Remote Sensing for a Dynamic Earth, page paper number 1672, Munchen, Germany, July 2012b. URL <https://hal-brgm.archives-ouvertes.fr/hal-00697315>.

Daniel Raucoules and **Marcello de Michele**. Monitoring Landslides Using SAR High Resolution Image sub-pixel Correlation. In Joint International symposium on deformation monitoring, Hong Kong SAR China, November 2011. URL <https://hal-brgm.archives-ouvertes.fr/hal-00615449>.

**Marcello de Michele**, Daniel Raucoules, and Caterina Negulescu. Surface deformation on the historical centre of the city of Rhodes based on radar interferometric techniques. In Joint International symposium on deformation monitoring, Hong Kong SAR China, November 2011a. URL <https://hal-brgm.archives-ouvertes.fr/hal-00615450>.

Maya Ilieva, Daniel Raucoules, Pierre Briole, Elias Panagiotis, and **Marcello de Michele**. Complex investigation of the moderate seismicity in the Mediterranean. In FRINGE 2011 -Advances in the Science and Applications of SAR Interferometry from ESA and 3rd party missions-, Frascati, Italy, September 2011. URL <https://hal-brgm.archives-ouvertes.fr/hal-00617140>.

**Marcello de Michele**, Alain Giros, Herve Yesou, Daniel Raucoules, and Helene De Boissezon. Kal-Harti: a database for research, risk management and sustainable reconstruction in Haiti. In EGU 2011, Vienne, Austria, April 2011b. URL <https://hal-brgm.archives-ouvertes.fr/hal-00617169>.

**Marcello de Michele**, Daniel Raucoules, Paulino Feitio, Pierre Briole, and Joao Fonseca. the Machaze (Mw 7, 2006, Mozambique) Earthquake: Co and post seismic surface displacement carachterisation using multiband InSAR. In EGU 2011, Vienne, Austria, April 2011c. URL <https://hal-brgm.archives-ouvertes.fr/hal-00617168>.

**Marcello de Michele**, Daniel Raucoules, Julia De Sigoyer, Manuel Pubellier, Cecile Lasserre, Erwan Pathier, Yann Klinger, Jerome Van Der Woerd, and Nicolas Chamot-Rooke. Three dimensional surface displacement of the Sichuan earthquake (Mw 7.9, China) from Synthetic Aperture Radar. In EGU, editor, EGU General Assembly 2010, page 10089, Vienne, Austria, May 2010. URL <https://hal-brgm.archives-ouvertes.fr/hal-00533293>.

Bernard Sanjuan, Philippe Jousset, Gwendoline Pajot, Nicole Debeglia, **Marcello de Michele**, Michel Brach, Francois Dupont, Gilles Braibant, Eric Lasne, and Frédéric Duré. Monitoring of the Bouillante Geothermal Exploitation (Guadeloupe, French West Indies) and the Impact on Its Immediate Environment. In International Geothermal Association, editor, World Geothermal Congress 2010, page 11 p., Bali, Indonesia, April 2010. URL <https://hal-brgm.archives-ouvertes.fr/hal-00496141>.

Yann Gueguen, Marwan AL HEIB, Benoit Deffontaines, Benedicte Fruneau, **Marcello de Michele**, Daniel Raucoules, and Yves Guise. The interferometry technics applied on residual subsidence analysis measurement of closure coal mines, example from Nord-Pas-de Calais coal mine, France. In Symposium Post-Mining 2008, page NC, Nancy, France, February 2008. ASGA. Vandoeuvre-l`es-Nancy. URL <https://hal-ineris.archives-ouvertes.fr/ineris-00973294>.

Yann Gueguen, Benoit Deffontaines, Marwan AL HEIB, Benedicte Fruneau, **Marcello de Michele**, Daniel Raucoules, Yves Guise, and J. Planchenault. Detection, Characterisation, of Residual Mining Subsidence Using SAR Interferometry. Application to Nord/Pas-de-Calais Coalmine. Envisat Symposium 2007, page NC, Montreux, Switzerland, April 2007. European Space Agency. URL <https://hal-ineris.archives-ouvertes.fr/ineris-00973270>.

#### **Scientific vulgarization**

**de Michele M.**, Raucoules D., Foumelis M., Boulahya F., Idier D., Gascon F., “From Ocean Waves to Water Depth: Coastal Bathymetry Derived from Copernicus Sentinel-2 Data”. SENSED, the Remote Sensing and Photogrammetry Society Newsletter, 1, (2018).

**M. de Michele**, D. Raucoules, J. de Sigoyer, M. Pubellier, Cartographie et mesure de la rupture co-sismique à partir d’imagerie radar satellitaire : application au séisme du Sichuan (Chine) du 12 mai 2008. Géochronique n° 110 (2009).

« Objectif Terre, la révolution des satellites » book published by Le Pommier, Paris, 2009. Authors : Jean-Michel Besnier, Vincent Cassé, Michel Kasser, Robert Lainé, Marie-José Lefèvre-Fonollosa, Hervé le Treut, Volker Liebig, Bernard Mathieu, **Mercello de Michele**, Hormoz Modaressi, Daniel Raucoules, Isabelle Sourbès-Verger. Pages 187; ISBN : 978-2-7465-0419-6.

#### **I am regularly called to be a reviewer for:**

the French ANR; IEEE, Transactions on Geoscience and Remote Sensing; Remote Sensing of Environment; Nature Scientific Reports; Geophysical Journal International; Earth and Planetary Science Letters; Remote Sensing.



### 3. SYNTHESIS of my SCIENTIFIC ACTIVITY

#### 3.1 MÉMOIRE de SYNTHÈSE

« Un mémoire de synthèse original (parcours et travaux, responsabilités collectives, conférences invitées, résumé critique des 5 productions les plus significatives). Le mémoire de synthèse de l’activité scientifique du candidat permet de faire apparaître son expérience dans la recherche et dans l’animation d’une recherche ainsi que la (les) direction(s) qu’il compte développer dans les quatre années à venir. Ce mémoire compte approximativement une centaine de pages. »

I earned an Italian “Laurea” in Geological Sciences in 1999, from the University of Pavia in Italy. After one year of civil service, I left for London where I attended an intercollegiate M.Sc. between the University College London (UCL) and Imperial College of Science, Technology and Medicine. The M.Sc. focused on satellite remote sensing and satellite image processing. I took the “geological applications” options at Imperial College, where I chose to work on satellite image investigations of the 2001 Mw 7.8 Kokoxili earthquake (Tibet), with Professor Jian Guo Liu and Dr. Philippa Mason. This topic was of great interest to me. I remember being pretty happy when I was not left the real choice of the final dissertation topic, as I was the only student with the geological background that was needed to conduct this research, the other students being directed towards less “geological” topics for their final dissertation project. To make a long story short, this was a great opportunity for me to hear for the first time about the “new” sub-pixel offset techniques applied to the measurements of the displacement of the Earth surface. I earned the British diploma in September 2002. In late December 2002, I had the opportunity to join the French CNRS (*Centre National pour la Recherche Scientifiques*) at the Institute for the Physics of the Globe in Paris (IPGP), within the Seismological Laboratory directed by Pierre Briole back then. There, I was in charge of applying a CNES-developed cross correlation codes (MEDICIS) to airphotos for volcano deformation monitoring. This work was performed within the frame of the CNES funded “Space Volcanoes Observatory” (SVO) project. My involvement in the project led me to meet Remi Michel and Hélène Vadon, pioneers developers of this method who inspired me a lot for my future researches. At that time, the measurement of ground displacements by cross correlation applied to airphotos (and satellite imagery) was not as common as today, particularly if applied to volcano deformation. My work consisted on trying to adapt the cross correlation method to airphotos, separated 10 years, to measure the displacement field of Piton de la Fournaise volcano summit (La Réunion Island, France). Those results led me to my first paper published as a first author in *Geophysical Journal International*. Besides, I have also been involved in different projects related to space-borne imagery applied to geodetic measurements of

seismo-tectonics, particularly using Interferometric Synthetic Aperture Radar (InSAR), that I learned at IPGP under the supervision of Pierre Briole (today at ENS Paris) and Antonio Avallone (now at INGV, Rome). There, I learned to use DIAPASON, the CNES based codes for interferometric processing. I particularly focused on the InSAR processing of Envisat SAR data on the 2004 Nigata earthquake (Mw 6.8, Japan) and the 2005 Kashmir earthquake (Mw 7.6, Pakistan). Between 2004 and 2005 I had the great opportunity to join TRE (Telerilevamento Europa) in Milan for about 4 months where I learned more about the Persistent Scatterers Interferometry (PSI). There, I had the opportunity to meet Alessandro Ferretti and the TRE crew while I was in charge of writing communication material about geological applications of InSAR and PSI. Alessandro Ferretti, Pierre Briole, Claudio Prati and I wrote a Phd proposal and apply for a Franco-Italian scholarship for which I was the candidate student, on the topic of geological applications of PSI. Unfortunately our project was not selected. Therefore, I went back to France. In late 2005, I joined the French Geological Survey (BRGM), where I am still today. Since the beginning of my career at BRGM, I focused on the use of InSAR and image correlation techniques to the measurements of the displacements of the Earth’s surface on different EU funded projects (SAFELAND, MIAVITA, MEDSUV, MARSITE), ANR funded projects (KALHAITI, CECILE), ESA funded projects (PSIC-4, TERRAFIRMA) and BRGM funded projects (many). I found a scientific fertile environment; the publications that we wrote are testimonies of this. We concentrated on seismo-tectonics, landsliding and volcano deformation using GAMMA mainly; InSAR and sub pixel offsets of both SAR amplitude and optical images. Strong of this experience, I decided to conduct a PhD co-supervised by *Ecole Normale Supérieure de Paris* and *Université Pierre et Marie Curie* in Paris, in parallel of my professional activities (01-2009/11-2010). My PhD had two topics. For the first topic, I studied the 2008, Mw 7.9, Sichuan earthquake from SAR, teaming with the geological laboratory of ENS. For this project, we used ALOS PALSAR L-band data and Envisat C-band SAR combined together along with the cross correlation of amplitude SAR data to retrieve a map of 3D vectors of de deformation field of the Sichuan earthquake. We coupled this data with elastic dislocation modelling for the interpretation of the results and we came out with the evidence of a secondary rupture of a blind thrust at depth. The second topic of my PhD was the InSAR measurement of interseismic shallow creep on the San Andreas Fault at the Parkfield section, using 20 years of ERS SAR data archive, teaming with Frederique Rolandone at the geoscience department of UPMC.

Now (2018), I am a researcher at the French Geological Survey, I still mainly focus on InSAR processing and Sub Pixel offset techniques for the measurements of the displacements of the Earth’s surface. But not only. My main interests are remote sensing applications to seismo-tectonics, volcanology and natural hazards. I teamed up with different colleagues. I study different phenomena related to seismotectonics. Notably earthquakes, such as the Bam earthquake, the Mozambique earthquake, the Sichuan earthquake, the Lorca earthquake, the Parkfield earthquake, and transient

events on the North Anatolian fault at the Ganos section. We also concentrate on volcanic phenomena at Etna (Italy), Merapi (Indonesia), Cordon Caulle (Chili), Holuhraun (Iceland). We also dedicate our attention to the development of SAR methods to study landsliding notably at La Vallette, using high resolution x-band TerraSAR-X data, and La Réunion Island with X-band Cosmo Skymed data and L-Band ALOS PALSAR (1 and 2). Besides conventional methodologies, we try to broaden our application fields and methodological development of SAR and optical satellite data. We mainly developed three branches of applications/methods. Firstly, I recently focused my research on the use of space-borne SAR data to assess the influence of volcanic plumes on the SAR Doppler signal. This idea stems from the observation that the SAR signal is biased from the presence of a volcanic cloud, and other eruption-related phenomena (such as particles motions and lahars) during the SAR focusing. Secondly, we recently proposed an innovative method for the extraction of digital elevation models of volcanic plumes from optical High Resolution (HR) datasets. This method revealed to be crucial to retrieve the volcanic-cloud injection height. Thirdly, I proposed a method to measure the celerity of ocean swell from a single satellite optical dataset which, in turn, led our team to develop a method to map bathymetry from space. A patent is pending on this method. I am still today developing and applying these methods. Today, I am PI for ESA, scientific referee for the steering committee of Solid Earth French national Pole (Form@ter), part of the MIST GdR, EU WP leader (Aphorism) and ESA-CNES “Geohazards Office” scientific board member.

### 3.2 RESEARCH and APPLIED RESEARCH

In the following paragraphs I describe briefly the research projects I have been involved in. BRGM works on a project by project basis; it would be out of scope to encounter them all in 13 years of scientific career at BRGM. I will then describe the most significant to me, where I participated either to the project building, either as investigator, or as a project leader or WP leader. I briefly describe the scope of the project, the source of funding, my main role as well as the principal results.

#### 3.2.1 International Charter on Space and Major Disasters & Cellule d’Intervention et d’Expertise Scientifique et Technique

The International Space and Major Disasters Charter is an agreement between participating space agencies to provide information and data obtained from space to support humanitarian efforts in emergencies caused by major disasters. The Charter is unique in that it can mobilize agencies around the world and take advantage of their expertise and satellite (and ground based) data through a single point of contact. Access is open 24 hours a day, 7 days a week, at no cost to the user. Since November 2000, the Charter has used space-based data to help manage the effects of sudden-onset

natural disasters such as floods, hurricanes, tsunamis, earthquakes, landslides, wildfires, volcanic eruptions. The International Charter on Space and Major Disasters has 17 members: European Space Agency (ESA), National Center for Space Studies (CNES), Canadian Space Agency (CSA), Space Research Organization of India (ISRO), National Oceanic and Atmospheric Administration (NOAA), National Commission for Space Activities (CONAE), Japan Aerospace Exploration Agency (JAXA), United States Geological Survey (USGS), UK Space Agency / DMC International Imaging (UKSA) (DMC), Chinese Space Agency (CNSA), German Aerospace Center (DLR), Korean Institute for Aerospace Research (KARI), National Institute for Space Research (INPE), European Organization for the Exploitation of Meteorological Satellites (EUMETSAT), Russian Federal Space Agency (ROSCOSMOS), UAE Space Agency (UAESA), Agencia Bolivariana para Actividades Espaciales (ABAE) . In France, the “Cellule d’Intervention Scientifique et Technique” (CIEST) is an agreement between six national research organizations (BRGM, CEA, INSU, IGP, IRD, UCBL), which aims to extend the use of space data, and in particular the images acquired within the framework of the International Charter of Space and Major Disasters, for the understanding and the geophysical study of the geological hazards. This agreement came into life in September 2005, with an initial term of three years. Today (2018), the CIEST has become an informal research group; a brainstorm is currently being conducted on the integration of the CIEST activities within the national "solid earth" pole FORM@TER.

How does it work? When the Charter is triggered for a geological disaster (earthquake, volcanic eruption, gravitational movement, tsunami), the members of the CIEST are warned. Scientific teams wishing to contribute to the development of geophysical products access the satellite images acquired. When CNES is Charter Project Manager, the interface with the Charter is natural, when it is not the case, CNES is committed to acting as an interface between the members of the CIEST and the Charter lead. The image data distributed to the members of the CIEST who request them are available in the near-disaster period (Charter operation period) but also beyond three months after the outbreak. This availability allows a thorough analysis of the data for purposes of understanding geological phenomena and geophysical research.

Here are some results I was involved directly in, obtained using satellite imagery as part of the Charter / CIEST:

L’Aquila Earthquake, 2009.

**Ground deformation and a simple dislocation model of the Mw=6.3 April 6, 2009, l’Aquila earthquake (Italy), inferred from ASAR/ENVISAT and PALSAR/ALOS interferometry.**

Analysis and processing by de Michele M., Elias P., Briole P., Raucoules D., a contribution from

*The French Geological Survey, BRGM, Orleans, France; the Institute of Space Applications and Remote Sensing, Athens, Greece; Ecole Normale Supérieure, Laboratoire de Géologie, Paris France.*

An earthquake Mw 6.3 hit central Italy at 1:32 GMT on the 6 of April 2009. The earthquake struck the Abruzzi region in the vicinity of L'Aquila on the Apennine mountain range, a long, narrow mountain range, oriented approximately NW–SE that forms the backbone of the Italian peninsula. We used the European Space Agency ENVISAT Advanced Synthetic Aperture Radar (ASAR) data and the Phase Array L-Band Synthetic Aperture Radar (ALOS) data to construct ascending and descending modes *interferograms* and retrieve the co-seismic surface displacement in the L'Aquila region. The earthquake ruptured with an almost pure normal fault mechanism in the vicinity of Paganica. Given the different viewing angles ( $23^\circ$  for ASAR and  $34^\circ$  for PALSAR) and different viewing geometry of the InSAR data, we combine the interferograms to try to retrieve the vertical and horizontal components of the coseismic surface displacement. Then, the results are inverted against a simple elastic dislocation model. We observe  $\sim 30$  cm vertical surface displacement and  $\sim 24$  cm horizontal surface displacement on a  $47^\circ$  dip angle fault, with a maximum slip of 0.7 meters at 4 km depth. Our interferometric results are also made available on a dedicated page within the Euro Mediterranean Seismological Centre ([http://www.emsc-csem.org/index.php?page=current&sub=recent&evt=ESA\\_123429](http://www.emsc-csem.org/index.php?page=current&sub=recent&evt=ESA_123429)).

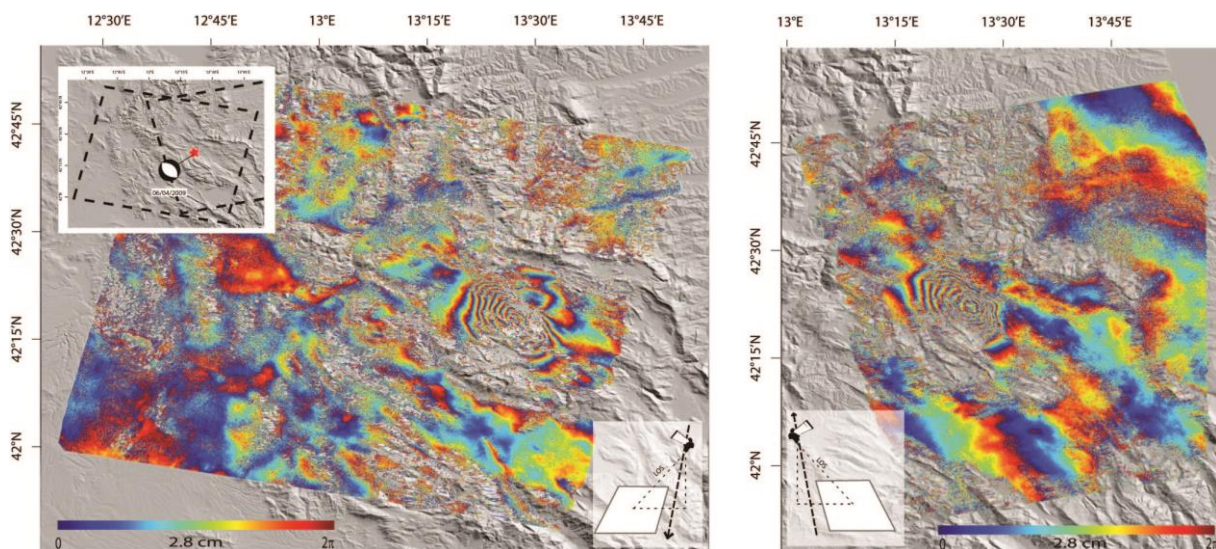


Figure 3.2.1 -1. The displacement field of the L'Aquila earthquake from C band ASAR Interferometry (ascending and descending modes). Image © de Michele et al. 2009, BRGM

Christchurch, 2011.

**The displacement field of the Mw 6.3 South Island of New Zealand Earthquake (February 21st 2011 at 11:51 UTC): PALSAR interferometry and elastic dislocation modeling.**

This analysis has been performed by de Michele M., Briole P., Ruegg J-C, Raucoules D., in the frame of the International Charter on Space and Major Disasters through the French “Cellule d’Intervention Scientifique et Technique”. The data used are from the L-BAND PALSAR sensor on board the Japanese Space Agency (JAXA) Advanced Land Observing Satellite (ALOS). PALSAR data courtesy of JAXA, through CNES (PI on the Charter Call); Data copyright belongs to JAXA, METI. We are thankful to JAXA and CNES for providing the data within the frame of the International Charter on Space and Major Disasters.

PALSAR interferometry (calculated on Friday 2011-02-25, 18:00UTC): we combined PALSAR data acquired on 2011-01-11 and 2011-02-25 (UTC), ascending orbit track 335, Line of Sight (LOS) angle of  $34^{\circ}.3$ , to form a differential interferogram. Topographic contribution to the interferometric phase is modeled and removed by the use of a Shuttle Radar Topography Mission (SRTM) digital Elevation Model. The interferogram shows a pattern of interferometric fringes each of which represents  $\sim 11.5$  cm of surface displacement in the LOS direction. Data processing has been performed at the *Bureau de Recherches Géologiques et Minières* (BRGM) for the CIEST group with the GAMMA processor. Preliminary Elastic Dislocation modeling has been calculated at “Ecole Normale Supérieure de Paris” (ENS) with the code Inverse3.

For the elastic dislocation modeling, we picked the fringes where we could see and count them. We chose a total of 210 points. We made an inversion (for a single fault plane) using the value at the 210 sample points. We did not try to invert the dip angle and maintained it at  $65^{\circ}$ . We tried to leave free or not all other parameters. The strike angle and slip angle and slip amplitude were not stable, especially when left free simultaneously. We were obliged to fix the strike and slip angles. For this model we used  $65^{\circ}$  for the strike and  $135^{\circ}$  for the slip, as in the previous model. Then we inverted for the other parameters and the result was quite stable with the following parameters: coordinates of the center of the upper edge of the fault: 43.53620S, 172.71561E, -2km. In this model the fault does not reach the surface but ends 2km beneath the surface, this depth is mostly constrained by the (non zero) spacing of the fringes north and north-west of the fault). Fault length: 8km (probably around the lower bound for the magnitude). Fault width: 8km. Slip: 1.63m (around upper bound for the magnitude). Geodetic moment tensor:  $3.13 \cdot 10^{18}$  Nm (60% higher than the moment tensor from the CMT Harvard, the difference is relatively large, the only way we found to reduce the geodetic moment tensor was to move the fault closer to the surface and then the fringes north of the fault were becoming much closer than observed, a variable slip around the upper tip of the fault might

help resolving part of the discrepancy). Source duration: Harvard indicates 2.8s half-time and 4.8s hypocenter v/s centroid, those numbers are a bit high for the size of our modelled fault, discrepancy to be analyzed.

<https://www.emsc-csem.org/Earthquake/194/M-6-3-SOUTH-ISLAND-OF-NEW-ZEALAND-on-February-21st-2011-at-11-51-UTC>

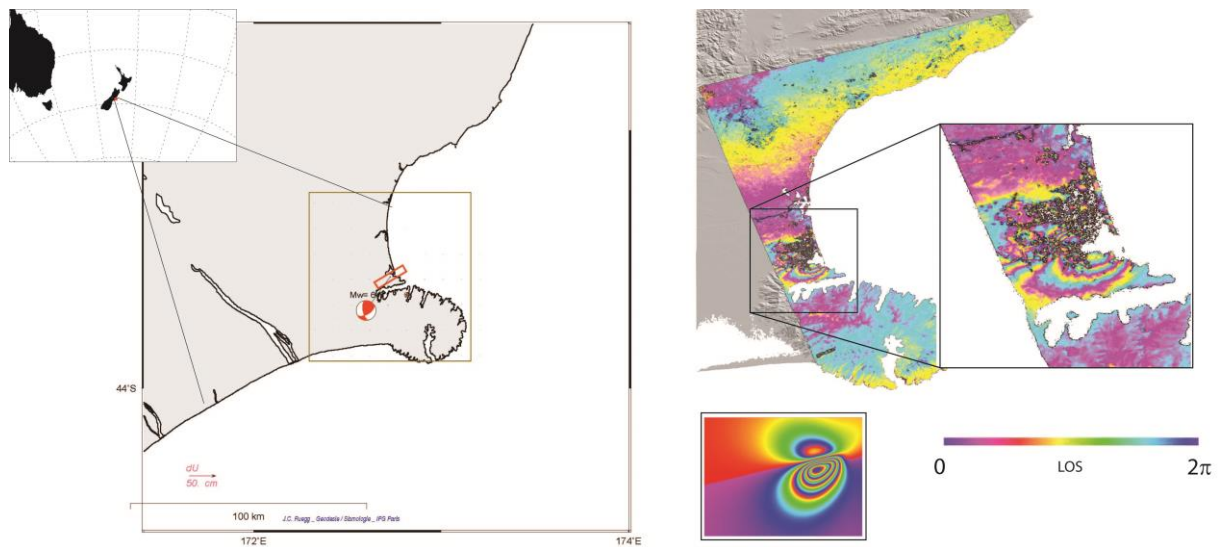


Figure 3.2.1 -2. The displacement field of the Christchurch earthquake as seen by ALOS PALSAR interferometry and elastic dislocation model. Image © de Michele et al. 2011, BRGM, ENS.

3.2.2 European funded projects, within the 6<sup>th</sup> and 7<sup>th</sup> framework program for research and development.

**Advanced Procedures for Volcanic and Seismic Monitoring (Aphorism)**, 2013-2016. Project Funded by the Seventh Framework Programme of the European Commission. Aphorism was a collaborative project developed under the theme FP7-SPACE-2013-1. The consortium was made by INGV Rome, BRGM, Institute of Telecommunications of Barcellona (ITC), University of Rome, University of Oxford, Gamma Remote Sensing and Alma Sistemi. Aphorism project proposes the development and testing of two new methods to combine different types of Earth Observation satellite data and ground data. The aim of APHoRISM was to demonstrate that an appropriate management and integration of satellite and ground data can provide new improved products useful for seismic and volcanic crisis management. In particular, the project is focused on two main products: one is related to the monitoring of volcanic crises (volcanic product) and the other one concerns seismic events (seismic product).

The volcanic product is generated using the Multi-platform volcanic Ash Cloud Estimation (MACE) method. This method exploits the complementarity between Geosynchronous Earth Orbit sensors, Low Earth Orbit satellite sensors and ground measurements to improve the ash detection and retrieval and to fully characterize the volcanic ash clouds from source to the atmosphere. The key idea consists in meaningfully improving (calibrating and integrating), in a novel manner, the volcanic ash retrievals at the space-time scale of typical geostationary observations using both the Low Earth Orbit satellite estimations and in-situ data. The typical ash thermal infrared retrieval is integrated by using a wider spectral range from visible to microwave and the ash detection is extended also in case of cloudy atmosphere or steam plumes.

The seismic product consisted of a damage map addressing the detection, analysis and estimate of changes to buildings and infrastructures occurring during an earthquake in the epicentral regions. The damage map is obtained by integrating a priori information and change detection images. The a priori information is derived by applying processing techniques to pre-crisis interferometric Synthetic Aperture Radar data to measure possible surface movements. This first product provides information on the stability of the terrain. An integration algorithm merges the a priori information, the detection of changes observed by Earth Observation sensors and ground shakemap from seismological data. The final product is a Likelihood Index Damage Map, which represents a map of group of buildings or single buildings and infrastructures that are likely collapsed or strongly damaged (Source : Aphorism.eu).

As for as the administrative part, I was the Work Package 2 leader and coordinator, dedicated to the users requirements and the integrated products definition. In terms of scientific and technical involvement, I took part to WP3 dedicated to new monitoring techniques to detect or characterize volcanic plumes from space-borne data. We applied and developed further the method presented in de Michele et al. (2013). Here, our group developed further the methodology based on the SAR Doppler anomalies during the SAR focusing caused by the presence of a volcanic plume. We applied the methodology on Etna volcano, during lava fountains episodes of 2011-2013 and the flank eruptions of 2002-2003. We used Envisat SAR and Radarsat data. Our method is particularly interesting for the volcanological community as it can potentially detect de presence of a volcanic cloud in cloudy sky conditions, where other sensors (based on optical analysis) might fail. While the results could assess the methodology, we highlighted that the influence of topography in the SAR Doppler analysis could not be neglected. We started to develop a method based on differential Doppler analysis, aiming at compensating any common topographical signature in the Doppler signal during the focusing of SAR data acquired at two different (consecutive) dates over the same volcano and over the same eruptions. While these results are presented in the Aphorism project reports, they still need to be investigated further. Besides, we concentrated on the plume injection height

measurement. This information is crucial in volcanology as several geophysical parameters control the injection height and, in turns, the injection height is a fundamental parameter for the modelling of the plume dispersion in the atmosphere. We used optical data from Landsat 8, Pleiades and SPOT5 to construct digital elevation models of the volcanic clouds on Etna volcano. This method, that we called Plume Elevation Models, was already presented in de Michele et al. (2016) applied to Landsat 8 data on the Holuhraun (Iceland) fissural eruption.

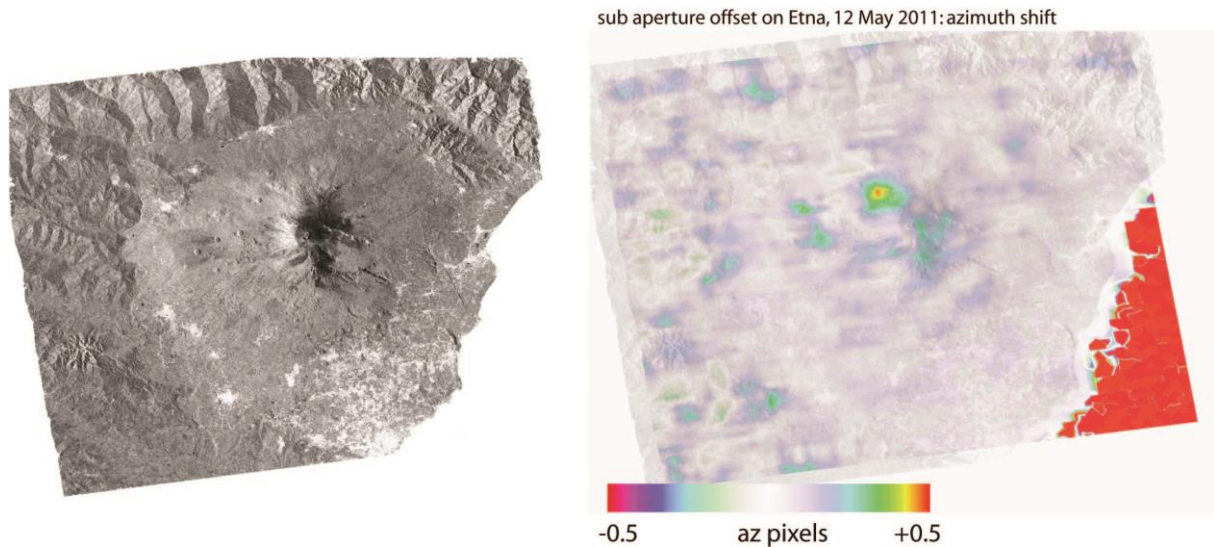


Figure 3.2.2 -1. Left, SAR amplitude image of Mount Etna. Right, SAR Doppler anomalies detected during the Etna volcano lava fountains episodes of 11 May 2011. Results published in the Aphorism project report (2016).

**MEDSUV : Mediterranean Supersite Volcanoes** (2013-2016). MedSuv project was funded under the frame of the Supersite 7th Framework Programme of the European Commission, with 24 partners, led by INGV Catania (Italy). The MED-SUV project proposed the development and implementation of a state-of-the-art infrastructure for the volcanic risk management life-cycle, from the observation to people preparedness, in southern Italy. The infrastructure relies upon the improvements of the understanding of geophysical processes underlying the volcanic systems of Vesuvius / Campi Flegrei and Mt. Etna. It would also achieve the integration of existing components, such as monitoring systems and data bases, novel sensors for the measurements of volcanic parameters, and tools for data analysis and process modelling.

This project is funded under the call FP7 ENV.2012.6.4-2 : Long-term monitoring experiment in geologically active regions of Europe prone to natural hazards : the Supersite concept. Grant agreement n°308665. I was involved into the WP2 “new monitoring and observing systems”. In this work package, led by the German Aerospace Agency (DLR), we used SAR data from TerraSAR-X to

spot Doppler anomalies related to the Eyjafjallajökull 2010 eruptions. The basic idea behind this method has been developed in de Michele et al. (2013). Our aim here was to analyze the x-band Doppler history, during a single satellite pass, to understand whether the SAR signal was affected by the presence of the volcanic cloud. The results, presented in the MEDSUV reports, were not conclusive in terms of the original subject and need more thorough interpretation. Besides, we could see that the Doppler SAR history is perturbed by a number of volcano-related phenomena including “laars” that impact the signal much more than the expected delay related to the volcanic cloud. In a complementary fashion with the Aphorism project, In MEDSUV we understood further the importance of the measurement of the injection height of the volcanic cloud. Therefore, in the MEDSUV context, we applied the method developed in de Michele et al. (2016) for the extraction of PEMs to Etna 2013 eruption. We applied the method to Landsat 8. The results are being validated with independent measurements from IASI, in collaboration with INGV Rome, the University of Oxford and ENS Paris, and will be presented at the EGU 2018.

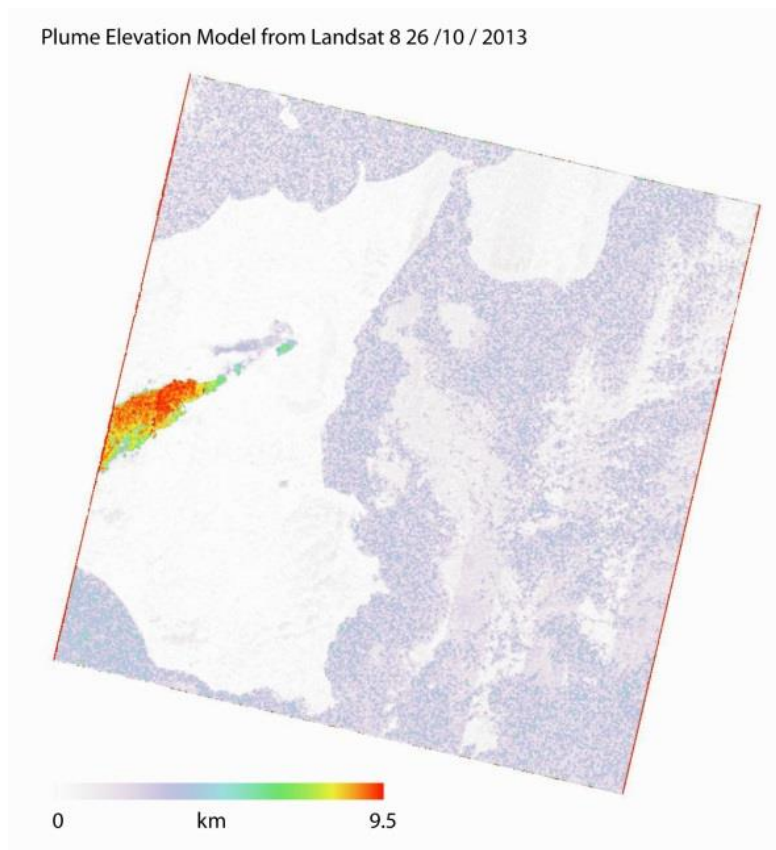


Figure 3.2.2 -2. Mount Etna eruption, 26 October 2013. Volcanic plume elevation form Landsat 8. Image © de Michele et al. 2015, BRGM (unpublished).

**MARSITE: New Directions in Seismic Hazard Assessment through Focused Earth Observation in the Marmara Supersite, 2013-2016.** Marsite was an international project funded within the 7<sup>th</sup> Framework Programme of the European Commission. MARSite aimed at assessing the “state of the art” of seismic risk evaluation and management at European level, to establish a starting point, to move a “step forward” towards new concepts of risk mitigation and management by long-term monitoring activities carried out both on land and at sea. MARSite coordinated research groups with different scientific skills in a comprehensive monitoring activity developed both in the Marmara Sea and in the surrounding urban and country areas. The project planned to coordinate initiatives to collect multidisciplinary data, to be shared, interpreted and merged in consistent theoretical and practical models suitable for the implementation of good practices to move the necessary information to the end users. MARSite planned to coordinate initiatives of research European partners focused on: the collection multidisciplinary data; their dissemination, interpretation and fusion to produce consistent theoretical and practical models; following good practices so as to provide the necessary information to end users; and updating seismic hazard and risk evaluations in the region, particularly in Istanbul.

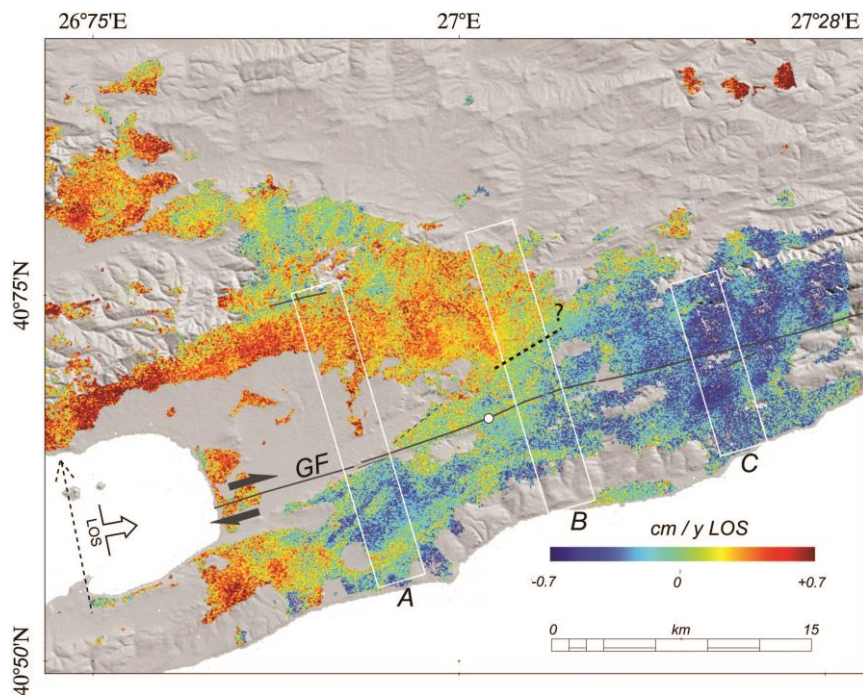


Figure 3.2.2 -3. InSAR PALSAR derived mean velocity on the Ganos section of the North Anatolian Fault zone.

Results published in de Michele et al., 2017.

In the MARSite context, within work package 3, I was in charge of the use of archived L-band SAR data from ALOS PALSAR applied to the measurement of the displacement field of the Ganos section of the North Anatolian Fault (NAF). This section of the NAF is considered as locked, but its behavior is not

completely understood. We tried to push the InSAR analysis on this section of the NAF by removing Radio Frequencies Interferences in the SAR data and by combining multiple polarizations data to improve the available data stack. Our results, coupled with a simple elastic dislocation model, might suggest shallow transients on this section of the NAF. They are published in de Michele et al. (2017).

**NEMOH - Numerical, Experimental and stochastic Modelling of vOlcanic processes and Hazard, 2012-2015.** NEMOH is an Initial Training Network under the European Community FP7. The training objective of NEMOH is that of forming the next generation of European volcanologists, capable of extending further the knowledge and understanding of volcano dynamics and the methods and paradigms for volcanic hazard evaluation. Training is conceived to develop in the context of internationally coordinated research structured in closely interconnected research activities. My task in this project was to co-supervise the PhD thesis of Claudio Trovato. We planned to use InSAR analysis on Etna volcano as a hint for the numerical simulation of ground deformation signal.

**Miavita**, Mitigate and assess risk from volcanic impact on terrain and human activities, 2008-2012. Miavita was project funded under the FP6 European Framework Programme of the European Commission, under the call ENV.2007.1.3.3.1. - Assessing and managing volcanic threat. In EU countries, volcanic risks assessment and management are tackled through scientific knowledge and monitoring, although there is still a need for integration between all risk management components. For international cooperation partner countries (ICPCs), the risk management depends on local situations but is often less favorable. Therefore, following UN International Strategy for Disaster Reduction recommendations and starting from shared existing knowledge and practices, the MIA-VITA project aims at developing tools and integrated cost effective methodologies to mitigate risks from various hazards on active volcanoes (prevention, crisis management and recovering). Such methodology will be designed for ICPCs contexts but will be helpful for European stakeholders to improve their experience in volcanic risk management. The project multidisciplinary team gathers civil defense agencies, scientific teams (earth sciences, social sciences, building, soil, agriculture, Information Technologies and telecommunications) and an IT private company. The scientific work will focus on: 1) risk assessment methodology based on a multi-risk approach developed at Mt Cameroon by one of the partners in cooperation with Cameroonian institutions 2) cost efficient monitoring tools designed for poorly monitored volcanoes (satellite & gas analysis & volcano-seismology) 3) improvement in terms of vulnerability assessment (people, buildings and biosphere) 4) socio-economic surveys to enhance community resilience 5) Integrated information system (data

organization and transfers, communications) taking advantage of GEONET Cast initiative Results will be achieved with help from local scientists and stakeholders in Africa (Cameroon, Cape Verde), in Asia (Indonesia, Philippines) and will be validated on a European volcano (Montserrat). The objectives will be reached through sharing/transfer of know-how, through scientific and technological developments, and through dissemination/training.

My role in MIAVITA has been attributed by the Merapi eruption. When Merapi erupted, conventional C-band InSAR was unusable because of the dense vegetation on the study area, yielding incoherent results. The offset tracking results pointed at more than 10 meters co-eruptive flank displacement, potentially threatening the surrounding areas, while field observations performed by the Indonesian Geological Authority showed no evidences of ground displacement on the volcano. Enquired by my colleagues on this subject, I came out with the idea that the presence of a volcanic plume, or a volcanic related phenomena (such as lahars) could impact the SAR Doppler history during the SAR focusing, thus impacting the theoretical pixel positioning in the SLC (Single Look Complex) image. If this was true, multitemporal offset tracking could show and 'apparent' ground motion. To verify this hypothesis, we came out with idea of analyzing the Doppler history of a single SAR acquisition by detailed sub-aperture correlation. In theory, sub-aperture correlation of a single SAR acquisition should be zero. If not, it means that there should be a phenomenon that has perturbed the SAR Doppler history during the focusing. The results of the experiment were positive, thus we made the hypothesis that the perturbing phenomenon could be the presence of a volcanic cloud during the SAR acquisition. The results are presented in de Michele et al. (2013).

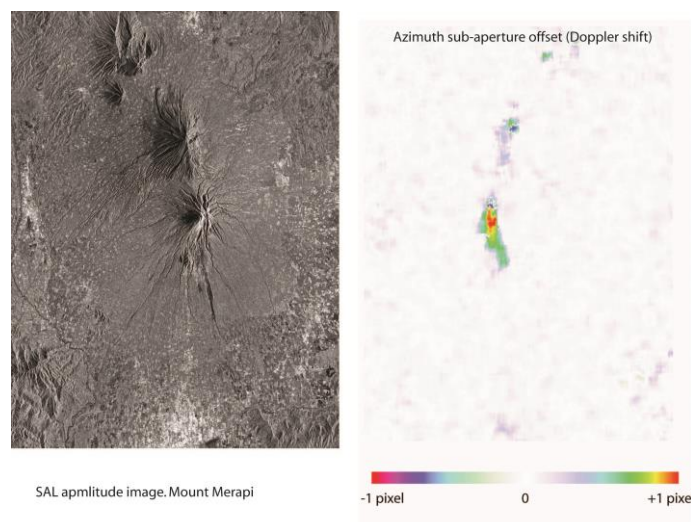


Figure 3.2.2 -4. Left, Radarsat amplitude image on mount Merapi on 23 November 2011. Right, sub-aperture offset indicating a Doppler anomaly during the SAR image acquisition process. In this very case, the Doppler anomaly might be due to lahars velocity. © de Michele et al. 2012, BRGM (unpublished).

**Safeland, 2010-2013.** SafeLand is a Large-scale integrating Collaborative research project funded by the The Seventh Framework Programme for research and technological development (FP7) of the European Commission. Thematically the project belongs to Cooperation Theme 6 Environment (including climate change), Sub-Activity 6.1.3 Natural Hazards. The project team composed of 25 institutions from 13 European countries is coordinated by Norwegian Geotechnical Institute (NGI). SafeLand will develop generic quantitative risk assessment and management tools and strategies for landslides at local, regional, European and societal scales and establish the baseline for the risk associated with landslides in Europe, to improve our ability to forecast landslide hazard and detect hazard and risk zones. In this project, we proposed to use the high spatial resolution and high revisiting capacity of the DLR TerraSAR-X data to construct a 4-dimensional map of the displacement field of La Vallette landslide (French Alps). We exploited the 1 meter pixel size, along with the offset tracking method applied to both ascending and descending TerraSAR-X data to extract the spatiotemporal evolution of this large, fast moving, landslide from space. The results are published in Racoules et al., (2013).

### 3.2.3 ANR, Agence Nationale de la Recherche

**Kalhaiti, 2010-2014.** KalHaïti project was funded by the French ANR within the frame of the call "Séisme Haïti : pour une reconstruction durable", following the 2010 earthquake. The earthquake that struck Haiti on 12 January 2010 (Mw 7.1) represents one of the worst catastrophes on this territory causing more than 200 000 deaths and leaving 2 millions homeless. This earthquake highlighted the need for scientific studies for better understand the tectonic context and the seismic cycle in the area. Besides, during the crisis phase, a large number of satellite images, both radar and optical, have been acquired in the frame of the International Charter of Space and major Disasters. After interpretation, these data are used by the Civil Protection to organize the rescue team and plan the land use and reconstruction. During the emergency phase, these data are useful to cover the risk management cycle, from prevention to reconstruction. This implies that the data archive is made available to users, decision makers and scientists. The archive, including in-situ data, should make easily available and accessible locally and remotely. Kalhaiti project aimed at building and deploying an easily accessible database of satellite imagery to local authorities, scientist and all the actors involved in the mitigation of seismic risk in Haiti, sustainable reconstruction and resilience analysis. Kalhaiti is meant to be an infrastructure in support to applied research in the aforementioned fields. The infrastructure is built by CNES and a mirror site is hosted in Haiti. The initial phase of the project was supported by ANR. CNES will guarantee the functioning of the infrastructure for further ten years

form the end of KalHaiti project. My role in the project was to make a link between the remote sensing and the geohazard community. Besides, my role was technically related to the implementation of L-band SAR data within the base, their potential use in the understanding of the seismotectonic of the area (InSAR) and to foster their application to understand and mitigate geohazards in Haiti.

**CECILE, 2010-2013.** Changement Environnementaux Côtiers : Impact de L'Elévation du niveau de la mer ou Coastal Environment Changes Impact of sea L'Level. BRGM project leader : Goneri Le Cozannet.

The CECILE project brought together 8 partners (BRGM, LEGOS, Météo France, CNRS, LIENSS, Cerfacs, CREOCEAN, SHOM). Its mission is to analyze the vulnerability of coastal areas faced with the phenomenon of rising sea levels by examining positions at several levels in the scale as part of an integrated approach that takes account of the multi-factor aspect of the process. The project is jointly run by the BRGM (project coordination) and LEGOS (scientific coordination), with a 45-month mission (January 2010 to September 2013). The project was based on six work packages. WP1: Selection of study areas and gathering of any kind of information that might allow characterization of coastline shifts in these regions. WP2: Take a look at the climatic causes of past and future variations in ocean levels. WP3: Multi-scale analysis of the relative rise in sea levels. This concentrates on the systematic analysis of collected bathymetric data in order to bring out trends, isolate indications, or correct old biases. WP5: Development of an integrated methodology based on precise indicators for identifying the causes of coastline shift and assessing future impacts with respect to terrain type and time scale. WP6: Distribution and development of the research results.

In CECILE project I was involved in the processing and interpretation of InSAR data to assess the increasing exposure to sea level rise of the city of Alexandria due to land subsidence. Delta margins are subject to relatively high rates of land subsidence and have the potential to significantly exacerbate future changes in sea levels predicted by global warming models used in impact studies. Through a combined analysis of GPS and persistent scatterer interferometry data, we have determined that most of the coastline of Alexandria has been subject to moderate land subsidence over the past decade (0.4 mm/year on average and up to 2 mm/year locally). This contrasts to previous studies that suggested subsidence in excess of 3 mm/year. Based on our findings, we infer that on multi-century to millennia timescales, land subsidence in the area of Alexandria is dominated by tectonic setting and earthquakes or gravitational collapse episodes of a growth fault, whereas on shorter inter-seismic decadal to century timescales, subsidence rates are likely steady and moderate,

in agreement with natural compaction and dewatering of the observed Holocene sediment layer. These results were published as Woppelmann et al., 2014.

#### 3.2.4 ESA funded projects

**PSIC-4, 2005-2007.** Persistent Scatterers Interferometry Cross Comparison and Certification (2004-2006). The Persistent Scatterer Interferometry (PSI) methods are a group of new and technologically advanced technologies for measuring relative position of (usually) bright targets in the direction of the satellite line-of-sight (LOS) with millimetric accuracy in ideal cases. In response to a recommendation of the Fringe 2003 Workshop, ESA initiated the Persistent Scatterer Interferometry Codes Cross-Comparison And Certification (PSIC4) Project to produce reliable information about the accuracy and dependability of these methodologies. The work was divided into two phases. The first phase concerned parallel processing of identical stacks of data by the participating EO service providing contractors. The second phase consisted on independent validation of the results to be carried out by a separate consortium of survey experts. I was involved in the second aspect (cross comparison and validation). The results are published as Raucoules et al., 2009.

**Geohazard office, 2018-2020.** With Michael Foumelis and Daniel Raucoules (BRGM). The Geohazards Office is an activity integrated in the Geohazards Lab initiative within the Committee on Earth Observation Satellites (CEOS) Working Group on Disasters (WG Disasters) to enable a greater use of Earth Observation (EO) data and derived products to assess geohazards and their impact. The CEOS WG Disasters is a collaboration among ten space agencies, comprising a range thematic pilots and demonstrators (multi-hazard Recovery Observatory, GEODARMA etc.), led by CEOS in the frame of the inter-governmental Group on Earth Observations (GEO). The aim is to establish an inclusive, comprehensive process to optimize the use of EO technologies starting from the needs of national and local decision-makers in political and socio-economic sectors relevant to DRM. In addition, a new activity initiated within the CEOS WG Disasters is the Geohazards Lab, an initiative based on a group of interoperable platforms with federated resources providing EO data access, hosted processing and e-collaboration capabilities to animate and support the geohazard user community. It is originated by the European Space Agency (ESA), the German Space Research Centre (DLR), the Italian Space Agency (ASI) and the French Space Agency (CNES). One of its precursors is the Geohazards Exploitation Platform (GEP), an ESA originated processing platform made available since 2016 within the CEOS WG Disasters pilot on seismic hazards. The Geohazards Lab focuses on different thematic areas of geohazards, typically seismic, volcanoes, terrain subsidence and landslides. The users of the Geohazards Lab include users from the WG Disasters pilots and demonstrators, the RO, the Geohazards Supersite and Natural Laboratories (GSNL) and GEO-DARMA who are able to execute

processing chains on the platform as well as other EO experts/geoscience centers already contributing to precursors activities such as the users of the GEP.

In this context, the Geohazards Office, envisaged and supported by ESA in collaboration with CNES is an activity to develop a collaborative framework with expert geoscience centers and users to achieve a greater adoption of EO methods. Its goals are to support the exploitation of hosted processing capabilities with a focus on Cloud processing solutions, define consensus methods in liaison with experts to harmonize EO based processing results, establish a methodological approach to support the generation of reference ground deformation measurements in support to historical hazard analysis, and finally, utilize available EO capabilities looking at geohazards. The Geohazards Office intends to help bridge the gap between the space community and the geohazards community with a strong focus on expert users from geoscience centers who are the priority intermediaries with end users.

### 3.2.5 Some of the BRGM research framework programs, 100% funded by BRGM

CENdReS « Calcul de modèles numériques d’Élévation des Nuages de cendres volcaniques Depuis une Restitution Satellitaire : Plume Elevation Models (PEMs) », funded 2017. I was project leader and principal investigator.

Nicolo « New Insar survey based on COpernicus and L-band Observations », funded 2017. Project leader, Daniel Raucoules. I was co-investigator.

Bathysat « water depth inversion from satellite dataset », funded 2016-2017. Project leader, Deborah Idier. I was co-investigator.

Seismorisk « recherche et developpement en risqué sismique », funded 2009-2014. Project leader, Hideo Aochi. I was co-investigator on the use of InSAR and offset tracking methods to map displacement fields of the Earth surface due to earthquakes.

Metrophy « Metrologie Geophysique », funded 2005-2010. Project leader, Claudie Carnec. I was co-investigator on the methodological (geophysical) development of InSAR and offset tracking methods.

### 3.3 PhDs, POSTOCS, INTERNSHIP SUPERVISION.

PhD thesis. Guillaume Bacques (2010 - 2013).

I have been co-supervisor (30%) and a jury member for Guillaume Bacques' thesis, which took place between 2011 and 2013. Guillaume's thesis focused on the use of InSAR for observation and the modeling of the seismotectonic deformation, notably on large creeping faults (San Andreas Fault, USA) and on plate convergence zones where slow earthquakes occur (Guerrero, Mexico). The PhD project, co-funded by CNES and BRGM, was hosted by the Institute of Earth Sciences of Josef Fourier University of Grenoble (IsTERRE) and the BRGM, under the direction of Michel Campillo and the co-director Hideo Aochi. The PhD has been co-supervised by Daniel Raucoules (BRGM) and Erwan Pathier (IsTERRE) other than myself.

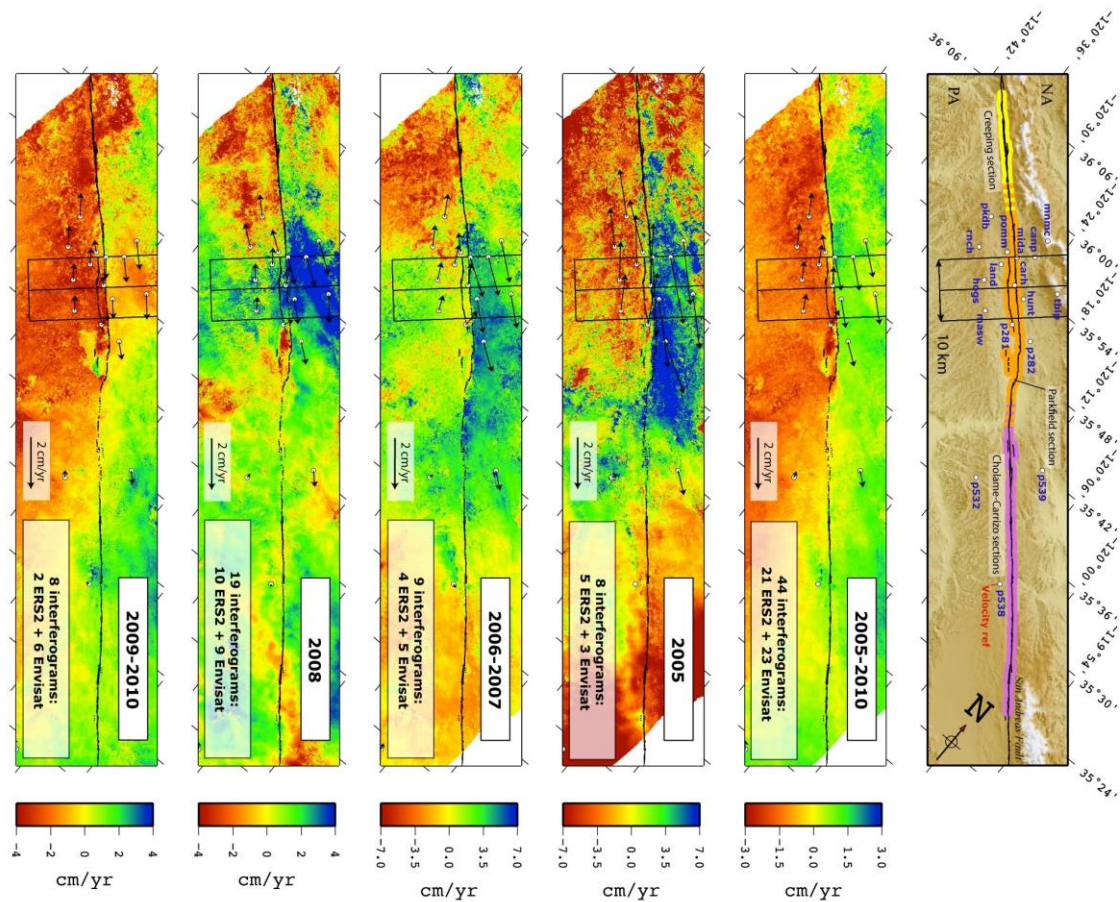


Figure 3.3 -1. San Andreas Fault surface displacement from Stacked ERS and ASAR interferograms at 5 given time intervals between 2005 and 2010. These results are from Bacques et al., Scientific Reports (2018).

The results of Guillaume's thesis have resulted in several presentations at national and international conferences and an article published in Scientific Reports (2018) « Shallow deformation of the San-Andreas fault 5 years following the 2004 Parkfield earthquake (Mw6) combining ERS2 and Envisat

InSAR » by Guillaume Bacques, Marcello de Michele, Daniel Raucoules, Hideo Aochi, Frédérique Rolandone. The study focuses on the shallow deformation during the 5 years following the Parkfield earthquake (28/09/2004, Mw 6, San Andreas Fault, California). In the study, we used the ability of Synthetic Aperture Radar interferometry (InSAR) to provide precise measurements of transient deformation following the Parkfield earthquake between 2005 and 2010. We proposed a method to combine both ERS2 and ENVISAT interferograms to increase the temporal data sampling. Firstly, we combined 5 years of available SAR acquisitions including both ERS-2 and Envisat. Secondly, we stacked selected interferograms (both from ERS2 and Envisat) for measuring temporal evolutions of ground velocities at given time intervals. Thanks to its high spatial resolution, InSAR could provide new insights on the shallow fault motion behavior over the 5 years following the Parkfield earthquake. As a complement to previous studies in this area, our results suggested that transient deformations play an important role into the Parkfield seismic cycle. This might affect the time recurrence variability of Mw6 earthquakes.

PhD thesis. Claudio Trovato (2012 – 2015).

Claudio's thesis was funded in the context of the Nemo project (EU Marie Curie fellowship). I was co-supervisor at approximately 5%. The thesis was directed by Bruno Scaillet (Institut de Science de la Terre d’Orléans) and hosted by BRGM under the direction of Hideo Aochi. The subject dealt with earthquake at Long Period (LP) on Mt. Etna (Italy), inversion of the moment tensors and uncertainties related to their interpretation. The thesis also involved a brainstorm on an inversion method to integrate different sources of soil deformation measurement (including InSAR) for the characterization of the volcanic environment.

PhD Thesis. Yann Gueguenn (2004 - 2007).

I was co-supervisor (20%) and jury member of Yann Gueguenn's thesis, between 2005 and 2007. The thesis project focused on the use of PSInSAR applied to ERS and Envisat C-band SAR data to measure the residual deformation due to mining in Nord Pas de Calais (France). The thesis was co-funded by BRGM and Charbonnage de France (now DPSM).

Yann PhD results were collected in a publication for the Journal of Applied Geophysics in 2019, titled “Monitoring residual mining subsidence of Nord/Pas-de-Calais coal basin from differential and Persistent Scatterer Interferometry (Northern France)” by Y. Guéguen, B. Deffontaines, B. Fruneau, M. Al Heib, M. de Michele, D. Raucoules, Y. Guise, J. Planchenault. Both differential SAR Interferometry (DInSAR) and Persistent Scatterer Interferometry (PSI) were used to estimate surface displacement of the Nord/Pas-de-Calais coal basin during a 15-year period (1992–2007) after the end of 270 years of mining exploitation. On the results issued from ERS and Envisat data processing, even

if the area undergoes high temporal decorrelation due to the high amount of field crops, present residual deformation are well detected. Those deformations show low amplitude with a maximum rate of more than 1 cm/year during a period of 5 to 7 years after the end of the mining exploitation (1992– 1999). Then decrease up to stability, prevails, depending on the area. The deformation field obtained by differential and Persistent Scatterer Interferometry showed good agreement with the traditional methods of levelling comparison focused on specific sites. The recent displacements, revealed by DInSAR and PSI within a wider area, led us to propose various natural (geology and neotectonics) or/and anthropic origins.

Post doctorate. Adrien Poupardin (2013-2014).

I co-supervised the post doc of Adrien Poupardin with Daniel Raucoules and Deborah Idier. This project, funded by the Carnot Institute between 2013 and 2014, stemmed from a new idea from BRGM, which had been explored a few years before, the results of which are reviewed in Michele et al. (2012): the ability to measure ocean wave velocities accurately from an optical spaceborne dataset using quasi-synchronous images. The celerities and wavelengths of the oceanic swell are controlled by the coastal bathymetry: Adrien's work focused on the development of an original method to restore the bathymetry from these two measurements. Adrien Poupardin used a set of SPOT-5 data. He came out with an original idea of using wavelet analysis to calculate a multiple set of wavelengths associated with multiple sets of celerities. We called the method CWB (Correlation-Wavelet-Bathymetry). The encouraging results are published in several conference proceedings and a specific article published in IEEE Transaction on Geoscience and Remote Sensing in 2016 "Water depth inversion from a single SPOT-5 dataset" , by A. Poupardin, D. Idier, M. de Michele, D. Raucoules. The method is the subject of a patent that we submitted in 2015 (WO 2016132068 A1). The SPOT 5 data were obtained thanks to a PNTS funding (Programme Nationale de Teledetection Spatiale) and thanks to the Kalideos “Isle de la Réunion” program by CNES.

Co-supervision of the internship of Master student (M2) Konstantinos Derdelakos

Konstantinos internship took place at the BRGM in 2015 during his Master 2 studies at the Paris ENS, supervised by Pierre Briole at the Geology Laboratory, Department of Geosciences. The internship topic, which was part of the EU MEDSUV project, focused on the use of Sentinel 1 for interferometric tracking of soil deformation along the Pernicana Fault on the Etna volcano during the 2015 eruption. Konstantinos developed the Sentinel 1 interferograms using the GAMMA tools and reconstructed the ground deformation history as well as an average velocity map between the beginning and the end of the eruption. His results, shared with the INGV Catania, revealed co-eruptive residual movements on "secondary" faults, i.e. a reactivation of pre-existing faults during the eruption. The results of this

research internship are the subject of a poster presented during the final workshop of the MEDVUS project, 2016 titled « Creeping on the flanks of mount Etna (Italy) monitored by means of ERS, Envisat and Sentinel-1 interferometry for the period 1992-2016 » by Derdelakos K., Mitoukaki S., Guglielmino F., Elias P., Bonforte A., Puglisi A., Parcharidis I., de Michele M., Raucoules D., Briole P. In the full study, SAR interferometry and GPS, used at Mount Etna since more than twenty year, show that the volcano is characterized by a relative stable western domain and a mobile eastern flank. The boundary between both is well defined to the North with a unique discontinuity, the Pernicana fault. The South boundary is more complex with several right lateral faults, e. g. Mascalucia, S. Leonardello and Timpe faults. Their motions, combines shallow creep as well as co-seismic displacement. In this work Konstantinos studied the spatio-temporal variability of the motion along those faults in the period 1992-2016. Konstantinos produced a series of interferograms using ERS and Envisat ASAR archived data with a maximum baseline of 250 meters and time span of 4 years. Using published fault maps and the interferograms, Konstantinos refined the location of the faults and discussed the status of the transition between faults. Konstantinos accurately calculated the average slip velocity and temporal changes from our InSAR data. Then, Konstantinos compared them with available published results including GPS and InSAR. In a second step, Konstantinos used sentinel 1 along with the SBAS approach to measure creeping along those faults, specifically related to the 2015 eruption.

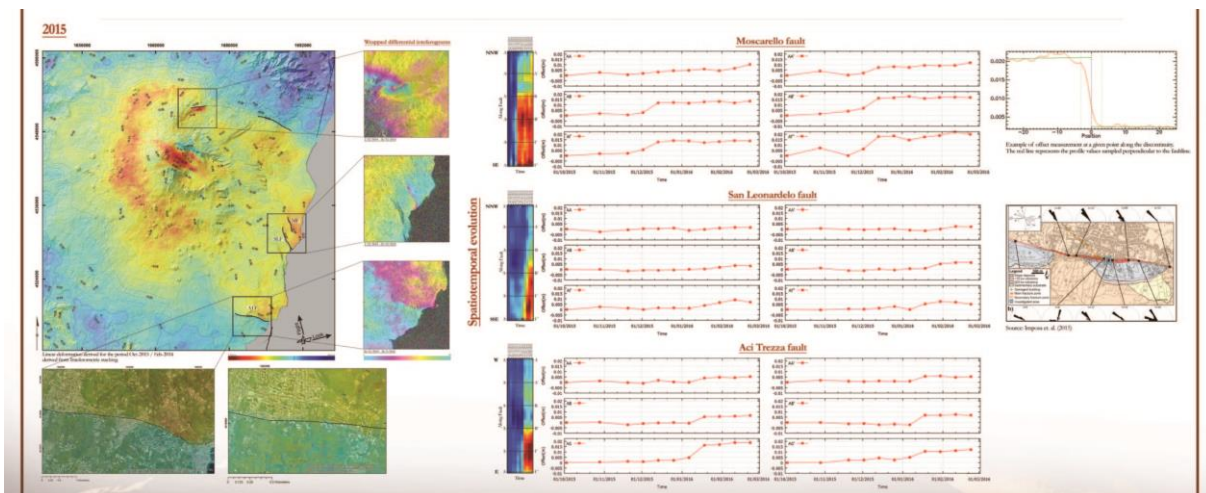


Figure 3.3 -2. Volcano deformation from Sentinel 1 interferometry. 2015 Etna eruption. Results presented at the MEDSUV final workshop 2016 as Derdelakos et al. (2016).

Co-supervision of the internship of Master student (M1) de Damien Raffard

The 2015, 4-months, internship focused on the potential of Diffused Scatterers differential interferometry (SQEESAR) for the long-term monitoring of CO2 storage sites. This innovative method makes it possible to measure the interferometric phase coherently on areas partially covered by the

vegetation, where usually the coherence of the InSAR signal is low. Damien, Master student at the Faculty of Applied Mathematics of the University of Orleans, was in charge of developing an IDL code that integrating the concept of Diffuse Scatterers Interferometry expressed in Ferretti et al. (2014). The results of this research internship are published in Raucoules et al., 2016.

Co-supervision of the internship of Master student (M2) Baptiste Ristori

Baptiste Ristori's course focused on the use of InSAR and image correlation methods for the measurement of the displacement field of the Machaze earthquake (Mozambique, Mw 7, 2006).

Baptiste combined C and L InSAR bands, from the Envisat and ALOS 1 sensors, to map and characterize the seismic fault. The results of this research internship are published in Raucoules et al., 2010.

Co-supervision of the internship of Master student (M2) Nadia Khezami

In 2007, we began to work on the first observations of correlation of optical images applied to the measurement of the ocean swell celerity from space. The internship of Nadia took place in 2008 for 4 months. She focused on the exploration of the cross correlation methods in this new field of application. Nadia mainly used the stereoscopic data acquired by the IKONOS and ASTER satellites to measure the celerity and direction of the ocean swell in two areas of application: offshore Guadeloupe (IKONOS) and the Gibraltar strait (ASTER). Nadia's work contributed to the implementation of the methodology that we later applied to SPOT5 and published in Michele et al. (2012). The importance of these methods lies in the possibility of measuring different couples "celerity" - "wavelength" for bathymetric restitution. This work led us to the work of de Michele et al. (2012) and Poupardin et al. (2014).

## 4. PRESENTATION and PERSPECTIVES of MY RESEARCH WORK

### 4.1 INTRODUCTION

In 15 years of research activity now, I concentrated on both methodological development and geophysical interpretation of the retrieved signal, in a diverse range of study areas and application fields. On the one hand, I used SAR, InSAR and optical image correlation to measure crustal deformation due to fault creep, large and moderate earthquakes, along with elastic dislocation modeling for the interpretation. I also co-authored few studies on volcano deformation on Mount Etna and Piton de la Fournaise. We attempted multi-disciplinary approaches by comparing SAR vertical displacement due to a large earthquake (Mw 7.8, Sichuan, China, 2008) with mass wasted via co-seismic landsliding to investigate mass balance and mountain building in the Longmen Shan (Parker et al., 2011). On the other hand, the impossibility of measuring fault displacements under water led me to the basic idea of “inter-band” optical correlation to retrieve bathymetry, which we further developed with A. Poupardin, D. Idier and D. Raucoules in the Bathysat project.

Furthermore, I got interested in the path of the SAR signal when an image is acquired at the very moment a volcanic eruption is ongoing. Is the signal delayed? Does ash particles motion induce a further Doppler shift on the initial SAR Doppler ? Can we measure it ? How lahars velocity impact hi-resolution SAR Doppler signal? I understood that the plume injection height is a crucial geophysical parameter in volcanology, which led me to the concept of using inter band optical stereoscopy to extract a digital elevation model of volcanic clouds, that we called “Plume Elevation Models”, PEM, in contrast to the renowned “Digital Elevation Model”, DEM. These last methods bring new geophysical information and a much improved exploitation of archived data in the field of multitemporal bathymetric studies and volcano monitoring.

Here follows a review of 5 papers published after my PhD.

### 4.2. Article n°1

#### **Volcanic Plume Elevation Model and its Velocity Derived From Landsat 8**

*Marcello de Michele, Daniel Raucoules, Þórður Arason*

A contribution from

*BRGM, Natural Risks Department, French Geological Survey, 45000 Orleans, France*

&

*Icelandic Meteorological Office, Reykjavík, Iceland*

The method presented in this article was conceived at BRGM within the context of MedSUV and Aphorism EU projects. The method is virtually applicable to all bushbroom systems but the choice of Landsat 8 was somehow opportunistic: the Holuhraun fissural eruption was ongoing and Landsat 8 captures it nicely. Also, Landsat 8 data represent “a difficult case” as the sensors are staggered on the focal plane of the instrument, which needs a dedicated pre-processing. We are grateful to USGS for providing us with raw Landsat 8 images. We thank Jim Storey for the FPM’s technical sheet, without it our study would have been impossible. We thank Claudia Spinetti and Stefano Corradini at INGV, Rome for all the discussions on volcanic cloud height and the importance of measuring it. The research leading to these results received funding from the European Community's Seventh Framework Programme [FP7/2007-2013] under the MED-SUV project: grant agreement n° 308665 and under the APHORISM project: grant agreement n° 606738.

#### Short description

In this study we present a method to reconstitute the volcanic gas/ash Plume Elevation Model (PEM) from optical satellite imagery. As the volcanic plume is moving rapidly, conventional satellite based photogrammetric height restitution methods do not apply as the epipolar offset due to plume motion adds up to the one generated by the stereoscopic view. This is because there are time-lags of tens of seconds between conventional satellite stereoscopic acquisitions, depending on the stereo acquisition mode. Our method is based on a single satellite pass. We exploit the short time lag and resulting baseline that exist between the multispectral (MS) and the panchromatic (PAN) bands to jointly measure the epipolar offsets and the perpendicular to the epipolar (P2E) offsets. The first are proportional to plume height plus the offsets due to plume velocity in the epipolar direction. The second, are proportional to plume velocity in the P2E direction only. The latter is used to compensate the effect of plume velocity in the stereoscopic offsets by projecting it on the epipolar direction assuming a known plume direction, thus improving the height measurement precision. We apply the method to Landsat 8 data taking into account the specificities of the focal plane modules. We focus on the Holuhraun 2014 fissure eruption (Iceland). We validate our measurements against ground based measurements. The method has potential for detailed high resolution routine measurements of volcanic plume height/velocity. The method can be applied both to other multi focal plane modules push broom sensors (such as the ESA Sentinel 2) and potentially to other push-broom systems such as the CNES SPOT family and Pléiades.

#### Why it is important to retrieve the height of a volcanic cloud?

The retrieval of both height and velocity of a plume is an important issue in volcanology. As an example, it is known that large volcanic eruptions can temporarily alter the climate, causing global

cooling and shifting precipitation patterns (e.g. Robock, 2000); the ash/gas dispersion in the atmosphere, their impact and lifetime around the globe, greatly depends on the injection altitude. . Plume height information is critical for ash dispersion modelling and air traffic security. Furthermore, plume height during explosive volcanism is the primary parameter for estimating mass eruption rate (e.g. Mastin et al., 2009). Knowing the plume altitude is also important to get the correct amount of SO<sub>2</sub> concentration from dedicated spaceborne spectrometers (e.g. Corradini et al., 2010; Carboni et al., 2012). Moreover, the distribution of ash deposits on ground greatly depends on the ash cloud altitude, which has an impact on risk assessment and crisis management. Furthermore, a spatially detailed plume height measure could be used as a hint for gas emission rate estimation and for ash plume volume researches, which both have an impact on climate research, air quality assessment for aviation and finally for the understanding of the volcanic system itself as ash/gas emission rates are related to the state of pressurization of the magmatic chamber (e.g. Urai, 2004; Hreinsdottir et al., 2014). Today, the community mainly relies on ground based measurements (e.g. Arason et al., 2011; Petersen et al., 2012; Scollo et al., 2014) but often they can be difficult to collect as by definition volcanic areas are dangerous areas (presence of toxic gases) and can be remotely situated and difficult to access. Satellite remote sensing offers a comprehensive and safe way to estimate plume height. The various techniques that can be used today either estimate average volcanic plume heights indirectly, based on wind speed for instance (see Sparks et al., 1997 for a review) or plume shadowing (e. g. Simpson et al., 2000; Spinetti et al., 2013), each of which do not aim at restituting a spatially detailed map of the plume heights. Conventional photogrammetric restitution based on satellite imagery fails in precisely retrieving a plume elevation model as the plume own velocity induces an apparent parallax that adds up to the standard parallax given by the stereoscopic view. Therefore, measurements based on standard satellite photogrammetric restitution do not apply as there is an ambiguity in the measurement of the plume position. Standard spaceborne along-track stereo imagers (e.g. SPOT 5, ASTER or Quickbird among the others) present a long temporal lag between the two stereo image acquisitions. It can reach tens of seconds for baseline-to-height ratios (B/H) between 0.2 and 0.5, during which time the surface texture of the plume may have changed due to the plume fast displacement (i.e. velocities larger than 10 m/s) biasing automatic cross correlation offset measurements (Kaab and Leprince, 2014). Urai (2004) succeeded in retrieving the plume height on Miyakejima volcano using ASTER stereoscopic view, on 3 specific points manually chosen on the forward and backward images. However, for the purpose of PEM extraction, the ideal is as small as possible time lag, with still a B/H ratio large enough to provide a stereoscopic view for restituting the height.

In the following paragraph we describe the main method.

In this study we propose to use the physical distance that exists between the panchromatic band (PAN) and a multispectral band (MS) in push broom spaceborne sensors to jointly measure the plume velocity and its height, at a high spatial resolution. A number of push broom sensors present a physical distance between the PAN and MS bands. This is because the PAN and MS Charge Coupled Devices (CCDs) sensors cannot coexist in an identical position on the focal plane of the instrument. This physical offset between the CCDs yields a baseline (i.e. the distance between the sensor positions when it acquires two images) and a time lag between the PAN and the MS bands acquisitions. On the one hand, the small baseline has already been successfully exploited for retrieving Digital Elevation Models (DEM) of still surfaces such as topography or building heights (e.g. Massonnet et al., 1997; Mai & Latry, 2009; Vadon, 2003). On the other hand, the time lag has been successfully exploited to measure the velocity field of moving surfaces, such as ocean waves and arctic river discharges (e. g. de Michele et al., 2012; Kaab et al., 2013; Kaab and Leprince, 2014; Poupardin et al., 2015). The problem of extracting a spatially detailed elevation model of a moving surface such as a volcanic gas/ash plume has not yet been addressed by common photogrammetric methods. The aim of this paper is to propose a method to address this problem. We propose a method based on a single pass of Landsat 8. We focus on the 2014-2015 Holuhraun fissure eruption (Iceland) as a test case.

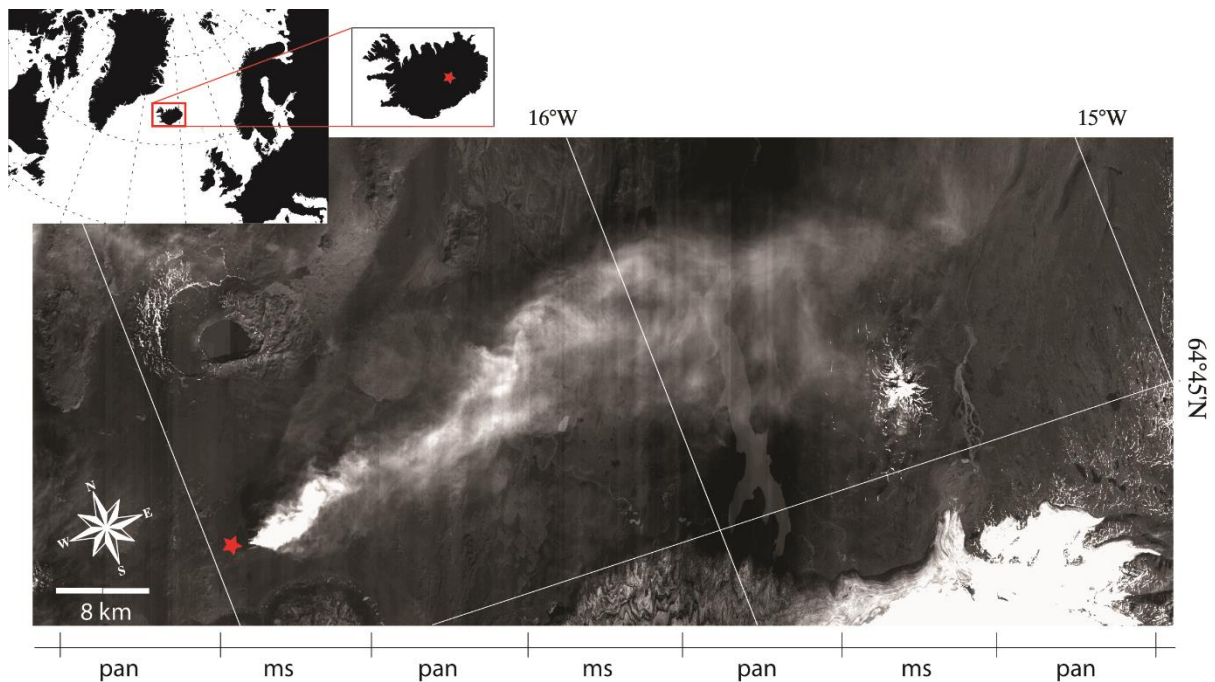


Figure 4.2 -1. The study area. Holuhraun (Iceland) eruption site (red star) and the volcanic plume from Landsat 8. The data were acquired on 6 September 2014 at 12:25 UTC.

The 2014-2015 Holuhraun eruption in the Bárðarbunga volcanic system is the largest fissure eruption in Iceland since the 1783 Laki eruption (Sigmundsson et al., 2015). It started at the end of August 2014 and lasted six months, to late February 2015. It has been characterized by large degassing processes and emission of SO<sub>2</sub> into the atmosphere (Gettelman et al., 2015; Haddadi et al., 2015). The eruption steam and gas column was nicely captured by the Landsat 8 on 6 September 2014 at 12:25 UTC (figure 4.2 1). The reasons why we use Landsat 8 data are manifold. Firstly, Landsat 8 captured the Holuhraun fissural eruption on a clear sky conditions. Secondly, raw Landsat 8 data are provided free of charge by the United States Geological Survey (USGS). Thirdly, Landsat 8 CCD sensors accommodation on the focal plane is somehow similar to the one employed by the ESA Sentinel-2, which is of high interest for the ash/gas plume research community as Sentinel-2 data will be free of charge and high revisit time. We chose the Holuhraun eruption as it represents a challenging test case for us as its plume was rapidly moving and reached low altitudes. Therefore, if our method works on the Holuhraun test case then it will apply to other types of volcanic plumes (higher and slower).

Now let’s describe the data that we are using and the system that collect them.

The Landsat 8 Operational Land Imager (OLI) is a push-broom (linear array) imaging system that collects visible, Near-InfraRed (NIR), and Short-Wavelength InfraRed (SWIR) spectral band imagery at 30-meter (15-meter panchromatic) ground sample distance (Storey et al., 2014). It collects a 190-kilometer-wide image swath from a 705-kilometer orbital altitude.

The OLI architecture is described as follows by Knight et al. (2014) and Storey et al. (2014). The OLI detectors are distributed across 14 separate Focal Plane Modules (FPMs), each of which covers a portion of the 15-degree OLI cross-track field of view. Adjacent FPMs are offset in the along-track direction to allow for FPM-to-FPM overlap. This is to avoid any gaps in the cross-track coverage. The reader should refer to figure 1 in Storey et al. (2014) for the OLI layout image. The important point in this study is that the internal layout of all 14 FPMs is the same, but with alternate FPMs being rotated by 180-degrees to keep the active detector areas as close together as possible. This has the effect of inverting the along-track order of the spectral bands in adjacent FPMs. Such an assembling of FPMs is rather frequent for multi-spectral sensors and is similar to the Sentinel-2 sensor. The OLI can be thought of as being composed of 14 individual sub-sensors, each of which covers approximately 1/14th of the cross-track field of view. Details of the OLI focal plane layout are presented by Knight et al. (2014) and Storey et al. (2014). USGS provide orthorectified Landsat 8 data free of charge and raw data on demand. Our analysis is based on RAW data.

This is the detailed method and the first results

We exploit both the time lag and the baseline between the PAN and MS image acquisitions. We chose the red channel as the PAN/red time lag is significantly larger than the PAN/blue time lag while the central frequency is closer to the PAN central frequency than the blue channel. The nominal PAN/red time lag is 0.52 seconds while the nominal angular separation is 0.3 degrees (Jim Storey, pers. Comm.). The platform flies at a nominal altitude of 705 km at a nominal speed of 7.5 km/s. So the base-to-height ratio ( $b/h$ ) is 0.0055. Alternatively, one might use the green channel instead of the red (which time lag is 0.65s).

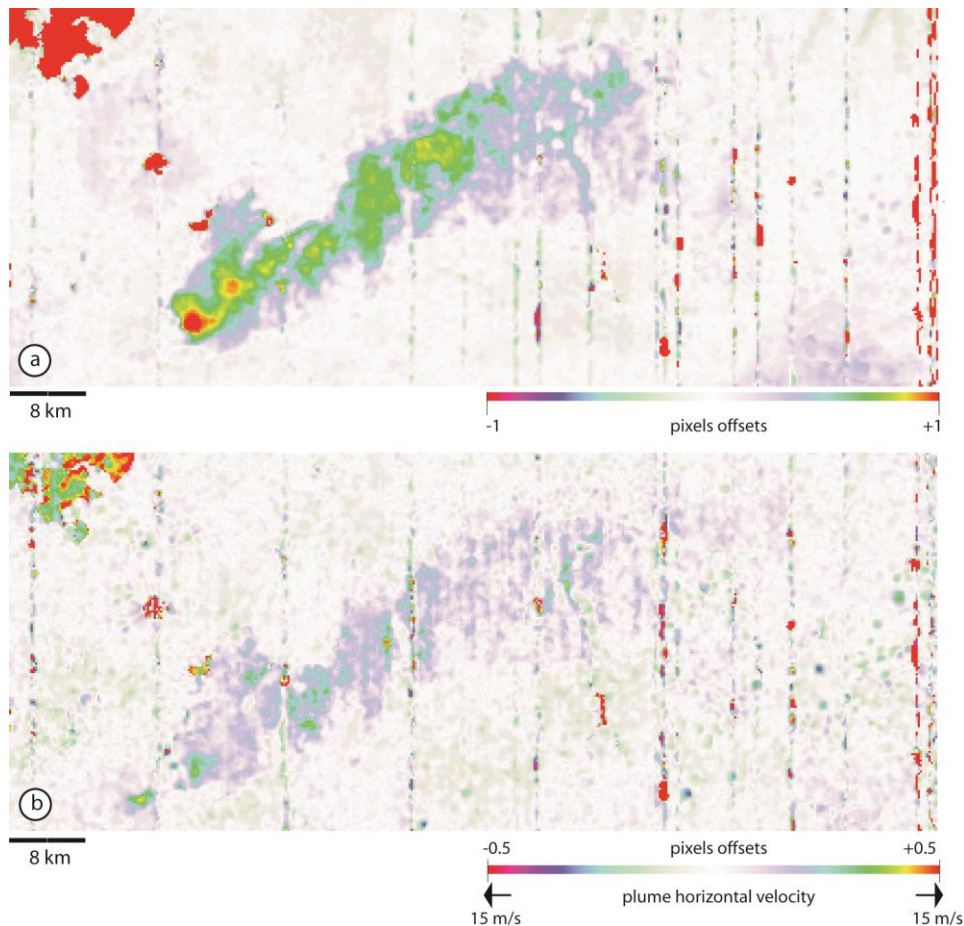


Figure 4.2 -2. Pixel offsets from correlation analysis. a) offsets in the epipolar direction due both to parallax and plume velocity in the along-track direction. b) P2E offset due to horizontal plume velocity in the P2E direction.

Things are a bit more complicated since the internal layout of all 14 FPMs is the same, but with alternate FPMs being rotated by 180-degrees. When measuring velocities from offsets from cross correlation techniques there will be a sign opposition between velocities measured on adjacent FPMs. To compensate for this, we propose the following approach; from raw data, instead of

assembling one PAN image and one MS image, we construct two mixed images. The first is made of alternate PAN-MS bands and the second is made of alternate MS-PAN bands from adjacent FPMs so that the time lag is kept at 0.52s without sign ambiguity (e.g. fig 4.2 1). The MS data are oversampled to match the PAN spatial resolution of 15 meters. Then, we perform offset measurements between the reconstructed images with the standard cross correlation approach (e.g. Leprince et al., 2007) (figure 4.2 2). We use a correlation window of 32x32 pixel size with 16 pixels sampling interval. This yields a 240 m pixel size offset grid. In a pioneering work, Urai (2004) proposed to use the P2E direction to estimate the wind speed and use this information to adjust the height estimation on 3 selected pixels belonging to the ash plume. The P2E offsets are independent of height, by definition. Therefore, offsets occurring in the P2E direction would be due to the motion of the observed surface in the P2E direction. By measuring the plume direction (i. e.  $\sim 30^\circ$  with respect to the P2E direction) we back-project the P2E offsets on the plume direction to retrieve plume velocity (figure 4.2 2b). The offsets in the epipolar direction (along track offset, figure 4.2 2a) are the sum of both a offset component proportional to the plume height and a component proportional to the apparent height due to the plume velocity.

We convert the formerly retrieved plume velocity to apparent height contribution. Finally, we compensate the apparent height contribution on the along track offset to retrieve the PEM (figure 4.2 3). We start by calculating the pixel offsets due to the plume height only:

$$O_h = O_e - O_{p2e} \tan \theta \quad [4.2 1]$$

where  $O_h$  is the pixel offset due to the plume height only,  $O_e$  is the pixel offset in the epipolar direction,  $O_{p2e}$  is the pixel offset in the P2E direction, and  $\theta$  is the angle between the plume major axis and the columns direction of the image matrix. From  $O_h$  we retrieve the PEM by applying (Urai, 2004)

$$h = O_h \cdot s \cdot H / (V \cdot t) \quad [4.2 2]$$

where  $h$  is the plume height (m),  $s$  is the pixel size (m),  $V$  is the platform velocity (m/s),  $t$  is the temporal lag between the two Landsat-8 bands (s) and  $H$  is the platform height (m). The results are shown in figure 4.2 3. We trace two profiles on the PEM and attempt a validation with ground truth data acquired by a web camera located in Kverkfjöll, about 25 km south of the plume. The comparison between ground based and space based measurements show that the PEM values are consistent. We show the results of the validation in figure 4.2 4. Besides, our method provides a spatially dense measure of the plume velocity at the PEM pixel sampling (240 m)

$$v_p = O_{p2e}S / (t \cdot \cos \theta) \quad [4.2\ 3]$$

where  $v_p$  is the velocity of the plume along its main axis (m/s).

For the 2014 Holuhraun eruption, we estimate a velocity between 7 and 12 m/s, which is consistent with ground based observation of the plume velocity on the same day as the Landsat 8 acquisition; the wind speed of the IMO numerical weather prediction model (Harmonie) at the surface (10 m a.g.l.) at Holuhraun on 6 September 2014 at 12:00 was 8.6 m/s (Arason et al., 2015).

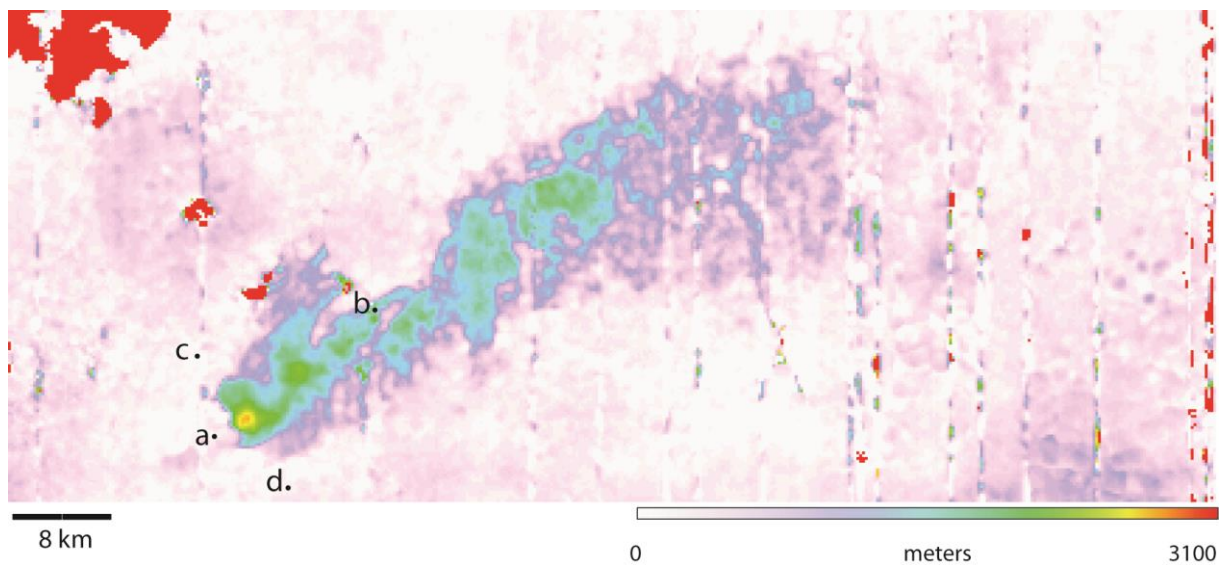


Figure 4.2 -3. The Holuhraun Plume Elevation Model on 6 September 2014 with a spatial resolution of 240 m per pixel. Location of the a-b and c-d elevation profiles in Fig. 4.2 -4 are shown.

#### Some methodological considerations

When creating images alternating Panchromatic and MS stripes, two issues can arise from both geometric and radiometric origin. The first is the alignment of successive stripes (resampled at the same sampling step). In our case, we proceeded by estimating shifts on the common overlapping columns of the two stripes (e.g. Panchromatic and Red) by simple image correlation. The second issue is the “calibration” of successive stripes of information acquired in different wavelengths and resolutions. We propose to proceed by adjusting the median values of successive image columns. Although the information is of different origin on the two successive stripes, the discontinuities between bands are little visible on the resulting mosaic images on land (figure 4.2 1).

Alternative methods could be implemented. We found that the actual resulting image product is suitable for the present application as it reduces the loss of information due to low correlation values when the correlator windows cross the borders between adjacent PAN/MS stripes.

#### A Discussion on the precision of the method.

In this section we discuss two sources of errors: the direct incidence of the expected inaccuracy of the offsets estimation on the height values and the incidence of the plume velocity correction. In terms of the error on the epipolar offset estimation, if we assume a theoretical correlator precision of 1/10 of pixel (Leprince et al., 2007), the resulting PEM precision (from equation [4.2 2] using the estimated B/H for Landsat 8) would be about 270 m. In terms of error due to insufficient velocity compensation, if we assume a theoretical correlator precision of 1/10 of pixel, the resulting error due to P2E offsets would be about 160 m. This estimation is sensitive to  $\tan \theta$ . As a consequence, the height measurement error will strongly increase with increasing  $\theta$ . This fact yields potential extreme situations when the volcanic plume is parallel to the satellite orbit, which PEM would be impossible to compute without neglecting the plume velocity. Surely, to overcome this problem one could combine both ascending and descending paths. Secondly, we can suppose a certain dispersion of the velocities about the average direction of the plume. For our case the dispersion is between 5° and 55° with average direction of about 25°. In this case, the vertical inaccuracy of the PEM can reach up to 380 m.

In the case one neglects the plume velocity, we can deduce that an uncompensated epipolar component of the velocity  $\delta v_p$  might result in an error  $\delta h$  given by (from equation [4.2 2])

$$\delta h = \delta v_p \left( \frac{H}{V} \right) \quad [4.2 4]$$

which yields  $\delta h \sim 100 \delta v_p$  for Landsat 8 data.

We highlight that most Low Earth Orbit (LEO) optical sensors relevant to this method share similar altitudes (600-800km) and speeds ( $\sim 7$  km/s). Therefore, the ratio  $\delta h / \delta v_p \sim 100$  gives an idea of the estimated error due to uncompensated plume epipolar velocity for most of the available LEO sensors. In the present test case (15 m/s maximum P2E velocity) if we do not correct for velocity contribution,  $\delta h$  would be about 860m. On the basis of the previous discussion, we are confident that our method can reasonably provide precisions in the interval 300-500m if the velocity component is well compensated.

Our PEM is validated against *in-situ* independent observations in the next section.

Comparison with *in situ* data: accuracy assessment

A web camera was located in Kverkfjöll (64°40'30"N, 16°41'23"W, elevation 1730 m a.s.l.), about 25 km south of the vent and almost perpendicular to the plume (Arason et al., 2015). The images are available every 10 minutes. The camera image area was scaled by identifying seven mountains visible on the images with elevations from 741 to 1682 m a.s.l. Assuming no lens distortion and that the plume drifted into direction 80° East of North, the plume top seen in the images can be transformed to height profile above sea level vs. distance along the plume. The camera view shows the plume during the first 19 km from the eruption site.

A comparison of the plume top altitude is shown in figure 4.2 4, where the web camera estimates at 12:20 and 12:30 UTC are shown as red dots with their temporal variation shown as error bars. We notice that the space based heights measurements are consistent with the ground based; the accuracy is better than 150m on the first 7 km from the eruption site.

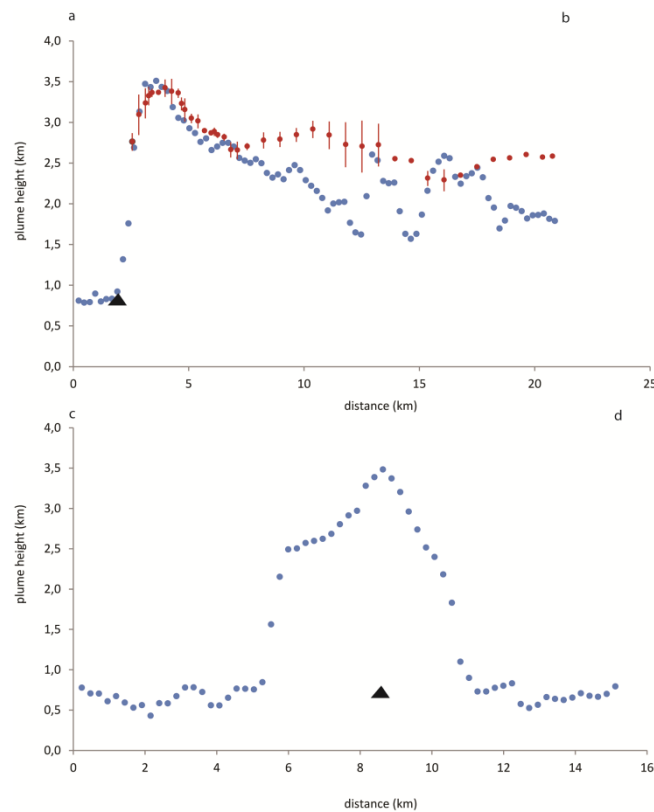


Figure 4.2 -4. Along-plume elevation profile a-b (top) and across-plume elevation profile c-d (bottom) (see location in Fig. 4.2 -3). The red circles represent the average of two ground camera measurements at 12:20 UTC and 12:30 UTC that we use for validation. The red bars indicate the difference between the two ground observations. The black triangles represent the location of the eruption site.

### Discussion and some conclusions

In this article we present a method to reconstitute the digital elevation model of a volcanic ash/gas plume. We apply the method to the 2014-2015 Holuhraun eruption and compare the results to ground-based observations (validation). The comparison yields a good fit, which makes us confident about the potential use of our method in remote access areas. Moreover, the method has potential for automation given that the procedure is relatively straight forward and the only input is the spaceborne imagery and associated metadata.

The produced PEM is consistent with ground observations for the first 7 km of the profile from the eruption site. The discrepancies are less than 150 m indicating that, in a range of a few km from the eruption site, our method appears to be accurate. The profile shows a height decrease starting at 3400 m over the eruption site and reaching 2500 m after 7 km. Then, between 7 km and 19 km, our PEM appears to be underestimated with respect to the ground observations by about 500 to 700m (i.e. height values vary between 1700 m and 2500 m). A possible explanation comes from the fact that the surface of the plume is very irregular (with possible local maxima and minima for the height). Seen from the ground, the height at a given point is obtained by the high and position of the plume in the line of sight of the camera - and therefore should not correspond to a local minimum of the plume’s upper surface as minima are occulted by higher elements of the plume. For the PEM, the values are extracted along a straight profile that could cross low areas of the plume occulted from the ground. That would result in an apparent underestimation. A second possible explanation can be proposed observing that far from the eruption site, the plume is more diluted, so we can see the ground through the plume on the images. A possible consequence of this, is the fact that features of the plume used in the image correlation process are deeper under the plume’s upper surface than in areas where the plume is denser. We might therefore estimate heights under the upper surface instead of the upper surface itself. Finally, we cannot reject the possibility that uncertainty of the plume velocities (values and directions) could affect our PEM estimates. Based on these considerations, we recommend the use of this method only when the mean angle between plume and orbit is larger than  $45^\circ$  with respect to the orbit azimuth angle. If it is not the case, auxiliary information (as wind speed data) is required to improve the PEM accuracy.

We measured the plume height with respect to the surrounding topography. Therefore, it is a relative height value with respect to the lowest topography within the scene. The sea could be taken as a reference “zero” value, if the sea is present in the satellite dataset. There is a need of absolute height calibration if the scene is devoid of sea. It can be done by including local topographic data (such as a DEM).

We developed this method on FPMs sensor such as Landsat 8 in the view of the use of Sentinel-2 data, where sensors are in a similar geometry on the focal plane. But our method can be applied directly to other –more linear- push broom sensors such as the CNES SPOT family (1980 – today) and Pléiades, which would improve the observation frequency, geographic coverage and number of data in archived inventories. The exploitation of these data archives would allow a study of past/present and future volcanic ash/gas columns.

#### 4.3. Article N°2

##### **Synthetic Aperture Radar (SAR) Doppler anomaly detected during the 2010 Merapi (Java, Indonesia) eruption**

*Marcello de Michele*<sup>1</sup>, *Daniel Raucoules*<sup>1</sup>, *Urs Wegmuller*<sup>2</sup>, *Christian Bignami*<sup>3</sup>

*A collaboration between*

<sup>1</sup> *BRGM, 3 Av. C. Guillemin, 45060, Orléans, France.*

<sup>2</sup> *Gamma Remote Sensing AG, Worbstrasse 225, CH-3073 Gümligen, Switzerland*

<sup>3</sup> *Istituto Nazionale di Geofisica e Vulcanologia, INGV, via di Vigna Murata 605, 00143, Roma, Italy.*

This work generated by the controversial observation that the Merapi 2010 eruption did not generated any volcanic edifice ground motion (the source was deep enough) while multi temporal SAR offsets tracking indicated a clear flank collapse. Therefore, we had the idea of digging into the SAR focusing procedure to look whether an eruptive related phenomenon could influence the SAR signal during a single image acquisition. This work has been partly supported by BRGM and partly by “MIAVITA” project, financed by the European Commission under the 7th Framework Programme for Research and Technological Development, Area “Environment”, Activity 6.1 “Climate Change, Pollution and Risks”. We thank P. Jousset for constructive comments on this topic and for bringing the 2010 Merapi eruption to our attention.

##### Short description

In this study we report the presence of a localized Doppler anomaly occurring during the focusing of a Radarsat-2 dataset acquired on the Merapi volcano (Indonesia) during the devastating 2010 eruption. The Doppler anomaly is manifested as a ~3km wide bull-eye shape azimuth pixels shifts between two sub-aperture images. The Doppler anomaly is centered on the summit-south flank of the Merapi volcano. The pixel shifts reaches up to 11.6 meters. Since the Merapi volcano was undergoing a large eruption during the data acquisition, it is possible that there is a volcano-related phenomenon that has delayed the radar signal so much to create measurable pixel offsets within a single SAR dataset, similar -but more extensive- to the signal generated by targets motions; similar -but less extensive- to

the signal generated by ionospheric perturbations. It is known that the SAR signal is delayed as it passes through heterogeneous layers of the atmosphere, but this delay typically affects the SAR signal to a fraction of the phase cycle or few centimeters depending on the radar wavelength employed by the system. We investigate the source of this anomalous metric signal; we review the theoretical basis of SAR image focusing and we try to provide a consistent physical framework to our observations. Our results are compatible with the SAR signal being perturbed during the actual process of image focusing by the presence of a contrasting medium located approximately between 6 and 12.5 km altitude, which we propose being associated with the presence volcanic ash plume.

### Context and introduction

In Synthetic Aperture Radar, variations in the Electro Magnetic Waves (EMW) travel time results in a change in the Doppler frequency that adds up to the one that is naturally generated by the relative motion between the platform and the ground targets. In Synthetic Aperture Radar, frequencies modulations control the image focusing along the two fundamental SAR directions, the azimuth (i.e. the platform motion direction) and the range (i. e. the sensor looking direction). During the synthetic aperture process (the so called image focusing) a target on the surface is seen along different paths. In standard focusing processing it is assumed both that ground targets are stationary and that between the sensor and the target the medium is the vacuum or a totally homogeneous medium. Therefore, if there is a significant path delay variation along the paths to a specific target this can result either in image defocusing or in pixel misregistration or both. As a special case, a path delay ramp across the synthetic aperture time would result in an offset in the azimuth pixels positions e.g. Cumming and Wong (2005), Breit et al., (2003). In particular, a ramp of one phase cycle across the standard synthetic aperture would result in an offset of one pixel in azimuth. Such a relative path delay might be caused by fluctuations of media properties in between the sensor and the surface, as already observed and discussed on L-band and C-band SAR data caused by dispersive ionospheric layers i. e. Gray et al., 2000, Meyer, 2009, Raucoules and de Michele, 2011, Wegmuller et al., 2006. In particular cases, further radar frequencies modulations can be induced by the own motion of specific radar targets such as vehicles e.g Breit et al., 2003. Moreover, a Doppler shift in ground based radar signal has been observed to be induced by volcanic ash plumes e. g. Valade and Donnadieu, 2011. In this study, we report a Doppler anomaly in Radarsat-2 SAR data occurring during the process of image focusing on data acquired over the Merapi volcano on the 30 of October 2010. The Doppler anomaly is so intense that it gives rise to measurable sub-aperture pixel offsets within a single radar image. The Merapi volcano was in activity during the Radarsat-2 SAR image acquisition (the 2010 centennial Merapi eruption). Therefore, we test the hypothesis that the Doppler anomaly might be induced by a volcano-related phenomenon.

The Merapi volcano is one of the 145 Holocene volcanoes that populate the Indonesian archipelago. It is located in the heart of the Sunda arc in Central Java, 30 km north of the city of Yogyakarta (fig. 4.3 1). With its ~3000 m height, it is one the most dangerous volcanoes in Indonesia, characterized by the persistent growth of the summit dome, intermitted by partial or total dome collapse to generate frequent *nuées ardentes* (e. g. Camus et al., 2000; Gertisser et al. 2001; Surono et al., 2012). Merapi re-awakened in late 2010, after four years of quiescence. The eruption started the 26 of October 2010 after nearly two months of enhanced levels of seismicity. Surono et al. (2012) reported that after an initial phase characterized by magmatic intrusions and shallow degassing, an explosive phase took place characterized by phreatomagmatic eruptions from the 26 of October to the 1<sup>st</sup> of November that produced a sustained eruptive plume.

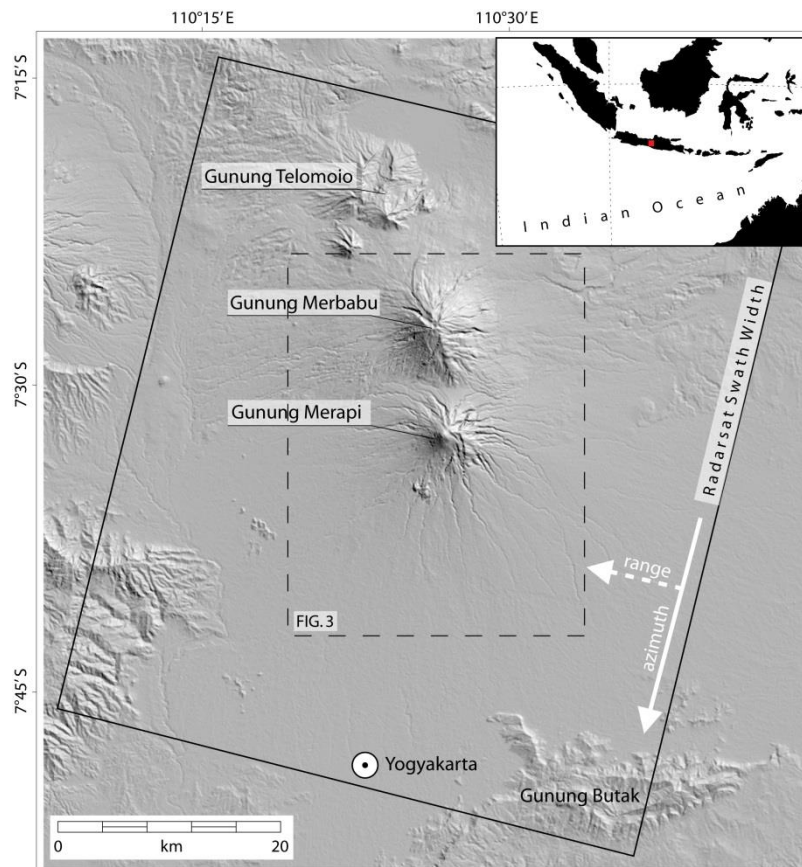


Figure 4.3 1. The study area. The black rectangle represent the RADARSAT swath width. Range and azimuth directions are indicated. The dashed rectangle is the footprint of figures 4.3 3.

We have used SAR data from the Canadian Space Agency C-band Radarsat-2 sensor acquired on the 30 of October 2010 (UTC), along with the sub-aperture offset-tracking method implemented in the

GAMMA codes Werner et al., 2000, to generate 2 sub-aperture SAR data. Our aim is to map azimuth sub-aperture sub-pixel offsets potentially due to systematic errors in the platform speed. Azimuth sub-band images correspond to consider SAR images with slightly different look directions. The resulting offset map (figure 4.3 3) substantially shows a localized pixel shift on the volcano summit and south-western flank that cannot be related to an error in the platform speed.

As former Merapi Volcano Observatory in Yogyakarta (BPPTK) reported the presence of explosions on the Merapi summit with a plume reaching several km height between 17:12 and 17:50 (UTC) on the 29 of October 2010, a possible hypothesis to explain the measured pixel offsets anomaly is to assume that there is a heterogeneous medium that locally delays the SAR signal during the data acquisition and hence causes pixel offsets. Effects are only expected for the data acquired on 30 Oct. 2010, when Merapi was erupting. Therefore, we concentrate on the Radarsat-2 data acquired the 30 of October 2010 at 22:11 (UTC) and we compare them to the data acquired by Radarsat-2 on the 06 of October 2010 (at 22:11 UTC -before the eruption started).

In the present manuscript, we firstly describe the method to measure the Doppler related azimuth shift anomaly. Secondly, we discuss the results and we propose a theoretic framework compatible to our observations. This is the first time that a space-borne SAR system is used to measure a Doppler anomaly related to volcanic activity.

#### Data description and methodological approach

Radarsat-2 data are acquired in F3 mode, vertical polarization, 43.43° look angle. While common Single Look Complex (SLC) SAR images are formed using the full length of the azimuth Doppler spectrum, the sub-aperture approach uses sub-aperture images derived from different segments of the azimuth Doppler spectrum calculated from the SLC SAR data. Each of the sub-aperture images (or ‘looks’) is formed from a bandwidth equal to 0.35 times the radar Pulse Repetition Frequency (PRF) yielding a frequency separation between the looks of 0.45 times the PRF. The idea is that as the sub-aperture images observe the same object on ground from slightly different locations along the orbit they ‘see’ through different parts of the volcanic plume. A difference in the Doppler gradients at these locations induces systematic small scale azimuth and range offsets between the two sub-aperture images resulting in relative shifts between the looks, which can be detected by cross-correlation methods. The sub-aperture images are firstly generated. Then, they are cross-correlated using 2D Fast Fourier Transform to measure the range and azimuth pixel offsets with a window size of 256 pixels every 64 SLC pixels. A biquadratic interpolator determines the offset correlation peak

with sub-pixel accuracy. The processing code that we adopted here is the one implemented in the GAMMA “autofocus of SLC” code Wegmuller et al., 2006.

Based on Su et al., 2013 and the work from Meyer, 2009, we can propose a set of relationships between the signal path lengthening  $l$  and the sub-aperture pixel offsets:

$$\Delta r_a (m) = V \Delta T \frac{h}{H} \frac{\partial l}{\partial x} \quad (4.3 1)$$

$$\Delta \eta (m) = \frac{2V^3 \Delta T}{\lambda_{FM}} \left( \frac{h}{H} \right)^2 \frac{\partial^2 l}{\partial x^2} \quad (4.3 2)$$

where  $\Delta \eta$  are the sub-aperture azimuth offsets (units, m),  $\Delta r_a$  are the sub-aperture slant range offsets (units, m),  $V$  is the platform velocity (units m/s),  $\Delta T$  is the time separation between the two looks,  $FM$  is the instrument Doppler rate, and  $x$  is along track coordinate of the measured anomaly (units, m).

We propose to introduce the ratio  $h/H$  in the formula. It reflect the fact that a given time interval between sub-apertures corresponds to different along-orbit path lengths depending on the height  $h$  of the disturbing phenomenon.  $H$  is the height of closest approach (i. e. the vertical distance between the orbit and the target) and  $h$  is the height between the ground target and the source of the Doppler anomaly. Figure 4.3 2 summarizes the geometric meaning of the aforementioned variables.

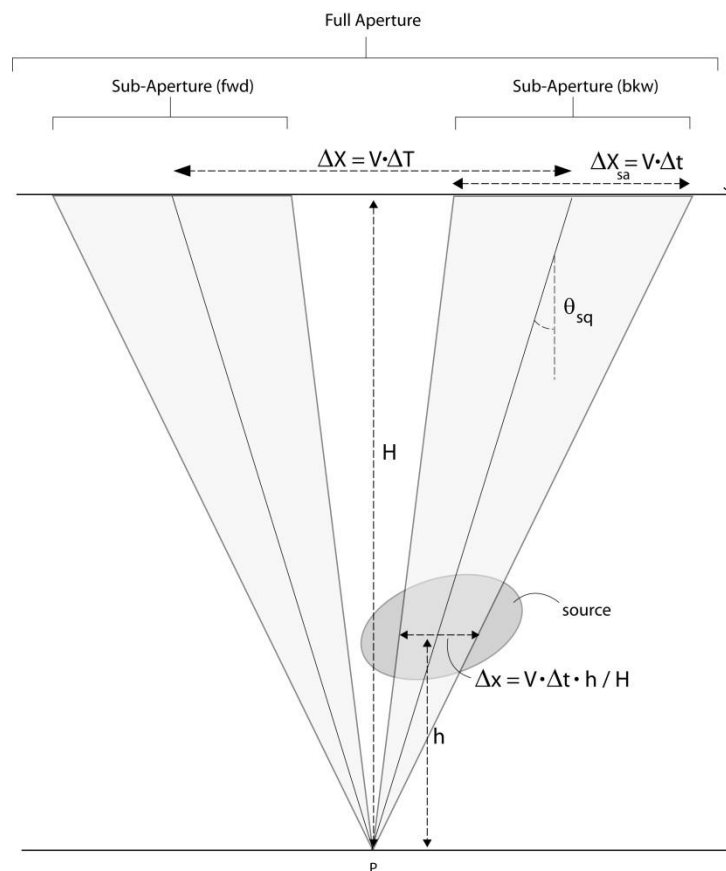


Figure 4.3 2: Geometry of the sub-aperture acquisition.  $\Delta T$  is the time separation between looks,  $\Delta t$  is the sub-aperture integration time,  $V$  is the along track velocity of the platform,  $\theta_{sq}$  the squint angle of the sub aperture

look.  $H$  is the distance between ground surface and the sensor.  $h$  is the Line of Sight distance between the ground target and the disturbing atmospheric phenomenon.

### First Results

The sub aperture cross-correlation method applied to the SAR data acquired on the 30 of October 2010 UTC shows a distinct azimuth and range offsets signal on the summit and South Western flank of mount Merapi (Figure 3a, b). The sub-aperture azimuth offset is as high as +11.6 meters (positive towards the sense of platform motion, indicating wave path lengthening). The sub aperture cross-correlation applied to the SAR data acquired on the 06 of October 2010 UTC does not show a consistent azimuth or range offsets signal on the summit and south western flank of mount Merapi (Figure 4.3 3c, d). Therefore we are measuring a non-stationary Doppler anomaly that appears in concomitance with the Merapi volcano eruption.

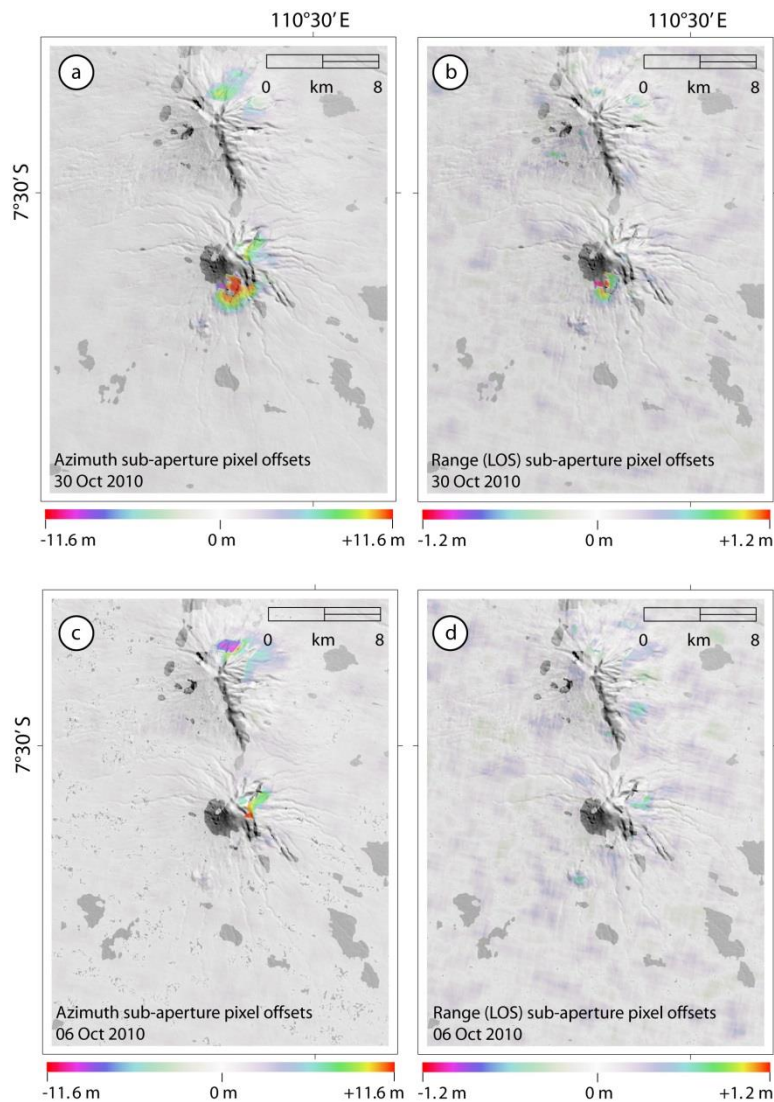


Figure 4.3 3. Pixel offsets measured by sub-aperture cross correlation calculated on the SAR data acquired on the 30 of October 2010 during the Merapi volcano eruption; a) azimuth direction, b) range direction. Apparent pixel offsets measured by sub-aperture cross correlation calculated on the SAR data acquired on the 06 of October 2010, before the Merapi volcano eruption; c) azimuth direction, d) range direction.

This evidence leads us to interpret the azimuth sub-aperture offset as the result of a localized delay in the SAR signal caused by strong heterogeneities within the Merapi summit atmosphere occurring on the 30 of October 2010 (UTC). This SAR signal anomaly correlates in date and approximate location with the occurrence of the volcanic plume observed visually and instrumentally by BPPTK on the 29 of and 31 of October 2010 UTC (Surono et al., 2012). However, one has to consider that with the side-looking SAR geometry the anomaly is not observed at the exact locations of the ash but "behind it" where the radar waves propagating through the ash are scattered from the ground. Given its relative limited areal extension, we tend to exclude that this Doppler anomaly can be originated by atmospheric gravity waves or small scale TEC (Total Electron Content) variations, which assessed influence on the radar signals in the higher atmospheric levels would result in wider scale SAR azimuth offsets e.g. Leu and Chang, 2005. To test our hypothesis we make a combined use of equations 4.3 1) and 4.3 2) to provide us with some hints about the absolute signal path lengthening, which we could relate to the average height of the source of the Doppler anomaly.

Some elements for signal interpretation in terms of path lengthening

In order for us to assess the consistency of the observed anomaly with a possible volcano-related atmospheric phenomenon, we propose to simplify the problem as follows. Let us approximate the measured  $\Delta\eta$ ,  $\Delta r_a$  and  $l$  by Gaussian functions having the same  $\sigma$  value corresponding to approximately half of the anomaly width ( $\sigma = \sim 1500$  m, from figure 4.3 3a, b). Let call  $A$  and  $B$  the measured maximal sub-aperture offsets (azimuth and range respectively). Let  $C$  be the maximal absolute signal lengthening to be estimated:

$$l(x) = C e^{-\frac{x^2}{2\sigma^2}} \quad (3)$$

In order to be consistent with equations (4.3 1) and (4.3 2), we propose the following approximations for  $\Delta\eta$ ,  $\Delta r_a$  based on the areal size of the measured anomaly and the maximum values  $A$  and  $B$  measured on our offsets results:

$$\Delta r_a(x) = B \frac{x}{\sigma} e^{-\frac{1}{2} - \frac{x^2}{2\sigma^2}} \quad (4.3 4)$$

(this guaranties that the maximum value of  $\Delta r_a$  is  $B$ )

$$\Delta\eta(x) = A \left(1 - \frac{x^2}{\sigma^2}\right) e^{-\frac{x^2}{2\sigma^2}} \quad (4.3 5)$$

By deriving equation (4.3 3) we obtain:

$$\frac{\partial l}{\partial x} = -C \frac{x}{\sigma^2} e^{-\frac{x^2}{2\sigma^2}}$$

$$\frac{\partial^2 l}{\partial x^2} = \frac{C}{\sigma^2} \left( \frac{x^2}{\sigma^2} - 1 \right) e^{-\frac{x^2}{2\sigma^2}}$$

Therefore, from (4.3 1) and maximizing each side of the equation, we obtain:

$$\frac{B}{\sqrt{e}} = -V \Delta T \frac{h}{H} C \frac{1}{\sigma}$$

$$C = - \frac{\sigma B \sqrt{e} H}{V \Delta T h} \quad (4.3 6)$$

From (4.3 2) we obtain:

$$A = \frac{2V^3 \Delta T}{\lambda FM} \left( \frac{h}{H} \right)^2 \frac{C}{\sigma^2}$$

$$C = \frac{\lambda FM \sigma^2}{2V^3 \Delta T} \left( \frac{H}{h} \right)^2 A \quad (4.3 7)$$

By fixing  $\lambda=0.056 \text{ m}$  (C-band wavelength);  $H=759201 \text{ m}$  (altitude of Radarsat-2 platform);  $A=1.6 \text{ m}$  (measured);  $B=0.7 \text{ m}$  (measured);  $FM = 1773 \text{ Hz/s}$ ;  $\Delta T = 0.8\text{s}$  (sub aperture time interval);  $\sigma = 1500 \pm 500 \text{ m}$ , we can plot  $C$  as a function of  $h$  from equation (4.3 6) and (4.3 7). We found that the sub-aperture anomalous pixel shifts can be compatible with a source located in between 6 and 12.5 km altitude yielding an absolute wave path delay between  $\sim 19$  and  $\sim 25$  meters (figure 4.3 4).

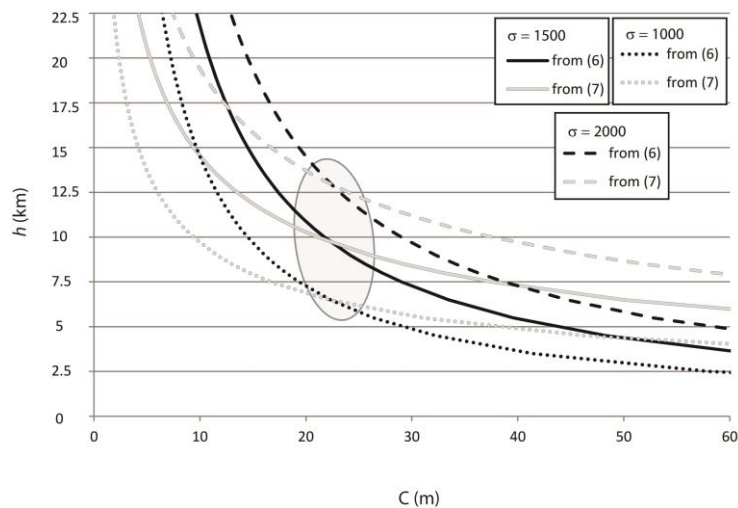


Figure 4.3 4. Plot of  $C$  (absolute path length in slant range) as a function of  $h$  (relative height of the source) from equations (4.3 6) and (4.3 7) we propose that the Doppler anomalous values can be compatible with a source located in between 6 and 12.5 km altitude, yielding an absolute wave path delay between  $\sim 19$  and  $\sim 25$  meters.

The solution is calculated for 3 different values of  $\sigma$  (1 km, 1.5 km, 2 km) to give an idea of the influence of the uncertainty to the proposed solution. Fixed parameters:  $l=0.056$  m;  $H=759201$  m;  $A=11.6$  m;  $B=0.7$  m;  $FM = 1773$  Hz/s;  $\Delta T = 0.8$ s.

The solution is very sensitive to  $\sigma$  so that the solution range is large because of the uncertainty on the measurements. Simplifications and approximations to derive (4.3 6) and (4.3 7) from the previous equations are additional sources of uncertainty. Nevertheless, we think that this approach is helpful to discriminate between a upper or lower atmospheric source. The solution is also sensitive to the system  $FM$  (Doppler rate) in the sense that a high  $FM$  would generate less azimuth pixels shifts -given other parameters as fixed. This observation leads to foreseen strong potential differences in results obtained using different sensors. An absolute wave path delay between  $\sim 19$  and  $\sim 25$  meters means that a range pixel is imaged between 19 and 25 meters away on the LOS from its ‘true’ position. In a general case, one could validate the measured  $C$  value by measuring the LOS pixel shift between two SAR dataset acquired on two different dates. Unfortunately, the violent dome explosions during the Merapi eruption caused the modification of the summit rim morphology and surface changes due to pyroclastic flows. Therefore, the backscattering elements before and during the eruption are not the same so that  $C$  cannot be measured directly due to high degree of surface changes.

#### Discussion and some conclusions

Sub-aperture pixel offsets technique allowed us to highlight an anomaly on the Doppler parameters estimation of a Radarsat-2 SLC data acquired on the 30 of October 2010 (UTC) over Merapi volcano. Sub-aperture pixel offsets reaches 11.6 meters in the azimuth direction (positive towards the platform sense of motion). At that time, Merapi volcano was undergoing an eruptive explosive phase. Sub-aperture pixel offsets technique applied to the Radarsat-2 dataset acquired before the eruption started (06 October 2010) does not reveal any areal extensive Doppler anomaly. Therefore, we are inclined to think that there is a volcano-related phenomenon that has consistently delayed the SAR signal during the actual process of image acquisition. Our measurements are compatible with the presence of a heterogeneous medium located on top south western flank of the Merapi volcano between  $\sim 6$  and 12.5 km altitude that influenced the SAR signal so much to cause measurable sub-pixel offsets during image focusing. Both volcanic ash cloud particles and plumes can delay radar waves as already observed with Global Positioning System e.g. Houlié et al., 2005. Therefore, we propose that the SAR signal might be perturbed by the presence volcanic plume on the 30 of October 2010 (UTC), which has been observed on the ground and instrumentally. In this study we do not take into account the influence of particles/target owns motions on the SAR Doppler

measurements but in the future we should investigate SAR Doppler anomalies induced by rapid mass movements (such as surges and pyroclastic flows) occurring during the synthetic aperture as well as the influence of Doppler anomalies generated by plume particles motions as already observed by ground based radars e. g. Valade and Donnadieu, 2011. This paper calls to a more careful interpretation of surface displacement derived from SAR sub-pixel offsets in regions of exacerbated volcanic phenomena.

#### 4.4. Article N°3

##### **Revisiting the shallow Mw 5.1 Lorca earthquake (southeastern Spain) using C-band InSAR and elastic dislocation modelling**

Marcello de Michele a, Pierre Briole b , Daniel Raucoules a , Anne Lemoine a, Alexis Rigo c

A collaboration between

a French Geological Survey (BRGM) , 45060 , Orléans , Cédex 2 , France

b Laboratoire de Géologie , CNRS UMR 8538, Ecole Normale Supérieure , 75231 , Paris , Cédex 05 ,  
France

c IRAP – UMR 5277, CNRS – Université de Toulouse, Observatoire Midi-Pyrénées , Observatoire ,  
31400 , Toulouse , France

In my personal opinion, this article is important because (among other more “tectonic related” reasons) it presents a method to extract interferometric phase from atmospherically biased (and sparse) SAR data. The potential application to Sentinel 1 might be of interest for the community. We thank ESA, BRGM Research Direction for funding this research.

#### Short introduction

Space geodetic techniques such as interferometric synthetic aperture radar (InSAR) and global positioning systems (GPS) have demonstrated to be useful in mapping the displacement fields of large earthquakes (moment magnitude ( $M_w$ )  $\sim 6$  or higher). However, the displacement fields of smaller earthquakes ( $M_w < 5.5$ ), such as those that typically result from the collision of the European and African plates, are less often analysed by space geodetic techniques, and their characterization, in terms of slip along the fault plane at depth and focal depth location, often challenges current seismological techniques. This letter presents the results of InSAR analysis of the 11 May 2011, Mw 5.1, Lorca earthquake. The Lorca earthquake occurred close to an area undergoing rapid subsidence

due to sediment compaction related to water pumping. Therefore, it is challenging to separate the InSAR signals due to the earthquake from those due to human activity. We used four sets of SAR data acquired from the European C-band Advanced SAR (ASAR) sensor on board the Environmental Satellite (ENVISAT) to map the surface-displacement field in the Lorca region. Then, we use a simple elastic dislocation model to characterize the fault plane geometry and the fault slip at depth. We find that the InSAR signals can be explained by  $\sim 21$  cm reverse slip with a  $\sim 6$  cm left-lateral component on a  $3 \text{ km} \times 3 \text{ km}$  segment centred at  $4.2 \text{ km}$  depth dipping  $45^\circ$  NW and striking  $N65^\circ$  E, consistent with the rupture of a segment of the Alhama de Murcia fault and consistent with recent published analyses. Interestingly, the InSAR signal can also be explained by  $\sim 21$  cm reverse slip with a  $\sim 6$  cm left-lateral component on a  $3 \text{ km} \times 3 \text{ km}$  segment centred at  $\sim 4.2 \text{ km}$  depth dipping  $50^\circ$  SE and striking  $N230^\circ$  E, consistent with preliminary focal plane solutions indicating a rupture on a previously unmapped blind structure. We conclude that the second model cannot be rejected on the base of the InSAR results, the complex surface-displacement pattern (containing both seismic and non-seismic displacement), the different preliminary moment tensor solutions and the published locations of aftershocks at depth.

### Introduction

The moment magnitude ( $M_w$ ) 5.1 Lorca earthquake (Murcia region, Spain) occurred on 11 May 2011 and ruptured a segment of the Alhama de Murcia fault (AMF) system. Preliminary seismological analyses from the Euro Mediterranean Seismological Center (EMSC) indicated a reverse slip mechanism on a relatively steep fault plane ( $\sim 65^\circ$ ) at a shallow depth of  $\sim 2 \text{ km}$  (EMSC 2011). Initial moment tensor solutions also suggest that the Lorca earthquake could have occurred on one of the two families of fault planes. The first family from the Spanish Instituto Geográfico Nacional (IGN), the Instituto Andaluz de Geofísica (IAG), the Global Centroid Moment Tensor solution (GCMT) and the University of Nice (Geoazur) is consistent with a rupture on a plane striking  $N65^\circ$  E and dipping NW. The second family from the Italian Instituto Nazionale di Geofisica e Vulcanologia (INGV), the German Geo Forschungs Zentrum (GFZ) and the US Geological Survey (USGS) is consistent with a plain striking  $N230^\circ$  E and dipping SE. The AMF zone is a 100-km-long reverse strike–slip fault composed of several segments trending NE–SW (from  $N45$  to  $N65$ ) that started developing within the internal zone of the eastern Betic Cordillera during the late Miocene (e.g., Martínez-Díaz 2002, Masana *et al.* 2004). Geomorphically, the AMF forms the northwestern boundary of the Guadalentin depression (figure 4.4 1). Structurally, the AMF has been a major player during different phases of inversion tectonics related to the Alpine Orogeny (particularly from upper Miocene to present) in the Murcia region and is believed to have controlled extensional basin formations along the Betic Cordillera (Meijninger and Vissers 2006). Geodynamically, the AMF has recorded a regional stress field that is compatible with

the NNW–SSE horizontal compression since the late Miocene (Galindo-Zaldívar *et al.* 1993, Martínez-Díaz 2002, Masana *et al.* 2004), in agreement with the present-day regional shortening direction (e.g., DeMets *et al.* 1990, Nocquet and Calais 2003). Seismically, the AMF is an active fault capable of Mw 6.5–7 earthquakes, as revealed by palaeoseismology on the Lorca–Totana segment (Masana *et al.* 2004). The area is characterized by a high rate of subsidence due to sediment compaction triggered by water pumping in the Guadalentín basin (González and Fernández 2011).

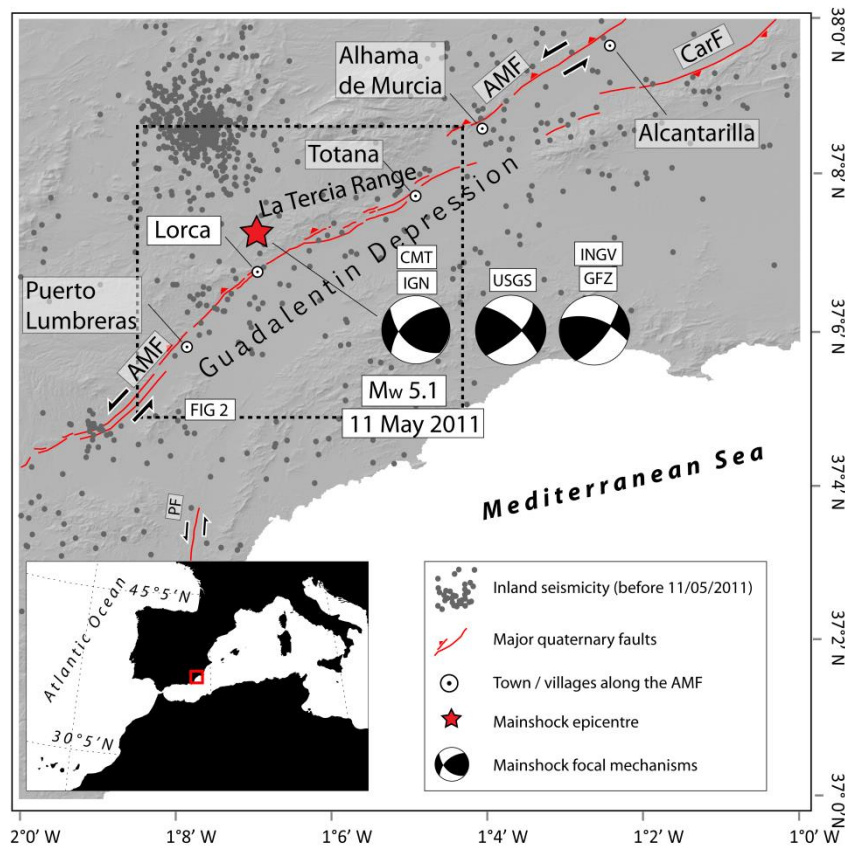


Figure 4.4 1. The study area. Locations of quaternary faults in red (after Martínez-Díaz (2002)). Seismicity recorded by IGN network before May 11, 2011, is shown in grey. The epicenter (red star) and the focal mechanisms of the main shock are as determined from the IGN moment tensor solution, INGV, GFZ and GCMT.

AMF: Alhama de Murcia Fault; PF: Palomares Fault; CarF: Carrascoy Fault.

Recent studies based on seismological analysis (Lopez-Comino *et al.* 2012) and interferometric synthetic aperture radar (InSAR) analysis (Frontera *et al.* 2012, González *et al.* 2012, Martínez-Díaz *et al.* 2012a, 2012b) have pointed towards a fault model consistent with the IGNSolution for the 2011 Lorca earthquake. Still, given the difficulty of separating coseismic displacement from the long-term surface subsidence and noises, an open question remains as for the capability of InSAR to discriminate between the two families of seismogenic fault planes in Lorca. This study focuses on

characterizing the fault segment responsible for the Lorca earthquake by applying the InSAR technique (e.g., Massonnet and Feigl 1998) to data from the European Space Agency (ESA) Advanced SAR (ASAR) sensor on board the Environmental Satellite (ENVISAT) satellite. The challenges of this study are twofold. First, this research aims to investigate whether ENVISAT ASAR C-band InSAR method can be used to quantify the displacement field of a shallow Mw 5.1 earthquake in the presence of both high-rate and long-term subsidence due to water pumping and atmospheric disturbances in the InSAR data. Second, we investigate whether an elastic dislocation model can provide a good explanation of the observed displacement field and whether the model parameters are consistent with the independent seismological observations. In addition, we investigate whether the InSAR signal generated by the Lorca earthquake can be explained by slip at depth on the second family of fault planes.

#### Data and methodology

We used four ASAR C-band scenes from track 8 in IS2 mode (23° off the vertical line of sight (LOS)) acquired between November 2010 and June 2011, after the ENVISAT extension orbit was implemented (ESA 2011). From these data, six differential interferograms were calculated (table 1); four of which contain the displacement field of the Lorca earthquake, and all six cover the extent of the subsidence in the Guadalentin basin. Two interferograms (one before and one after the quake) were used to verify that the InSAR signal outside the coseismic window is not due to the earthquake. The maximum perpendicular baseline was 267 m. Therefore, the Shuttle Radar Topography Mission (SRTM) 90-m digital elevation model (DEM) is sufficient to remove the topographic contributions to the interferometric phase from each interferogram. We used the GAMMA minimum cost flow (MCF) algorithm (Costantini and Rosen 1999, Werner *et al.* 2002) to unwrap the interferograms. To help MCF, we created a multiple-look interferogram and used it as a phase reference model. For each pixel, the unwrapped phase value was set to a value which is within the interval ( $\pm\pi$ ) of the phase reference model (Werner *et al.* 2002). Depending on atmospheric conditions, the SAR path delay might have an altitude dependence caused by changes in the atmospheric water vapor and pressure profiles between the acquisitions of the interferometric image pairs. Therefore, the GAMMA *atm\_mod* algorithm was used to determine the linear regression coefficients of the residual phase with respect to height in the unwrapped interferograms. The DEM was used to generate the phase model of the height-dependent atmospheric phase delay for each unwrapped interferogram, and then the phase model was subtracted from the corresponding single interferogram. Such a procedure also reduces possible unaccounted-for orbital uncertainties that could be due to a linear dependency to the perpendicular baseline of the SAR signal. The Guadalentin basin is known to be affected by high subsidence rates ( $\sim 0.8$  cm month<sup>-1</sup>), due to aquifer compaction caused by intensive

water pumping (González and Fernández 2011). Therefore, the subsidence signal was expected to be clearly visible in our InSAR analysis. We calculated the subsidence rate,  $\phi_r$ , over the period of observation of the four interferograms  $\phi_j$  ( $j = 1$  to 4) that contain the displacement field of the Lorca earthquake:

$$\phi_r = \frac{\sum_{j=1}^N \Delta t_j \phi_j}{\sum_{j=1}^N \Delta t_j^2} \quad (4.4 1)$$

where  $N$  is the number of interferograms and  $\Delta t_j$  is the time separation between the two radar scenes (Le Mouélic *et al.* 2005). This procedure further reduces the atmospheric contribution to the interferometric phase and makes it possible to evaluate the subsidence rate due to water pumping. Then, an estimate of the Lorca earthquake displacement field,  $\phi_k$ , could be extracted by considering it as being identical on all the interferograms for the period of observation:

$$\phi_k = \phi_r \frac{\sum_{j=1}^N \Delta t_j^2}{\sum_{j=1}^N \Delta t_j} \quad (4.4 2)$$

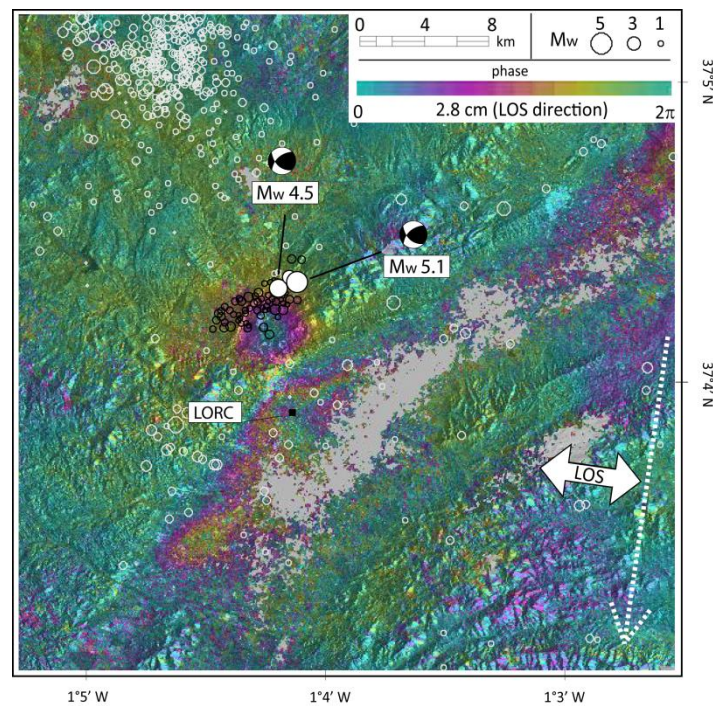


Figure 4.4 2. Surface displacement due to both the Lorca earthquake and 5.2 months of water pumping in the Guadalentin basin (DEM in semitransparent fill). Transparent white circles represent instrumental seismicity (IGN catalogue) and magnitudes before 11 May 2011; solid white circles represent the locations and magnitudes of the main shocks. Black circles represent the relocated aftershocks (after Lopez-Comino *et al.*, 2012). The main shocks,  $M_w$  4.5 and  $M_w$  5.1 on 11 May 2011, are plotted with their respective focal

mechanisms. In the grey area, the InSAR data were lost due to signal incoherence. The color fringe corresponds to  $2\pi$  radians phase variation, i.e., 2.8 cm in the line of sight (LOS) direction ( $23^\circ$  off the vertical). The black square is the location of the permanent LORC GPS station. DMS coordinates.

Figure 4.4 2 shows the displacement field of the Lorca earthquake; on the same map, the ground subsidence due to water pumping in the Guadalentin basin over an equivalent period of observation given by

$$\frac{\sum_{j=1}^N \Delta t_j^2}{\sum_{j=1}^N \Delta t_j} \approx 5.2 \text{ months} \quad (4.4 3)$$

The modelling process began with a forward approach. We used the physical theory proposed by Okada (1985), as implemented in the code by Briole *et al.* (1986), for predicting the results of InSAR observations. The process started with a set of *a priori* information on fault geometry obtained from seismology and structural geology. A trial-and-error approach was used, looking for the forward model that could best reproduce the InSAR displacement field in agreement with published seismological interpretations (Lopez-Comino *et al.* 2012). Once the forward model configuration was satisfactory, we fixed the strike and the dip of the fault, and we performed an inversion to obtain the slip, depth, width and length. The inversion was based on the Tarantola–Valette method (Tarantola and Valette 1982) and was implemented in the *inverse5* code as described by Briole *et al.* (1986). We used a set of 104 input data points from the InSAR displacement field (1 sample every 1 km along a  $\sim 10 \text{ km} \times 10 \text{ km}$  grid). As there was a disagreement among the very first moment tensor solutions, we tested several forward models based on the fault plane geometry initially suggested by INGV, GFZ and USGS.

## Results

Our best model (figure 4.4 3, table 4.4 2) in terms of both data fitting and agreement with published seismological/InSAR interpretations (Vissers and Meijninger 2011, Frontera *et al.* 2012, González *et al.* 2012, Lopez-Comino *et al.* 2012, Martínez-Díaz *et al.* 2012a, 2012b) is consistent with slip on the northern segment of the AMF, which dips to the NW. The results suggest that the Lorca earthquake ruptured a 2.9-km-long  $\times$  2.9-km-wide asperity belonging to a  $N65^\circ$  E oriented fault centred at 4.2 km depth and dipping  $45^\circ$  to the NW. The model proposed here indicates  $\sim 22$  cm coseismic slip partitioned into 21 cm reverse slip and 6.5 cm left-lateral slip (rake  $77^\circ$ ), which produced up to  $3 \pm 0.5$  cm of surface displacement in the LOS direction. Noise standard deviation in the stacked interferogram corresponds to 0.5 cm displacement.

We consider the modelled results as acceptable if the residual locally falls within plus or minus one standard deviation of the original observations. Our model suggests a seismic moment (Kanamori 1977) of  $5.55 \times 10^{16}$  Nm, which is in good agreement with the seismic moment deduced from seismological observations, yielding a Mw of 5.1. The residuals (figure 4.4 3) show that the model satisfactorily reproduces the observations, except for a large fringe pattern within the Guadalentín basin that can reasonably be attributed to sediment compaction caused by water-pumping activities, as described by González and Fernández (2011). In this area, we measured a subsidence rate of  $\sim 0.7$  cm month<sup>-1</sup> during the period of observation ( $\sim 2$  C-band LOS fringes).

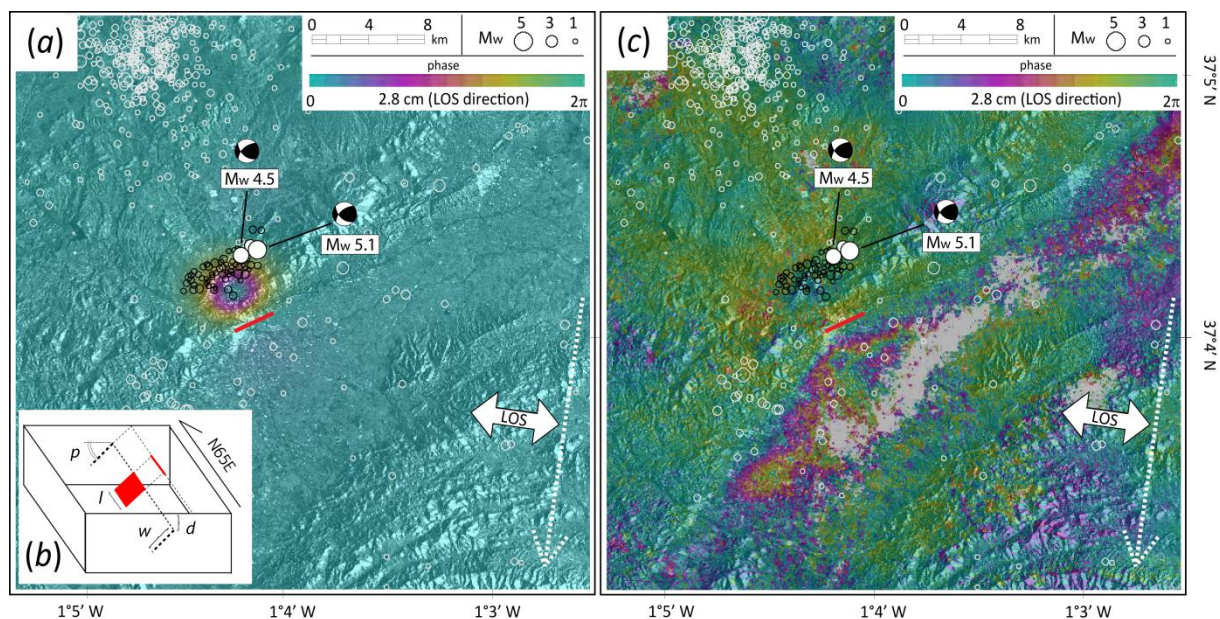


Figure 4.2 3. (a) surface displacement of the Lorca earthquake as inferred from the proposed elastic dislocation model (Table 2-1). Seismicity: same as in Figure 2. (b) illustration of the modeled fault plane geometry:  $l = 2.9$  km;  $w = 2.9$  km;  $d = 3.2$  km;  $p = 45^\circ$ . The red segment is the surface extension of the modeled seismogenic fault. (c) residuals between the observations and the elastic dislocation model. Seismicity: same as in Figure 2. The proposed model explains more than 90% of the displacement field NW of the AMF, but it cannot explain the large subsidence occurring in the Guadalentín basin. The red segment is the surface extension of the modeled seismogenic fault. Black circles represent the relocated aftershocks (after Lopez-Comino et al., 2012). DMS coordinates

Our second best model in terms of both fitting the data and agreement with preliminary focal plane solutions (by INGV, GFZ and USGS) and published relocated aftershocks at depth (figure 4.4 4 in Martínez-Díaz *et al.* 2012b) is consistent with slip on a blind thrust dipping to the SE. This result suggests that the Lorca earthquake might have ruptured a 3-km-long  $\times$  3-km-wide asperity belonging to a N230° E oriented fault centred at 4.2 km depth and dipping 50° to the SE (table 4.4 2). This

second model indicates that  $\sim 22$  cm coseismic slip partitioned into 21 cm reverse slip and 6 cm leftlateral slip (rake  $77^\circ$ ) can produce a surface displacement of  $3 \pm 0.5$  cm in the LOS direction (figure 4.4 4). The residual in figure 4.4 4 falls within the level of noise in the stacked interferogram (0.5 cm standard deviation). Therefore, this solution satisfactorily reproduces the set of observations and thus cannot be rejected *a priori*. Moreover, the Mw suggested by this 2nd model (Mw 5.12) is in good agreement with the seismic moment deduced from seismological observations. Frontera *et al.* (2012) measured  $5.5 \text{ mm} \pm 0.2 \text{ N}$  offset at the GPS station ‘Lorc’. We verify that both our models are consistent with the direction and the magnitude of GPS offset; model 1 predicts 1mm N offset and model 2 predicts 1.6 mm N offset at ‘Lorc’ station.

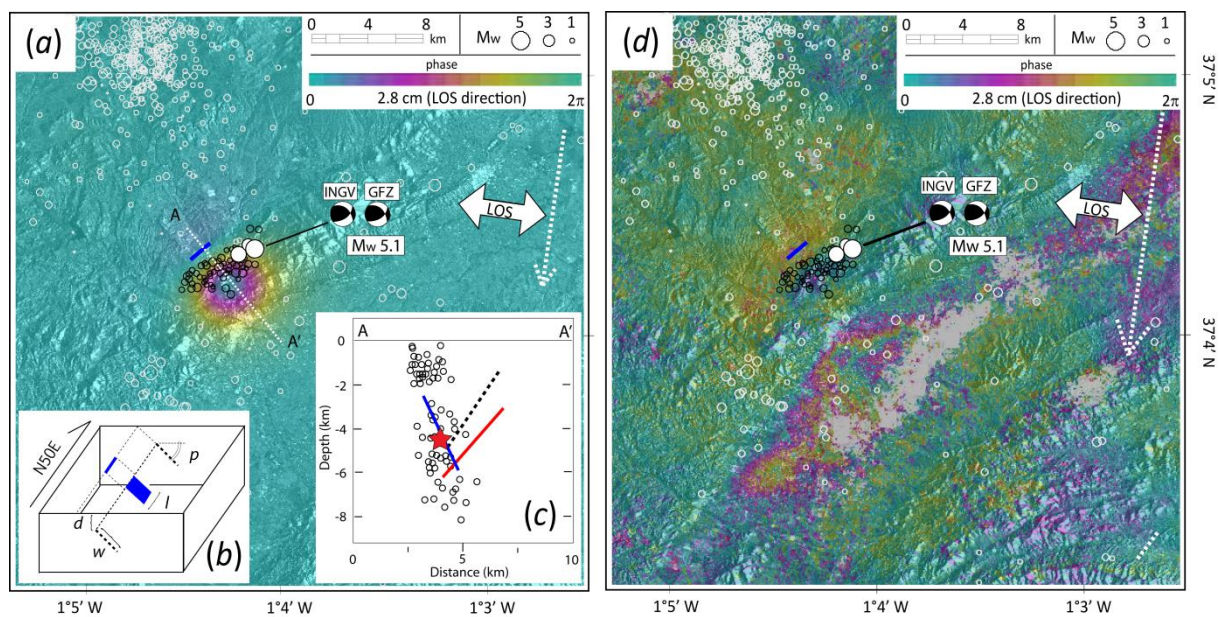


Figure 4. Left: (a) surface displacement of the Lorca earthquake as inferred from the second elastic dislocation model (Table 2-2). Seismicity: same as in Figure 2. (b) illustration of the modeled fault plane geometry:  $l = 3$  km;  $w = 3$  km;  $d = 2.8$  km;  $p = 50^\circ$ . The blue segment is the surface extension of the modeled seismogenic fault. (c) comparison between modeled fault planes at depth and relocated aftershocks on profile A-A' (after Martinez-Diaz *et al.*, 2012). Red: our model one; blue: our model two; dotted line: uniform slip model after Martinez-Diaz *et al.* (2012). (d) residuals between the observations and the elastic dislocation model 2. Seismicity: same as in Figure 2. The blue segment is the surface extension of the modeled seismogenic fault. DMS coordinates.

### Discussion and conclusions

Despite its low magnitude, the 11 May 2011, Mw 5.1, Lorca earthquake was shallow enough to produce a deformation field which was measurable with C-band ENVISAT InSAR. A simple elastic dislocation model was able to characterize the size, the depth and the amount of slip along the fault plane. The best-fitting model corresponded to a square fault segment of  $2.9 \text{ km} \times 2.9 \text{ km}$ . We found

that the centroid of the fault segment was located at a depth of 4.2 km. The slip was modelled as 22 cm of oblique–reverse slip. The moment magnitude predicted from the models proposed here was Mw 5.1. This value is consistent with the moment magnitude inferred from the seismological data. Nevertheless, we found that given the blind nature of the seismic rupture, the complex surface-displacement pattern (containing both seismic and non-seismic displacement), the different preliminary moment tensor solutions, the locations of aftershocks at depth and the level of noise in the interferogram stack, we were not able to discriminate certainly the orientation of the fault plane based on InSAR only. If we combine different sources of information such as rupture directivity, structural geology and InSAR (Vissers and Meijninger 2011, González *et al.* 2012, Lopez-Comino *et al.* 2012, Martínez-Díaz *et al.* 2012a, 2012b), our first model is consistent with a rupture on a segment of the AMF. If we combine different published information from relocation of aftershocks at depth, preliminary moment tensor solution (from INGV, GFZ and USGS) and our InSAR data, the best model is consistent with slip on a blind thrust dipping to the SE, suggesting that the Lorca earthquake might have ruptured a 3-km-long by 3-km-wide asperity belonging to a N230° E oriented fault centred at 4.2 km depth and dipping 50° to the SE. We conclude that ENVISAT extension-orbit data showed their ability to deliver coherent interferograms that can be used to study and to obtain a better understanding of shallow and moderate (Mw ~ 5) seismicity in Europe. Still, our analysis of the shallow Lorca earthquake has shown that the synergy of InSAR and seismology allows one to characterize the depth, the quantity of slip, the size and the focal mechanism of the earthquake source, but the nodal plane orientation is still a challenge; the main obstacles being the blind nature of the earthquake rupture, the phase noise and the presence of a long-term high-rate (~0.7 cm month<sup>-1</sup>) subsidence in the Guadalentin basin. In this case, one cannot rely on remotely-sensed data only but has to consider local structural geology (Martínez-Díaz *et al.* 2012a) fault directivity (Lopez-Comino *et al.* 2012) and damages analysis (Giner-Robles *et al.* 2012) to further constrain the fault geometry at depth.

Interferogram number	Time span (date)	Perpendicular baseline (m)	Temporal baseline (days)
1	27 Nov 2010–26 Apr 2011	203	150
2	27 Nov 2010–26 May 2011	–57	180
3	27 Nov 2010–25 Jun 2011	–267	210
4	26 Apr 2011–26 May 2011	146	30
5	26 Apr 2011–25 Jun 2011	63	60
6	26 May 2011–25 Jun 2011	209	30

Table 4.4 1. The calculated differential interferograms spanning from November 2010 to June 2011 with a maximum perpendicular baseline of 267 m.

Dip (°)	Length; width (km)	Depth of the fault top edge (km) <sup>1</sup>	East coordinate (km) North coordinate (km) <sup>2</sup>	Slip (mm) <sup>3</sup>
45	2.9; 2.9	3.2	614.65 ; 4172.67	210 R; 65 LL
50	3.0; 3.0	2.8	613.41; 4173.77	210 R; 60 LL

Table 4.4 2. Models parameters. The fault is assumed to be a rectangle buried in an elastic half-space, and the slip is assumed homogenous over the entire fault. (a) Vertical depth of the fault top edge; (b) East and North coordinates are in UTM zone 30 and refer to the middle point of the top edge of the fault; (c) R = reverse slip; LL = left-lateral strike slip.

#### 4.5. Article n°4

##### **Direct measurement of ocean waves velocity field from a single SPOT-5 dataset**

*Marcello de Michele a, Sébastien Leprince b, Jérôme Thiébot a, Daniel Raucoules a, Renaud Binet c*

A contribution from

a Bureau de Recherches Géologiques et Minières (BRGM), Service Risques Naturels, 3 Av. C. Guillemin, 45000, Orléans, France

b California Institute of Technology, Division of Geological and Planetary Sciences, Pasadena, CA 91125, USA

c Commissariat à l’Energie Atomique et aux Energies Alternatives Centre DAM/Ile de France, Bruyères le Châtel 91297 Arpajon Cedex France

We thank the Kalideos team (CNES) for providing the SPOT5 dataset. Discussions with Alain Giros improved this study. We are thankful to Nadia Khezami for her earlier inputs to this study. MdM, JT, DR thank BRGM Research Direction for supporting the study. SL was partly supported by the Keck Institute for Space Study and by the Gordon and Betty Moore Foundation.

##### 4.5.1 Abstract

We present a method based on space-borne optical imagery from the SPOT5 satellite to directly measure the phase velocity fields of ocean waves. The panchromatic and multispectral scenes acquired by SPOT5 the same day on the same area are not strictly superimposable due to the different locations of the CCDs (Charged Coupled Device) in the focal plane of the instrument. In this manuscript, we propose a method that exploits the temporal lag that exists between the panchromatic and multispectral scenes to measure the ocean wave velocity fields. We firstly discuss the principle and the methodology. Then, we apply it offshore La Reunion Island. Finally, we compare and discuss the results against a swell propagation model. Our method is proven reliable and can be immediately extended to other push-broom sensors.

## Introduction

Ocean waves represent an important oceanographic phenomenon for manifold reasons. For instance, they strongly influence the most superficial water layer where the exchanges and heat transfer between the ocean and the atmosphere take place. Moreover, the ocean swell highly affects coastal areas, being one of the principal agents responsible for coastal erosion. Furthermore, their propagation pattern being affected by shallow bathymetry, ocean wave velocity fields can provide invaluable information about the ocean floor topography at shallow depth. Traditional swell measurement methods typically employ sensors mounted on buoys or sensors installed at depth to determine ocean state characteristics. These methods are of great precision and allow one to measure the swell parameters on a point to point basis and are therefore well adapted to regions where the ocean swell is spatially uniform. However, in coastal areas the ocean wave field is not spatially uniform as it is modified on its arrival at shallow depth by near-shore processes that depend on local bathymetry (shoaling, refraction, breaking etc.). Therefore, it is of primary importance to measure the swell spatial variations. For instance, phenomena such as coastal erosion and marine flooding are highly dependent on the local wave characteristics. Since classical in situ instruments are often difficult to deploy in shallow water where waves break, wave models are often used to estimate the local sea state from the offshore wave buoys data. Space borne imagery has been demonstrated complementary to in-situ measurements in overcoming some of the aforementioned limitations and it typically renders the ocean swell using two frequency bands of the electromagnetic spectrum, the microwave and the visible bands (e.g. Larouche & Lavoie, 1996). The microwave imaging technique consists in an active hyper-frequency system such as the Synthetic Aperture Radar (SAR). The SAR backscattered signal on the ocean surface is dominantly governed by Bragg scattering (e.g. Chapron et al., 2005; Plant & Keller, 1990; Thompson et al., 1991) so that it is the small scale ocean roughness, essentially driven by the wind, that allows for imaging of the ocean swell by radar. A large number of studies have demonstrated that SAR imaging systems are able to correctly evaluate the swell wavelengths and directions even though a certain number of conditions have to be respected for a SAR to image the ocean swell (e.g. Ardhuin et al., 2004; Beal et al., 1983; Breivik et al., 1998; Collard et al., 2005; Dobson & Vachon, 1994). Concretely, most of the aforementioned methods are based on the evaluation of swell spectra retrieved from the SAR imaging systems, not from direct measurements of the swell velocity field. To overcome this limitation, Chapron et al. (2005, 2004) evaluated the Doppler shift of radar echoes occurring during the synthetic aperture as a direct measurement of ocean surface wave velocity (e.g. Johannessen et al., 2008). Since the Doppler shift is analysed on a sub-aperture base, Doppler velocities are obtained at spatial resolutions of 2 km for a narrow swath SAR, and this pioneering method does not yet yield spatially detailed information close to the coast. Higher spatial resolution systems or space-borne Along-Track Interferometry (ATI)

might overcome this SAR limitation. Techniques based on space-borne sensors operating in the visible range of the electromagnetic spectrum capture the specular reflection of visible sunlight on the multiple facets of the ocean swell. These techniques are limited by clouds, and to periods for which the sun, the sensor, and the ocean wave field are in a favourable alignment to allow for the swell image formation. For these reasons, optical techniques have encountered a limited development compared to SAR methods. Still, a large number of studies have demonstrated the potential operational use of optical imaging systems for studying the ocean swell spectra from high resolution SPOT images (e.g. Populus et al., 1991) or for direct measurement of advective surface velocities from medium resolution satellite sensors such as AVHRR, MODIS (e.g. Crocker et al., 2007; Emery et al., 1986) and Nimbus 7 (Garcia & Robinson, 1989). Moreover, a number of studies have demonstrated the potential of airborne infra-red remote sensing to evaluate swell spectra (e.g. Dugan et al., 1996; Gelpi et al., 2001) and surface currents using airborne visible image time series (e.g. Dugan & Piotrowski, 2003). Nonetheless, the direct measurement of ocean wave velocity fields from high resolution visible space-borne imagery is still a challenge. In this manuscript, we propose an innovative space-based method that jointly uses the panchromatic and multispectral instruments on-board the SPOT-5 satellite, respectively at 5 m and 10 m ground sampling distance (GSD), to directly measure the ocean surface velocity field at very high spatial resolution. Our method relies on two observations. First, owing to the SPOT-5 sensor's geometry, there exists a small temporal lag between “simultaneous” panchromatic and multispectral acquisitions. Because of this temporal lag, moving objects within the scene will therefore be imaged at different locations between panchromatic and multispectral images. Second, the relative displacement of objects between scenes can be measured with high accuracy and precision with well-established image cross-correlation techniques. We present the general concept of the method, test it, and discuss the results by comparing them with modelled ocean swell velocity offshore La Reunion Island (Indian Ocean). We conclude that our method is proven reliable and could be extended to most other space-borne optical sensors to increase temporal data sampling. Geometry of the SPOT-5 panchromatic and multispectral sensors Since 1986, SPOT satellites (SPOT 1–5) have been forming a constellation acquiring images of the Earth from a sun-synchronous near polar, 832 km altitude orbit with 26 days repeat cycle. SPOT orbits and station positioning are precisely determined by the Doppler Orbitography and Radiopositioning Integrated by Satellite (DORIS) instrument hosted by the payload. The DORIS integrated system allows for the precise computation of SPOT position and velocity every 30 s. In particular, SPOT-5, launched in 2002, is continuously controlled in yaw steering mode by a programmed control loop and a star tracking unit that computes absolute angles along the three attitude axis and provides high accuracy attitude measures to the ground (Riazanoff, 2002). Among other imaging sensors, SPOT-5 is equipped with High Resolution Geometry (HRG1-2) instruments

that acquire data in multispectral mode (XS1–2–3) at 10m spatial resolution and in panchromatic mode (HMA-B) at 5 m GSD respectively. The panchromatic and multispectral scenes acquired the same day on the same area and by the same instrument are not strictly superimposable due to the different locations of the CCDs in the focal plane of the instrument. In particular, an image line acquired at a given time by one of the HRG instruments is approximately  $9.24 \times 10^{-3}$  rad in front of the subsatellite point in panchromatic mode (HMA) and  $9.24 \times 10^{-3}$  rad behind the sub-satellite point in multispectral mode (HS) (Fig. 4.5 1). This configuration has been exploited to extract Digital Elevation Models (DEM) as it gives rise to a slight parallax view (e.g. Mai & Latry, 2009; Massonnet et al., 1997; Vadon, 2003).

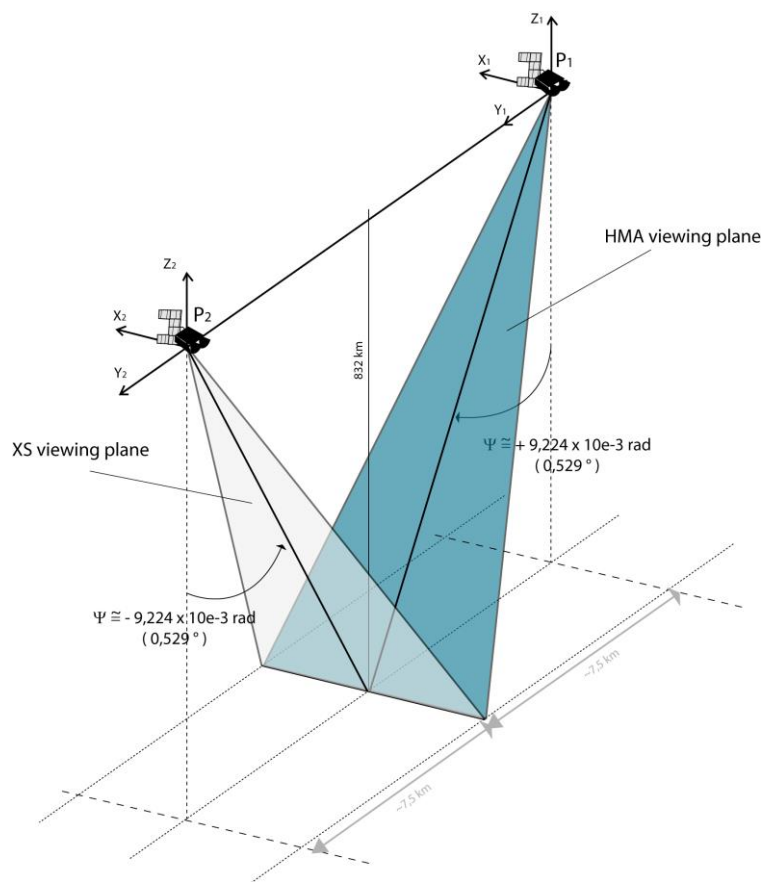


Figure 4.4 1. Acquisition geometry of SPOT5 HRG instrument (modified by the authors after Riazanoff, 2002 ). X, Y and Z represents the attitude state vectors stored in the ancillary data files; P1 and P2 indicate the position of the platform at  $T_0$  and  $T_0 + \Delta t$ , when acquiring the HMA and XS data respectively. In this case study,  $\Delta t = 2.04$  seconds.

Because the sensors are aimed at imaging exactly the same area on the ground, the panchromatic and multispectral scenes are therefore acquired with a temporal shift. For a given SPOT-5 dataset,



geometry, the glints stick to the wave slope as it moves. Therefore, by measuring the glint offsets (vector “ $d$ ”) and dividing it by image acquisition time lag  $\Delta t$ , we can measure the waves velocity. “ $S$ ” is the sunlight front,  $r_1$  and  $r_2$  are the specular reflections captured by the HMA and HS sensors at time 1 and 2 respectively. Specular reflections are symmetrical to the incident light with the respect to the local surface normal (corresponding to “ $z$ ” in this simplified case). “ $E$ ” is the Sun elevation angle (measured from the horizon) and “ $I$ ” is the viewing incidence with respect to the vertical “ $z$ ”. The condition to get proper surface illumination, is approximately  $60^\circ < E + I < 120^\circ$ . The reader should refer to Populus et al. (1991) for more details.

### Dataset

We use a panchromatic+multispectral SPOT-5 dataset acquired over La Reunion Island on February 6th, 2010 (Fig. 4.5 3). In particular, we use the HMA panchromatic band with spectral bandwidth centred at  $0.58 \mu\text{m}$ , and analyse it against the XS1 multispectral band (green), which has its spectral bandwidth centred at  $0.55 \mu\text{m}$ . We selected the XS1 because it is the one that closely matches the response of the panchromatic sensor, which can be critical to obtain good image cross-correlation (e.g., Necsoiu et al., 2009). The SPOT-5 orthorectified dataset has been made available in the frame of the Kalideos Project led by the French Space Agency (Centre Nationale d'Etudes Spatiales — CNES). The forward (HRG) and backward (HS) dataset were precisely orthorectified using a rigorous sensor model and a Digital Elevation Model (DEM) by CNES. The HRG and HS dataset are co-registered inland to subpixel accuracy. We subsample the HMA band spatial resolution (5 m) to match the HS spatial resolution (10 m). Then, we use the COSI-Corr correlation to derive the relative pixel offset field that is expected from the ocean wave motion.

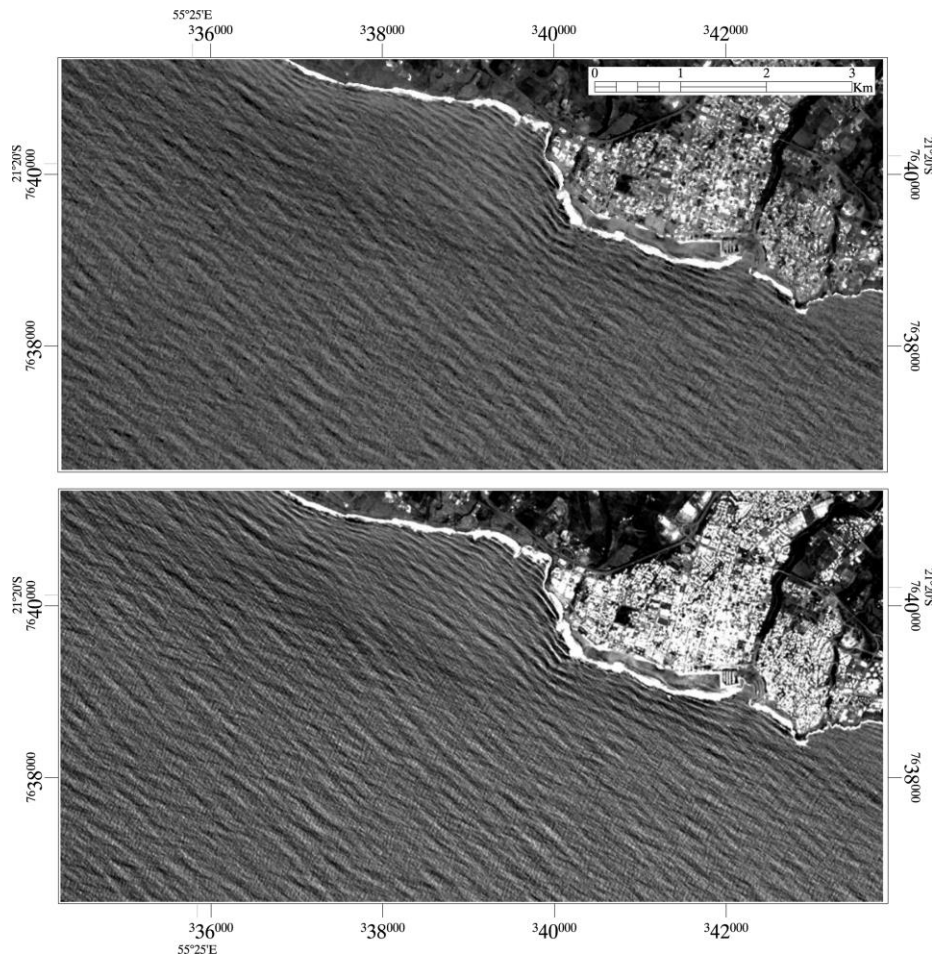


Figure 4.4 3. SPOT5 HRG dataset, south of La Reunion Island. Top: the HMA image (subsamped to the 10 m resolution XS image). Bottom: the XS image. We can observe a signal due to the SW/NE swell as well as a higher frequency wind waves directing SE-NW.

#### Optical image correlation

Image correlation techniques using sliding windows have already been successfully applied to both satellite and airborne photographs to monitor Earth surface displacements. In particular, on seismogenic faults (e.g. Binet & Bollinger, 2005; de Michele et al., 2008; Dominguez et al., 2003; Klinger et al., 2006; Michel & Avouac, 2002, 2006; Van Puymbroeck et al., 2000), on volcano deformation (de Michele & Briole, 2007; Tobita et al., 2001), on gravitational movements assessment (e.g. Berthier et al., 2005; Crippen, 1992; Debella-Gilo & Kaab 2011; Delacourt et al., 2004; Scherler et al., 2008), on sand dunes migration (Necsoiu et al., 2009). This technique analyses the phase difference of the local instantaneous frequency of the images to determine local subpixel offset vectors to a nominal precision better than 1/10 of the pixel size. In this study, we propose to enlarge the spectrum of applications of this method by applying it for the first time to a SPOT5 dataset to measure directly the phase velocity field of ocean waves. The reader should refer to the work of Van Puymbroeck et al. (2000) and to the work of Leprince et al. (2007) for details on the principles of the

correlation. In this study, we use a 64×64 sliding window with a sampling step of 32 pixels (320 m). We only retain reliable offset measurements, i.e., with a confidence higher than 0.97 as defined by the COSI-Corr correlation signal-to-noise ratio.

#### Detection limits

Since a parallax view leads to a stereoscopically-driven pixel offsets on regions with varying topography, the parallax between panchromatic and multi-spectral acquisitions is the main potential source of bias to the velocity measurements. The base to height ratio (B/H) controls the sensitivity of a particular acquisition system to the topography, where the base B is the linear distance between the scenes acquisition points and H is the platform altitude. The system configuration presented here yields a B/H equal to 0.018. Hence, the potential bias  $d$ , induced by ocean surface topography  $h$  on the wave offsets is:

$$d = h * B/H$$

This means that a potential 10 m high ocean wave (or 10 m error on the DEM) would produce an apparent pixel offset of 0.18 m on a SPOT-5 dataset, which would lead to an apparent wave velocity bias of 0.08 m/s. This is small in comparison to typical wave velocity values (~10 m/s). Moreover, as the epipolar direction may be approximated by the platform velocity direction (along-track stereo), the stereoscopic parallax would induce an error only in the North/South velocity estimates. In summary, we can conclude that the sea surface elevation induced by the waves negligibly influences the accuracy of the ocean wave velocity measurements. Ocean pixels are correlated by considering that land features are fixed reference points. We verify that the dataset are co-registered to subpixel precision inland by looking at the COSI-Corr correlation score along the coast. Inland, we found a mean of 0.04 pixels offset with a standard deviation of 0.75 pixels, equivalent to an intrinsic precision on the velocity measures of ±3.6 m/s. SPOT5 is a pushbroom system for which a linear CCD array integrates the sunlight coming from the ground, the line-by-line sampling being performed by the motion of the platform itself perpendicularly to the CCD array. The line-by line sampling-time is adjusted such that the spatial sampling step is identical in both rows and columns directions. As columns sampling-step is fixed as the distance between two elementary detectors of the CCD projected to the ground, the line-by-line sampling-time to achieve 5 m resolution is nominally 0.75 ms (Latry et al., 2001). Concerning the phenomenon that we aim to measure in this study, we can reasonably consider 0.75 ms per line as an instantaneous sampling which does not significantly influence the wave velocity measurements. Nevertheless, as it takes ~9 s to collect the whole 12,000 line HMA dataset, one should consider the aforementioned characteristic when measuring the

velocity field of very large scale and fast moving phenomena, such as tsunamis for instance, using the method proposed here.

### Modelling with SWAN

We compare our SPOT-5 velocity field with the velocity field derived with the SWAN wave propagation model. SWAN solves the transport equation for wave energy density (Booij et al., 1999; Ris et al., 1999) and is commonly used to obtain realistic estimates of wave parameters in coastal areas. In our configuration, SWAN simulates the following physical phenomena: wave propagation, shoaling, refraction due to depth, wind effects, and wave energy dissipation by bottom friction and by depth-induced breaking. Our SWAN configuration is nested within the global wave model NOAA WaveWatchIII (Tolman, 1991, 2009). We have used a standard parameterization which has been validated at La Reunion Island site using data collected at two omnidirectional wavebuoys. In this study, for the comparison with the SPOT-5 data, the results are extracted over a 1×1 km grid centred on the study area.

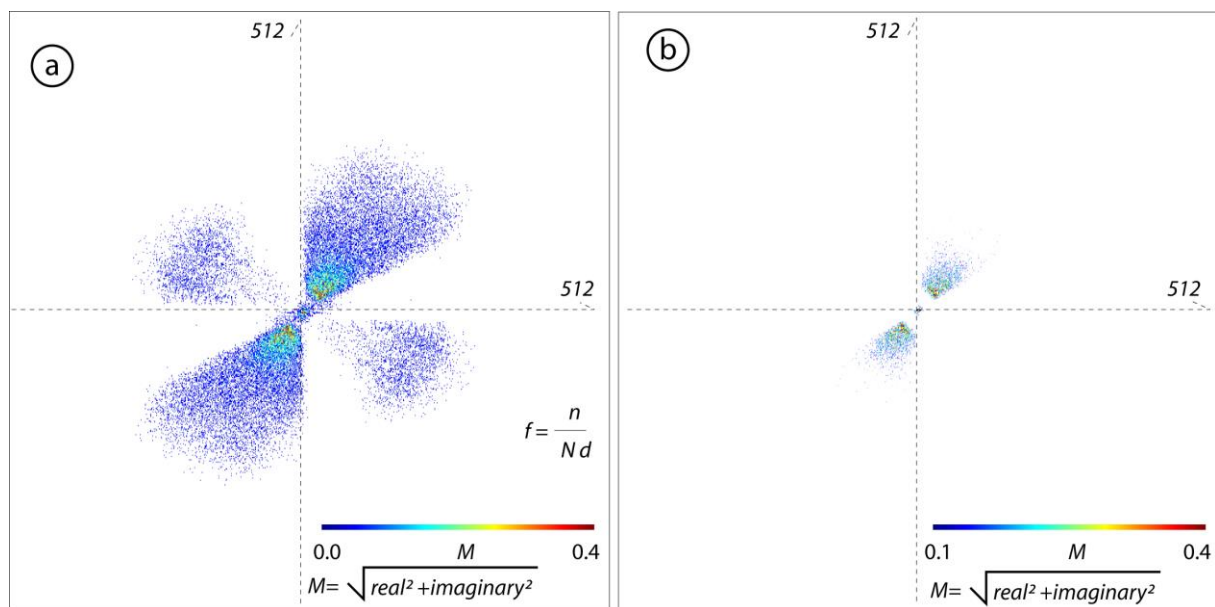


Figure 4.4 4. FFT spectrum calculated on a 512x512 pixels window over the ocean Image. A: FFT spectrum before the filtering. We can clearly see two preferential directions related to the swell (SW-NE) and the wind waves (SE-NW). B: FFT spectrum after filtering. We set the filter in such a way that FFT magnitudes less than 0.1 are discarded and only directions in the 1<sup>st</sup> and 3<sup>rd</sup> quadrant are retained for further processing.

### Swell and wind-generated waves: spectral analysis

The ocean surface wave field can be seen as the sum of several harmonic waves. On the SPOT-5 images studied here, we visually distinguish two components of the ocean wave field. On the one

hand, we can observe the South-West swell. On the other hand, we can observe a higher frequency wind waves signal directing SE–NW (Fig. 4.5 3). Our cross-correlation method measures the amplitudes and the directions of the pixel offset vectors resulting from the superposition of these two wave fronts, as they move simultaneously in different directions. These two components of the wave field are clearly visible in the image spectrum (Fig. 4.5 4a) calculated over the ocean only. The modelling with SWAN is based on the distribution of wave energy, which depends on the wave heights, as a function of frequency and direction. Therefore, the spectral discretization in SWAN is different than the one used for retrieving the waves velocity field from SPOT-5. The SWAN wave spectrum highlights the presence of two types of waves: the swell waves and the wind waves, the swell waves being the most energetic. We have restricted the SPOT-5/ SWAN data comparison to one type of wave only, the swell. In this case study, as the swell and the wind waves present very distinct propagation directions, we can separate them by applying a directional filter to each of the SPOT 5 images to only retain the information from the swell (Fig. 4.5 4b). The filter masks out the values aligned on the frequency axes  $-25/+155$  with a fan of  $40^\circ$ . We also decide to only work with high energy values in the FFT spectrum of Fig. 4.5 4a. Practically we filter out all the values within the quadrants 2 and 4 of the FFT spectrum and work with FFT magnitudes higher than 0.1 (i.e., a frequency mask of 0.57 in COSI-Corr). Concerning the results of SWAN, as the swell is more energetic than the wind waves, we use peak parameters (i.e. the sea state parameters calculated where the spectral energy is maximum) to focus on the swell characteristics for the comparison.

## Results

Using subpixel cross-correlation between two SPOT images, we have derived both the velocity field due to the ocean swell alone, and the total velocity field comprised of both swell and wind components. The results in Fig. 4.5 5 show that the swell velocity retrieved by SPOT-5 reaches up to 12.9 m/s (2.63 maximum pixels offset) and presents a SW/NE direction. We observe that the results obtained by filtering the SPOT-5 prior to correlation to retain only the swell information closely match the characteristics of the swell calculated with SWAN. We compute the measurements bias as the norm of the mean difference between SPOT-5 swell velocity vectors and SWAN-modelled swell velocity vectors.

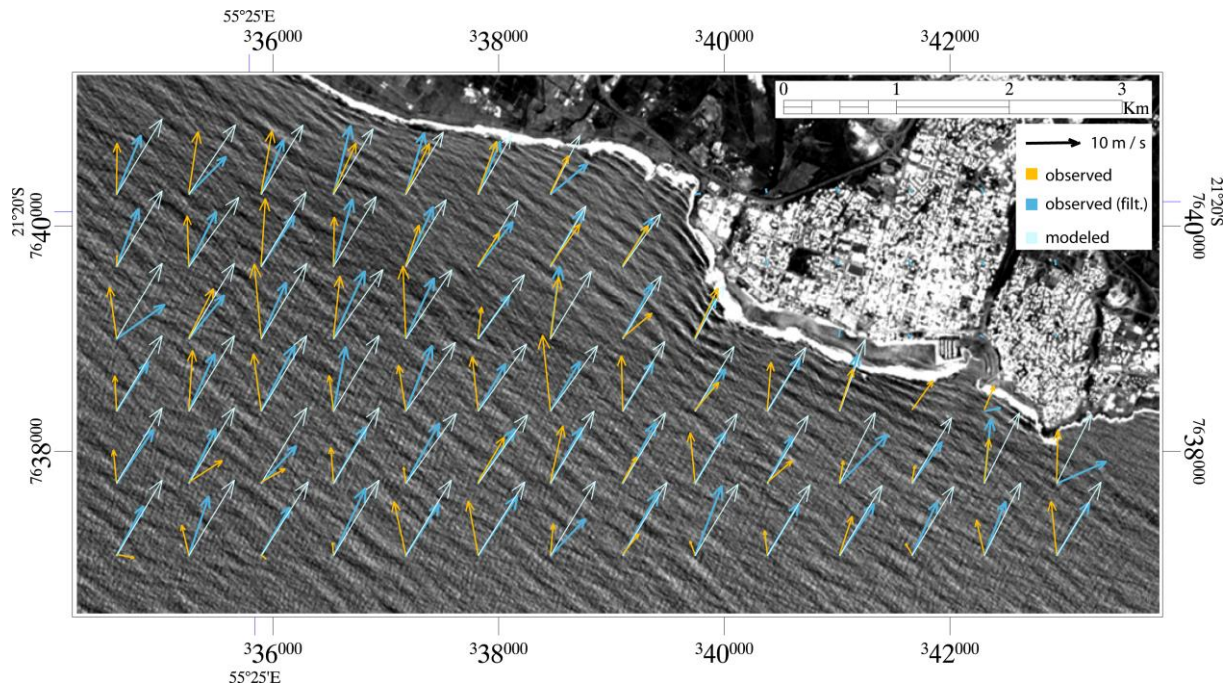


Figure 4.4 5. Wave velocity field retrieved from the SPOT-5 dataset (both filtered and not filtered) compared to SWAN modeled results. Orange arrows: velocity vectors obtained from COSI-Corr analysis on non-filtered SPOT-5 data. They represent the velocity field that result from both the swell and the wind waves motion. Dark blue arrows: velocity vectors obtained from COSI-Corr analysis on filtered SPOT-5 data. These vectors reasonably correspond to swell velocity field. Light blue arrows: velocity vectors obtained from SWAN swell analysis.

Moreover, we assessed the norm of the standard deviation of the X and Y components of the difference vectors. We find a bias of 2.3 m/s (0.4 pixels offset) and a precision of 1.6 m/s (0.3 pixels offset), which correspond to a 25% bias and 17% of misfit on the SPOT-5 velocity measurements. Considering the direction, we report 5° of standard deviation between SWAN and SPOT results. This value falls within the commonly expected wave directional spreading which is usually between 10° and 30°. Therefore, we can say that this first order comparison yields promising results. The reader should note that there are mainly two caveats to this quantitative comparison. First, the model does not represent the ground truth but the physics of wave propagation based on independently measured inputs. Second, we compare instantaneous measurements vectors from SPOT-5 to time-averaged vectors from SWAN.

#### Conclusions and perspectives

In this manuscript, we presented the potential of SPOT imagery for the direct measurement of ocean wave velocity fields. We compared the SPOT-5 results with SWAN modelling, and both methods indicate that the sea state comprises two types of wave regimes: the swell and the wind sea.

Focussing on the swell only, the comparison indicates that our methodology is promising. Nevertheless, there are few caveats to the data comparison. Indeed, we have distinguished wind waves from swell waves using a directional criterion but in situations where wind waves and swell waves have similar directions, one should consider alternative filtering methods or account for both phenomena into the modelling. Additional validation is needed in particular in areas where ground instrumentation is dense and data sampling is frequent. Our methodology is complementary to other space-borne techniques such as the SAR Doppler velocity and could be of great interest particularly to monitor coastal processes. Our approach can directly be extended to archived dataset (e.g. from the whole SPOT archive) to study past phenomena related to ocean circulation. This method could be potentially applied to measure the dynamics of a variety of fast moving phenomena such as ocean eddies, river flows, lava flows, volcanic plumes, tornadoes and hurricanes, icebergs, and glacier flow. The major limitation of this method is related to the image acquisition when the cloud coverage is high. Nevertheless, the revisit time can be improved as the methodology presented here can immediately be extended to the many space-borne pushbroom platforms equipped with along-track stereoscopic or multispectral sensing capabilities such as ASTER (Kääb & Prowse, 2011; Matthews, 2005; Matthews & Awaji, 2010), PRISM, SPOT-HRS, Quickbird, IKONOS, or Worldview instruments. We encourage detailed investigations on the potential use of those instruments for velocity field measurements and recommend this data acquisition configuration for future missions.

#### 4.5. Article n°5

##### **Water depth inversion from a single SPOT-5 dataset**

*Adrien Poupardin, Deborah Idier, Marcello de Michele, Daniel Raucoules*

*The authors work for the French Geological Survey (BRGM)*

Funding from the ANR Carnot institution, BRGM, and PNTS is acknowledged. The authors are grateful to the data providers: the Kalideos team (CNES) for the SPOT-5 dataset, SHOM and IGN for the bathymetric data (Litto3D® and multi-beam echo-sounder). The authors would like also to thank R. Pedreros for his contribution, as well as the reviewers for their comments.

##### Abstract

Knowing bathymetry at intermediate depth, over large areas, and at a reasonable cost is a key issue. Space-borne remote sensing techniques must play an essential role in retrieving such bathymetry. In this manuscript, a method is proposed that aims to address this issue without any in-situ

measurements by exploiting the characteristics of the SPOT-5 satellite dataset. The proposed method is designed to provide bathymetry from two optical SPOT-5 satellite images separated by a time-lag ***DT*** of **2.04 s**. It relies on estimation of several clouds of wave celerity and wavelength pairs using wavelet and cross-correlation techniques and on the linear wave dispersion relation. This method has been applied to two SPOT-5 images on a test site characterized by complex bathymetry (Saint-Pierre, La Réunion Island). Comparison of the retrieved bathymetry with *in-situ* bathymetric measurements reveals good morphological agreement. The mean relative error is less than **30 %** in the **3 – 80 m** water depth range. The methodological choices made during method development are discussed based on additional computations, and guidelines for using the proposed method on other images at other sites are provided

## Introduction

Today, knowledge of near-shore bathymetry is essential for multiple applications. For example, bathymetry provide essential data for the study of submarine morphodynamics. These data are vital for planning sustainable coastal development and conservation of submarines ecosystems. Moreover, they represent a crucial input for near-shore navigation and submarine resources exploration.

The reasons why space-borne remote-sensing techniques must play an essential role in retrieving near-shore bathymetry are threefold. First, space-borne imagery makes it possible to access remote areas with wide spatial coverage at high spatial resolution. Second, because space-borne imagery is acquired on a regular basis, a historical data archive is accessible for most sensors, which enables scientists to access information from the past. Third, the cost of the data is relatively affordable compared to airborne or ground missions.

A number of method have proven reliable in retrieving near-shore bathymetry from space-borne remote-sensing imagery. However, each of these presents substantial limitations with respect to ground-based (or airborne) methods, either because wave celerity  $c$  cannot be measured directly, or because ground calibration measurements are needed. Therefore, previous pioneering techniques in this field made use of either a priori information on wave characteristics or ground measurements to create a reliable near-shore bathymetric reconstruction from space.

Among existing techniques, one prominent approach is the use of multispectral satellite imagery, e.g., [Su et al., 2013] and [Capo et al., 2013]. This method makes it possible to measure bathymetry by assuming the optical depth properties of the water column in shallow waters. This technique has proven reliable for retrieving shallow bathymetry, until 20 m approximatively [Su et al., 2013], when waters are turbidity- free. Even for moderately turbid waters, the method may be used but the bathymetry may be only estimated until 4m in the case of [Capo et al., 2013]. The main drawback of

this method is the need to measure a calibration factor on the ground, which limits this technique to accessible areas. Other techniques to estimate bathymetry from optical, e.g., Leu and Chang, (2005) and Splinter and Holman (2009), or radar, e.g., Pleskachevsky and Lehner (2011) and Boccia et al., (2015), air-borne or space-borne imagery make use of wave characteristics. Most of these are based on a dispersion relation, which considers linear wave theory and is particularly well adapted to determine bathymetry at intermediate depths (i.e.,  $\lambda/20 < h < \lambda/2$ ):

$$h = \lambda/2\pi \cdot \tanh^{-1} \left( \frac{2\pi c^2}{g\lambda} \right) \quad (4.5 \ 1)$$

where  $h$  is the water depth,  $c$  the wave celerity and  $\lambda$  the wavelength. Here the dispersion relation is written for the case where the currents are equal to zero. Although  $\lambda$  can often be directly measured from the space-borne data themselves, these methods need either to make use of an *a priori* estimate of  $c$  (or the wave period  $T$ ) from a model or to obtain a ground-level measurement of  $c$  (or  $T$ ) from buoys, a limitation which results in punctual or sparse availability of measurements. Indeed, compared with ground-based or airborne-based methods like those described in Holman et al., 2013 and Plant et al., 2008, one key difference is that such airborne and satellite datasets (Leu and Chang, 2005, Splinter and Holman, 2009, Pleskachevsky and Lehner, 2011 and Boccia et al., 2015) are characterized by single images (i.e., no temporal description over a wave period). As a first pragmatic approach, the wave period is often assumed to be uniform. In the case where no wave period data are available, a constant wave period may be used by considering the offshore wave period computed from the deep water relation between wave period and wavelength Dalrymple et al., 1998. It is worthwhile to note that the method of Splinter and Holman, 2009 which is independent of the wave period, provide good bathymetric estimations. Their method exploits spatial changes in wave direction  $\theta$  to improve the bathymetry estimation and notably in considering the bathymetry gradients without any celerity information. It represents a good improvement to estimate the bathymetry from a single snapshot but it is not well adapted to more complex configurations. In contrast, the method described in this paper aims at considering the influence of the wave period which may be useful to study a complex sea characterized by several waves superimposing each other. Hereafter, for sake of clarity, this method will be called the CWB method for Correlation, Wavelets and Bathymetry. A pioneering method to retrieve bathymetry from satellite stereo image pairs for retrieving both wavelengths and wave celerities has already been described by Abileah, 2011. The CWB method differs from it because it determines depth by finding the best fit of the gravity dispersion equation to the measured power spectrum in the same manner as in Piotrowski and Dugan, 2002. Furthermore, the method proposed in Abileah, 2011 has been applied to

WorldView-2 and IKONOS satellite stereo image pairs characterized by time lags of 10 and 13 s (see, e.g., Abileah, 2013 for an application with WorldView-2). Such a time lag is quite close to the wave period (which generally ranges from a few seconds to 18 s for very long swells). Depending on the environment, this might lead to ambiguity in wave celerity or frequency detection. Furthermore, in the case of complex seas, it may be difficult to distinguish the different superimposed waves.

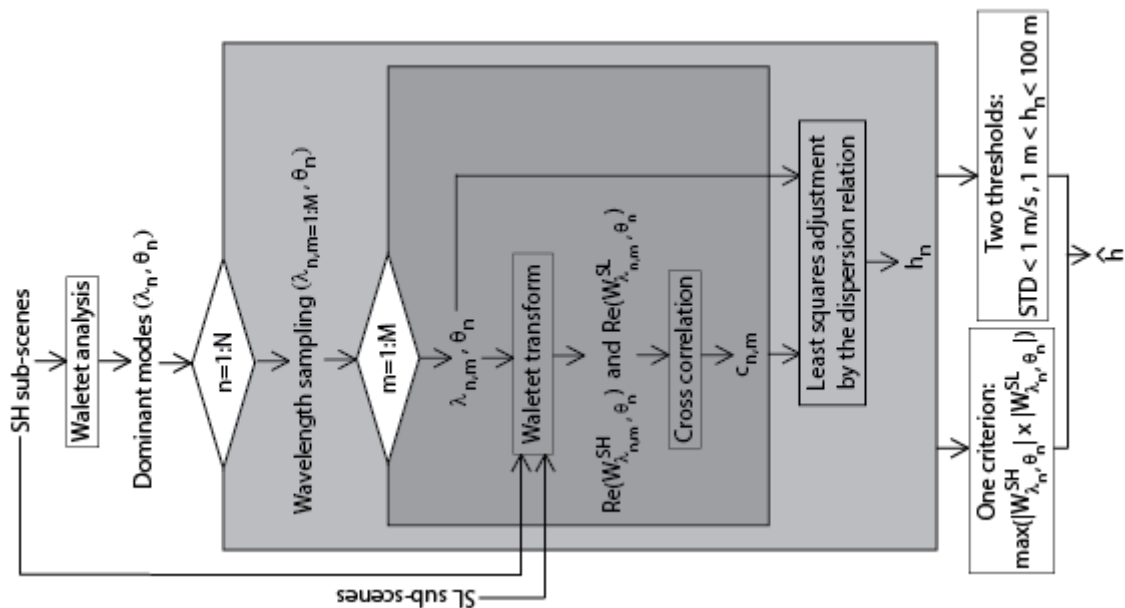


Fig. 4.5 1. Flowchart of the CWB methodology for retrieving bathymetry from two satellite images (**SH** for higher-resolution image and **SL** for lower-resolution image).

The CWB method uses the SPOT-5 HRV (High Resolution Visible) sensor which provides panchromatic and multispectral images acquired with a time lag of  $DT = 2.04 \text{ s}$  more adapted to follow the wave in his displacement. The main objective of this paper is to investigate whether by using the peculiar characteristics of the SPOT-5 dataset, it is possible to retrieve bathymetry from space with reasonable accuracy and precision without using any *in-situ* measurements or assumptions about the homogeneity of wave characteristics. To tackle the issue of estimating bathymetry using two images only, a method based on cross-correlation and wavelet analysis is proposed that exploits the spatial and temporal characteristics of the SPOT-5-like dataset to extract bathymetry. The proposed method combines the space-borne direct  $c$  measurement method presented in de Michele et al., 2013 and with an original wavelet-based adaptive  $\lambda$  estimate Poupardin et al., 2014 to retrieve a spatially dense series (clouds) of  $(\lambda, c)$  couples that are then used to estimate water depth using dispersion relation (4.5 1). A number of methods exist to derive the

wavelength  $\lambda$  from both optical and radar space-borne imagery. To measure  $\lambda$ , a dataset is needed with fine enough spatial resolution to isolate the shortest wavelengths. One of the first developments in measuring  $\lambda$  was proposed by Populus et al., 1991, who used a two-dimensional discrete Fourier transform applied to SPOT data at a spatial resolution of 10 m. In their study, Populus et al., 1991 could distinguish between swells and wind-generated waves, which are generated locally and therefore, have a shorter wavelength than swells. However, this method fails to determine wavelengths and directions correctly near the coast because waves evolve rapidly.

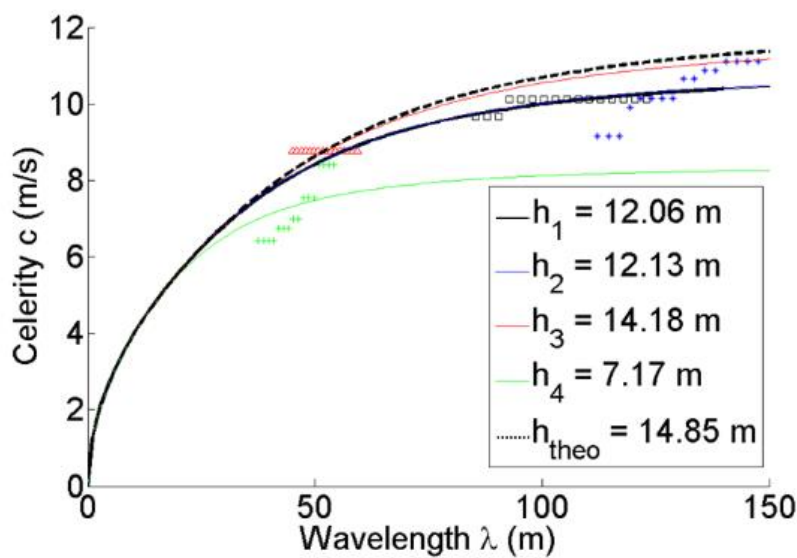


Fig. 4.5.2. Point clouds and nonlinear curve fitting corresponding to the  $n$  modes ( $n = 1$  (black),  $n = 2$  (blue),  $n = 3$  (red),  $n = 4$  (green)) at the P1 location (white cross on Fig. 3b). The selected  $\hat{h}$  is indicated with a thicker line (here, it is  $h_1$ ). The theoretical curve obtained using the in-situ bathymetry is shown by a dotted line.

To solve this problem, several authors have developed two-dimensional continuous wavelet analyses of sea state (Feng et al., 2011; Wu et al., 2011). These methods, which are based on ground photos, show good accuracy in characterizing waves, even in coastal areas. Chuang et al., 2008 tested a method on a synthetic wave-field dataset under various wave conditions and sea-bed slopes. They showed that two-dimensional continuous wavelets are well adapted to characterizing non-stationary and inhomogeneous wave fields. In particular, the method of [17] shows good precision in detecting wave refraction and reflection, taking shoaling effects into consideration, and determining wave spectra at any location in the coastal area. Wavelet function parameters were also discussed by [18],

who used a set of X-band Synthetic Aperture Radar (SAR) data as well as panchromatic QuickBird data to extract wave characteristics. Their method showed good results when retrieving ocean wave inhomogeneity and near-shore refraction and for describing local wave information at several locations on the scene, particularly near-shore. In Gorman and Hicks 2005, aerial laser scanning (ALS) measurements were used along with a continuous wavelet method to analyze the sea state in the spatial domain. Gorman and Hicks (2005) considered wave fields as greatly inhomogeneous and found that the Fourier transform method was not sufficient to retrieve wave characteristics at precise locations.

The variables  $c$  or  $f$  must be determined to estimate the water depth  $h$  from the dispersion relation (4.5 1), with  $f$  related to  $c$  by  $f = 2\pi c/\lambda$ . The literature contains many methods to measure  $c$  or the wave frequency  $f$  based on optical images. Apart for the study by Abileah, 2011, 2013 and de Michele et al., 2013, none of them makes use of space-borne imagery. As an example, the coastal observation techniques described in Holman et al., 2013, Plant et al., 2008, and Hampson et al., 2008, used well-resolved airborne or ground-based multi-temporal imagery to obtain the wave frequency  $f$  directly. In Holman et al., 2013, images were collected at an acquisition frequency of 2 Hz during 1024 s, which is not yet possible from a space-borne platform. Even with these ground-based experimental configurations, the wavelength  $\lambda$  must be deduced using dedicated techniques. For instance, Hampson et al., 2008 and Aarnes and Krogstad, 2001 developed the wavelet directional method (WDM) to determine the wavelength  $\lambda$  from the phase differences among spectral wavelet transforms of several couples of points in the spatial domain. In this method, the wavelets were applied to a water-surface elevation time series (estimated using ground equipment). In a similar manner, Holman et al., 2013 performed a temporal Fourier transforms on several points in the spatial domain before computing the cross-spectral matrix, providing estimates of the dominant eigenvectors and their associated wavelengths  $\lambda$ . Note that in the studies described by Holman et al., 2013 and Plant et al., 2008, a cross-correlation is realized to find the time delay  $DT$  which maximizes the correlation for a given frequency  $f$  whereas in the CWB method a cross-correlation is realized to find the wave displacement which maximizes the correlation for a given wavelength  $\lambda$ . In this last case, using two images separated by a small temporal lag  $DT$ , it is preferable to work with  $(c, \lambda)$  couples rather than  $(f, \lambda)$  couples which are more adapted to time series.

Some methods to resolve  $f$  as well as  $\lambda$  are particularly suited for airborne datasets Piotrowski and Dugan, 2002. In the experiment described in Piotrowski and Dugan, 2002, frames were collected at a frequency of 2 Hz during 480 s and a spatial resolution of 2 m for a spatial domain of 2 km  $\times$  2 km. With this optimal configuration, high spatial- and high temporal-resolutions  $f/\lambda$  spectra can be computed, yielding  $h$  with high precision. In their method, Piotrowski and Dugan, 2002 used the fact that the largest waves are more strongly impacted by the sea bottom. Then they considered a

wavelength range in the dominant wave direction (i.e., for the long waves impacted by the bottom) and the corresponding frequency range which maximized the spectral energy. Then they chose the  $h$  value that minimized the sum of squares of the distances between the point cloud found determined by the  $f/\lambda$  spectrum and the characteristic dispersion curve given by (1).

Ground-based and airborne observation techniques are well adapted to extract wave characteristics and bathymetry at high spatial resolution on well-defined local areas only. Today, because of cost or because of inaccessibility of the study area, they cannot be used routinely to cover very large surfaces. Moreover, this approach cannot be used to retrieve past bathymetry. Furthermore, ground-based image analysis methods cannot cover a large spatial extent. These limitations were the motivation for developing the space-borne method proposed here.

This paper proposes a methodology based on publicly available (commercial or not) space-borne optical imagery to determine  $h$ , which requires only one pair of images characterized by a short enough time lag.

This work is structured as follows. Section II describes the proposed method. Section III presents the application of the method to the selected SPOT-5 dataset to provide bathymetric estimates, which are compared with *in-situ* measurements. In Section IV, the results and method are discussed, as well as the applicability of the CWB method to other satellite datasets. Finally, conclusions are drawn (Section V).

### The CWB Method

In the procedure for estimating bathymetry from a single SPOT-5 dataset, the two main original ideas of the proposed method are: (1) to use wavelet analysis and cross-correlation techniques to estimate the wavelengths  $\lambda$  and the celerities  $c$ ; (2) to consider several clouds of  $(\lambda, c)$  couples to estimate bathymetry. Some of the underlying ideas have already been developed and used within ground-based or airborne approaches. However, the characteristics of space-borne images (only two images for the temporal dimension, at pluri-metric spatial resolution) imply specific issues compared to ground-based or airborne methods, so that the present method is original when applied to satellite-based bathymetric estimation. The methodology is illustrated in Fig. 4.5 1, and details are given in subsections A, B, and C. In the general case, the input data consist of two images, possibly with different spatial resolutions (this is the case, for instance, for SPOT-5 panchromatic and multispectral images). In the following paragraphs, the term *high-resolution scene (SH)* is used to refer to the SPOT-5 image with higher spatial resolution (i.e., the panchromatic image), whereas the term *low-resolution scene (SL)* is used to refer to the lower-resolution SPOT-5 image (i.e., the multispectral image). The corresponding spatial resolutions are designated by  $DX_{SH}$  and  $DX_{SL}$ . The principle of the CWB method is, for every subscene of the image where the  $(\lambda, c)$  are estimated, to

identify several waves (called dominant waves), to estimate several  $(\lambda, c)$  pairs (called a cloud) for each dominant wave, to use the obtained cloud to estimate one water depth per dominant wave, and then to select the “best”  $\hat{h}$  water depth among the various estimated depths. This principle is illustrated in Fig. 4.5 2 for one point P1 in the spatial domain (indicated by a white cross in Fig. 4.5 3b). In this example, four dominant waves were detected, providing four  $(\lambda, c)$  cloud pairs and therefore four estimates of water depth. The thick line indicates the selected  $\hat{h}$  value. Table 4.5 1 presents the parameters of the method, and its application is described below.

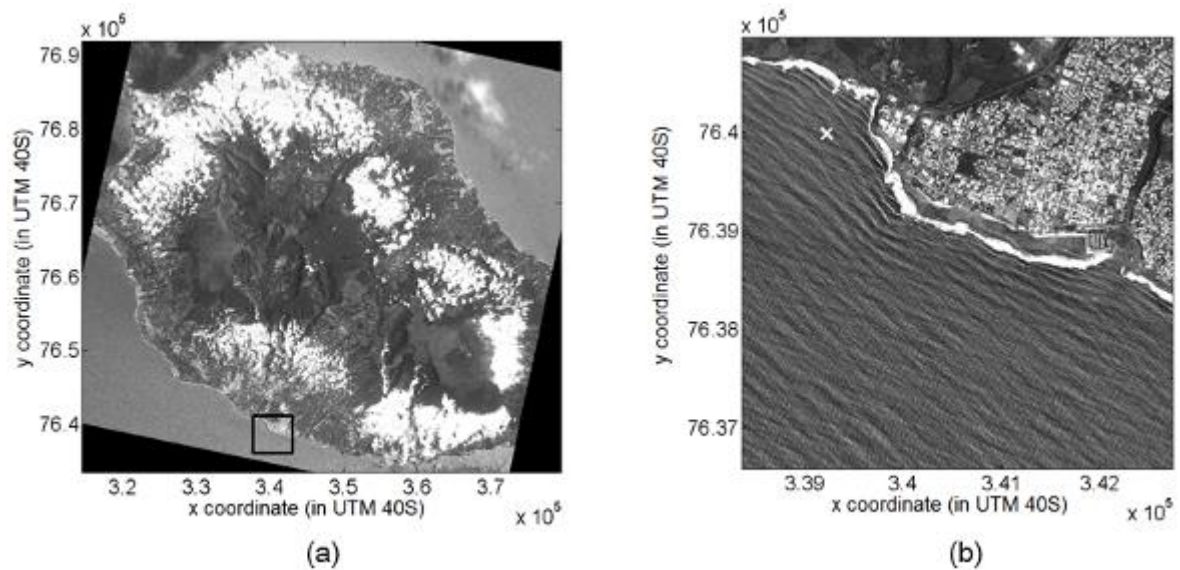


Fig..4.5 3. SPOT-5 panchromatic scene: (a) La Réunion Island; (b) Area of Saint-Pierre.

### Wavelet analysis of the higher-resolution scene *SH*

A wavelet analysis of the higher-resolution scene *SH* was carried out to obtain wavelengths with higher precision than those from a classical Fourier transform method. Indeed, the wavelengths vary rapidly on distances which are close to the wavelengths itself. The wavelet analysis is well adapted in this case because it may be computed at each pixel, providing a precise value of wavelength on these pixels. Furthermore, the Fourier analysis considers all the waves and noise included in the entire work subscene. In the case of Boccia et al., 2015 a smoothing of the wave spectrum was performed to keep only the swell. On contrary, the wavelet analysis eliminates a part of the noise and of the waves which are not centred on the work subscene leading to a higher spectrum quality without using any filters as shown in Wu et al., 2011 where an example of the comparison between the two analyses is given.

The wavelets used to characterize the image may be scaled, shifted, and rotated, which makes it

possible to detect all the waves at a particular location even if they are superimposed on each other. In the study of sea-surface waves, the most common and useful wavelets used in the literature are the Morlet wavelets (Feng et al., 2011, Chang et al., 2008, Wu et al., 2011, Gorman and Hicks, 2005). Therefore, the Morlet wavelet was selected for use in the proposed method. The associated wavelet functions are defined by:

$$\Psi_{a,\vec{b},\theta}(\vec{x}) = \frac{1}{a} \exp\left(\frac{-\|\vec{x}-\vec{b}\|^2}{2a^2}\right) \exp\left(\frac{5i(\vec{x}-\vec{b})\cdot\vec{r}}{a}\right) \quad (4.5\ 2)$$

where  $\vec{r} = (\cos \theta, \sin \theta)$  and  $\vec{x}$  is a two-dimensional spatial vector.

The *SH* scene (i.e., the scene having higher spatial resolution) is convoluted by the wavelet functions given the spectral matrix  $W$ :

$$W_{a,\vec{b},\theta}(\vec{x}) = \iint_{\mathbb{R}^2} I(\vec{x}) \Psi_{a,\vec{b},\theta}(\vec{x}) dx^2 \quad (4.5\ 3)$$

where  $I(\vec{x})$  is the subscene function.

Once the wavelet transform matrix  $W$  has been computed, it can be expressed in the form  $W_{\vec{x}}(a, \theta) = W_{\vec{x}}(\lambda, \theta)$  with  $\lambda$  related to  $a$  by  $\lambda = 2\pi a L_S / 5$  and with  $L_S \times L_S$  being the dimension of the subscene function under consideration,  $I(\vec{x})$ . This means that for a particular location  $\vec{x}$ , the matrix  $W$  depends only on wavelength and wave direction.

Morlet wavelets were applied to subscenes of variable dimension ( $L_S \times L_S$ ) so that each subscene contains at least two wave crests and two wave troughs.  $L_S$  was estimated based on preliminary wavelength estimates (FFT or visual inspection). To avoid boundary effects, only the wave spectra in a two times smaller area (dimension  $L_S/2 \times L_S/2$ ) centered on each subscene are used in the following steps. The wavelet spectra are computed using input subscenes with resolution  $DX_{WA}$ . Theoretically, wavelet analysis makes it possible to compute wavelength spectra at the same resolution ( $DX_{SH}$ ) as the pixels of the *SH* scene (for instance, 2.5 m for panchromatic SPOT-5 images). If computation time must be decreased,  $DX_{WA}$  can be reduced, but should still be small enough to characterize the wavelengths properly. Then, by spatial averaging, mean wavelength spectra are computed at a resolution of  $DX_{WO}$ . Then the subscenes are recovering each other to cover all the scenes with regularly spaced wavelength spectra  $W_{\vec{x}}(\lambda, \theta)$ , at resolution  $DX_{WO}$ .

Once the wavelength spectra  $W_{\vec{x}}(\lambda, \theta)$  have been computed,  $N$  dominant wavelengths are extracted numerically to cover a wide range of waves, e.g., several superimposed waves. To achieve this, the local energy maxima  $|W_{\vec{x}}(\lambda_n, \theta_n)|$  are assumed to identify the  $(\lambda_n, \theta_n)$  polar coordinates ( $n$  varying from 1 to  $N$ ) associated with each main local wave climate. In this method,  $N$  will always be

less than or equal to a fixed maximum number of local maxima, called  $N_{max}$ , to avoid excessive and unnecessary computation time (this point will be discussed further in Section IV).

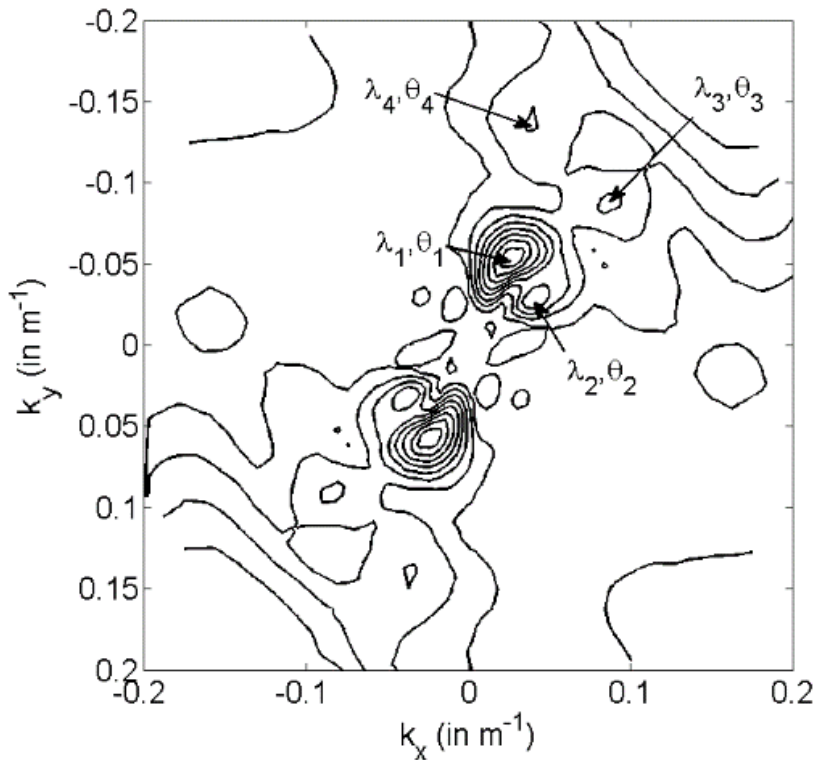


Fig. 4.5 4. Normalized wave amplitude spectrum  $W_{\bar{x}}$  at the P1 location (white cross in Fig. 3b). The spectrum is expressed in terms of wave number in the  $(k_x, k_y)$  plane using the following convention:  $k_x = 2\pi \sin(\theta)/\lambda$  and  $k_y = 2\pi \cos(\theta)/\lambda$ . The dimensionless maximum spectral intensity is  $W_{\bar{x}} = 0.1$ , and the contour intervals are **0.01**.

A representation of a wavelength spectrum obtained at point P1 (located in Fig. 4.5 3b) is given in Fig. 4.5 4. In this case, four significant dominant waves were detected. If more than  $N$  significant waves can theoretically be produced, the spectral mode search can be limited to the more relevant ones in terms of energy. At this step, one may note that most of the time the wind wave is rejected because it has not a sufficient energy. On the one hand, it is necessary to localize the local maxima robustly with respect to their neighborhood and to spectral noise. On the other hand, it is clearly desirable to identify wavelength domains (large enough to take advantage of the dispersion phenomenon) around each maxima. It is therefore necessary to focus on spectral peaks with high energy compared to other wavelengths and peaks spread over significant wavelength ranges. Indeed, the dominant waves, wind wave or swell, are associated to bumps distributed around a local maximum and not just to a peak value of Dirac type. These bumps are well described by the clouds  $(\lambda, c)$ . Some studies had been led to distinguish the wind wave from the swell, as for example in [22].

Other methods use also the detection of local maxima to detect the dominant waves in the wave spectrum as Boccia et al., 2015. This choice will be further discussed and its relevance illustrated in the application section III.

Determination of  $(\lambda_{n,m}, c_{n,m})$  couples and water depth  $h_n$  associated with each dominant wave  
 Before computing the wave celerity, in the case of images having different spatial resolution (this is the case for panchromatic and multispectral SPOT-5 images), the lowest-resolution scene ( $SL$ ) should be oversampled to match the higher-resolution scene ( $SH$ ) to correlate images of the same step size  $DX_{SH}$ . Oversampling of the  $SL$  scene is preferable to downsizing of the  $SH$  scene to improve the precision on the wave displacement. This operation is carried out by applying a bi-cubic interpolation to the  $SL$  scene.

In the current study, Fourier filtered subscenes are not used to compute celerity as in de Michele et al., 2013 or Poupardin et al., 2014. Indeed, the spatial resolution given by the Fourier transform subscenes is too coarse to isolate the dominant wavelength  $\lambda_n$  as determined by the wavelet analysis, particularly for the largest wavelengths. Once the wavelet spectrum has been obtained and the energy maxima and their corresponding wavelength ( $\lambda_n$ ) identified, the method consists of selecting several wavelength values  $\lambda_{n,m}$  around the dominant wave length  $\lambda_n$ , keeping  $\theta = \theta_n$  and  $m$  varying in the  $[1, M]$  interval, but corresponding to sufficient spectral energy to distinguish them from background noise. The next step is to compute the celerities associated with each  $\lambda_{n,m}$ . This approach is inspired by the method proposed in Piotrowski and Dugan, 2002 who considered several  $(f, \lambda)$  couples in the dominant wave direction, but adapted to the lack off access to frequencies on the basis of a high-temporal-resolution camera. Only one pair of two images separated by a phase lag ( $DT$ ) of a few seconds can be accessed. Considering the spectrum  $W_{\vec{x}}$  at a point on the grid,  $M$  couples  $(\lambda_{n,m}, \theta_n)$  with spectral energies larger than a threshold related to the energy maximum are defined as follows:  $TC \times |W_{\vec{x}}(\lambda_{n,m}, \theta_n)|$ . This approach aims to take into account only  $(\lambda_{n,m}, \theta_n)$  couples whose energy is still relatively close to one of the  $n$  dominant modes  $(\lambda_n, \theta_n)$ .

Next, the celerity can be estimated for each wavelength. At each point on the  $DX_{WO}$  grid, for each scene, subscene wavelet transforms were recomputed considering only the direction  $\theta_n$  and the wavelength  $\lambda_{n,m}$ . Contrary to the section II-A where the resolution  $DX_{WA}$  was used to reduce the computation time, to compute the wave displacements, the subscenes are considered on their full resolution  $DX_{SH}$  (i.e. at the pixel resolution). It does not represent a loss in time because the computation is realized for only one set of wavelet parameters (direction  $\theta_n$  and wavelength  $\lambda_{n,m}$ ). Relations (4.5 2) and (4.5 3) were used with  $a = 5\lambda_{n,m}/2\pi L$  and  $\theta = \theta_n$  to compute the two spectra, which were expressed in the form  $W_{n,m}(\vec{x}) = W_{\lambda_{n,m}, \vec{b}, \theta_n}(\vec{x})$ : one spectrum for each subscene ( $SH$ ,

$SL$ ). Then, for each subscene, the real part of the spectrum was used to identify the wave shape precisely, from the crest to the trough. A crest is located when the wavelet and the subscenes are in phase, and a trough is located when the wavelet and the subscenes have opposite phase. The cross-correlation was applied to a spectral window of dimension  $L_S/2 \times L_S/2$ , giving the cross-correlation matrix  $CC_{n,m}(i, j)$ :

$$CC_{n,m}(i, j) = \sum_{k=0}^{S-1} \sum_{l=0}^{S-1} Re(W_{n,m}^{SH}(k, l)) \times Re(W_{n,m}^{SL}(k - i, l - j)) \quad (4.5 4)$$

where  $S$  is the window size (i.e., the number of pixels),  $(i, j) \in [-(S - 1), S - 1]$  are the indexes associated with the displacement in pixels. Correlation computations were carried out with the `xcorr2` function of Matlab.  $CC_{n,m}$  is the cross-correlation matrix of size  $(2 \times S - 1, 2 \times S - 1)$ .  $Re(W_{n,m}^{SH})$  (or  $Re(W_{n,m}^{SL})$ ) is the real part of the wavelet transform corresponding to the wavelength  $\lambda_{n,m}$  and oriented by  $\theta_n$  as applied to the  $SH$  (or  $SL$ ) image. The maximum value of the matrix  $CC_{n,m}$  gives the displacement  $d_{n,m}$  between the two images, corresponding to the wavelength  $\lambda_{n,m}$  and oriented by  $\theta_n$ . Then the celerity  $c_{n,m}$  corresponding to the wavelength  $\lambda_{n,m}$  can be deduced by considering the temporal lag  $DT$  between the two scenes ( $c_{n,m} = d_{n,m}/DT$ ). The quality of the correlation  $Q_{n,m}$  is given by the maximum of  $CC_{n,m}$  normalized by the product of

$$\sum_{k=0}^{S-1} \sum_{l=0}^{S-1} Re(W_{n,m}^{SH}(k, l))^2 \text{ by } \sum_{k=0}^{S-1} \sum_{l=0}^{S-1} Re(W_{n,m}^{SL}(k, l))^2$$

which represents the auto-correlations of the real parts of both wavelet transforms. Fig. 4.5 5 provides an illustration of the center part of a subscene of the image pair and of the real part of its wavelet transforms.

Applying this procedure for every index  $m \in [1: M]$ , a point cloud  $(\lambda_{n,m}, c_{n,m})$  is obtained, which is represented in the  $(\lambda, c)$  plane and completes the characterization of the  $n^{th}$  dominant wave regime  $(\lambda_n, c_n)$ . Then, using a Levenberg-Marquardt algorithm, the water depth  $h_n$  which minimizes the sum of squares of the distance between the point cloud and the dispersion curve given by (4.5 1) can be estimated. To perform this adjustment, a weight is associated with each point  $(\lambda_{n,m}, c_{n,m})$  depending on the quality of the correlation  $Q_{n,m}$ . Fig. 4.5 2 provides an illustration for a case with four dominant waves.

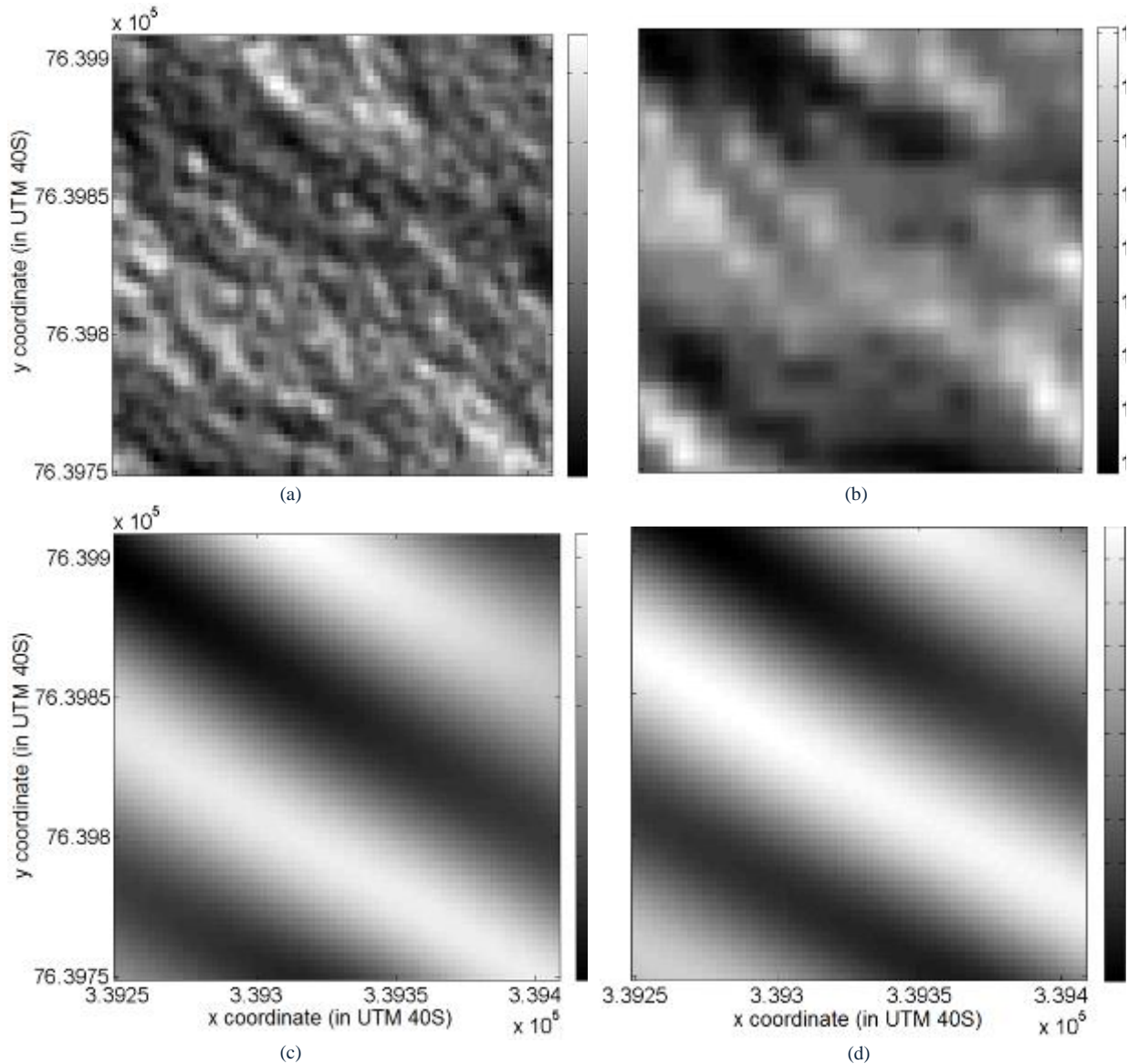


Fig. 4.5.5. Windows of **160 m × 160 m** centered on panchromatic (a) and multispectral (b) subscenes (in grayscale) and on the dimensionless real part of their respective wavelet transforms (c) and (d) corresponding to the P1 location (white cross in Fig. 3b). Use of  $\lambda_{1,1} = 85.4 \text{ m}$  and  $\theta_1 = 2.62 \text{ rad}$  for the wavelet transform.

#### Choice of water depth $\hat{h}$ among the $N$ bathymetric values $h_n$

On each point of the  $(DX_{W0} \times DX_{W0})$  grid, the proposed method is applied to the  $N$  dominant waves and therefore provides  $N$  depth values  $h_n$ , with  $n$  varying from 1 to  $N$ . (for an illustration, see Fig. 4.5.2). A first natural approach to select the “best” water depth  $\hat{h}$  among the  $N$  bathymetric values  $h_n$  would be to use the error on  $h_n$  estimated during the above LM inversion. However, due to the non linearity of the dispersion relation, the reliability of the obtained  $h_n$  is not really characterized by its deviation on  $h_n$ , but rather by the quality of its associated  $(\lambda_{n,m}, c_{n,m})$  cloud and how it follows the  $h$ -dispersion curves. For instance, for a single metric error on  $h_n$ , depending on the

depth, a cloud with characteristics that are not the best aligned with the  $h$ -dispersion curve could be chosen, depending on the  $h_n$  candidate values. Therefore, an alternative approach is proposed here, which focuses on proper wave detection in the  $SH$  and  $SL$  subscenes, so that the  $n^{\text{th}}$  dominant wave which maximizes the product  $PW = |W_{\tilde{x}}^{SH}(\lambda_n, \theta_n)| \times |W_{\tilde{x}}^{SL}(\lambda_n, \theta_n)|$  can be identified. Noteworthy is the fact that the dominant modes must be found on both panchromatic and multispectral scenes. Otherwise, the dominant waves will be rejected by our criterion  $PW$ . In other words a mode is determined on the panchromatic image for having the best possible precision but it is used for  $h$ -derivation only if the mode is also detected using the multispectral image. That points out the importance of the  $PW$  criterion for rejecting *a posteriori* irrelevant modes (i.e. modes that are observed in  $SH$  but not in  $SL$ ) during the process.

Within the method, the dispersion of the  $(\lambda_{n,m}, c_{n,m})$  cloud around the fitted dispersion curve is largely due to the lack of precision in the celerity estimate  $c_{n,m}$ . To avoid using clouds characterized by too-large celerity errors, the two following rejection conditions of the  $h_n$  estimate associated with the  $n^{\text{th}}$  cloud were used: (1) if the standard deviation of the celerity within the  $n^{\text{th}}$  cloud is larger than a given threshold (parameter called  $C_C$ , see Table 4.5 1), then  $h_n$  is rejected; (2) an additional threshold is used so that all estimated  $h_n$  outside the given range of bathymetric values are rejected (a parameter called  $DZ$ , see Table 4.5 1). The possible causes of threshold violation can be various kinds. First, the displacement estimate can be of poor quality for low-spectral-energy modes, resulting in a high standard deviation on the celerity. It is worth noting that the selection and sorting of the first five modes by decreasing  $PW$  value does not assess the global quality of their estimates but rather their relative importance in the image, and therefore the possibility that the first modes result in poor  $c_{n,m}$  estimation cannot be rejected. Second, for a given depth and the same standard deviation on  $c_{n,m}$ , the process can result in aberrant  $h_n$  values for the shortest wavelengths (where the  $h$ -curves corresponding to strongly different  $h$  values are too close to each other with respect to the amount of precision in  $c_{n,m}$ ). However, the main factor used in selecting  $h_n$  is based on the maximizing the product  $PW$ , with the two thresholds  $C_C$  and  $DZ$  being only secondary factors. The influence of these thresholds on the final estimated bathymetry, as well as the advantages of using such thresholds will be discussed in Section IV.

#### Application and results

To investigate the potential of the developed method, it was applied to a SPOT-5 image pair acquired on February 6, 2010, at 10:30 AM in the area of Saint-Pierre, located on the southwest of La Réunion Island (Fig. 4.5 3 shows the panchromatic scene). It occurs at the falling tide, 1h30 before the low tide. This experimental area is characterized by a short continental shelf a few kilometres

width. On this site and this date, there is no current measurement or hydrodynamic model results of high spatial resolution. Thus, we used the results of the global model NCOM (Navy Coastal Ocean Model, NOAA). At the global scale, this model provides local surface currents of about 0.1 m/s and 0.14 m/s, the 6th February of 2010 at 6 and 12 AM respectively. These currents remain weak enough to not be considered in the dispersion relation. It is the same site as that used by de Michele et al., 2013. Furthermore, this site is covered by *in-situ* measurements realized by LIDAR (from Litto3D® products, see [www.shom.fr](http://www.shom.fr) for more details) for depths less than 30 m and by single-beam echosounder (SHOM data, see [data.shom.fr](http://data.shom.fr)) for deeper water. These *in-situ* measurements are used as a reference to validate the proposed method. A representation of this measured bathymetry is shown in Fig. 4.5 6a.

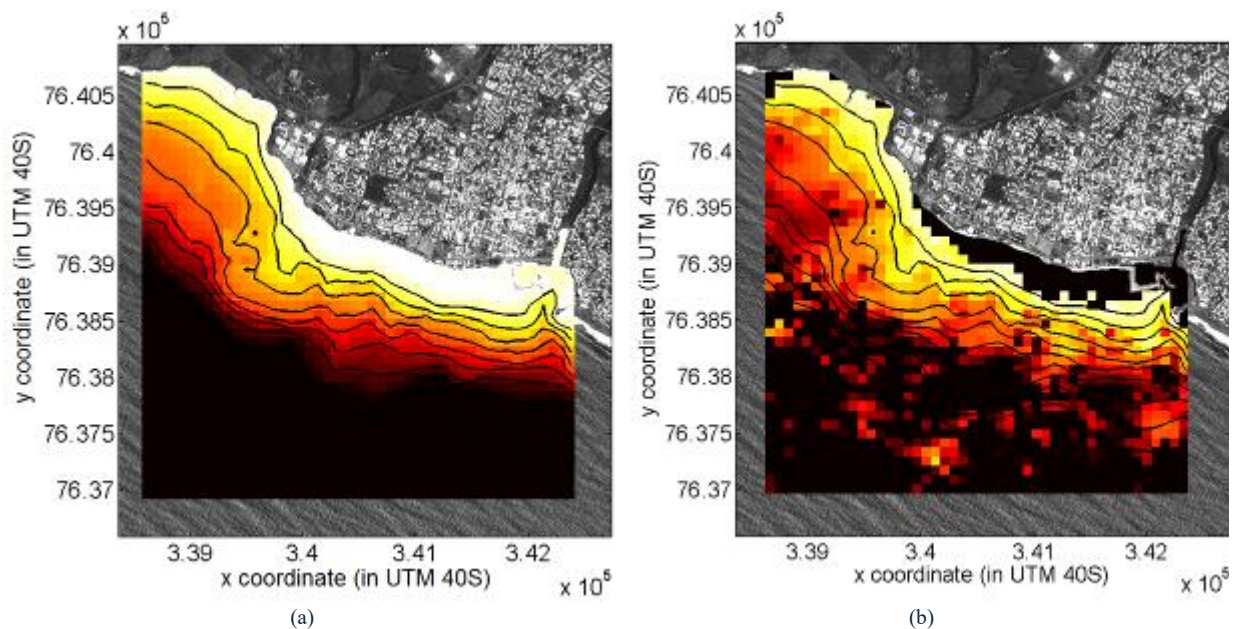


Fig. 4.5 6. (a) *In-situ* measured bathymetry (in m) on an **80 m** × **80 m** grid realized by LIDAR (from Litto3D products) for depths less than **30 m** and by multi-beam echo sounder (SHOM data) for deeper water. The isobaths are represented by black curves and are plotted each **5 m** until **50 m**. The vertical reference of the bathymetry is the hydrographic zero (SHOM convention). (b) Estimated bathymetry (in meters) on an **80 m** × **80 m** grid from the SPOT-5 dataset. The black curves represent the isobaths at each **5 m** given by the *in-situ* measurements. The black area near the coast is not covered by the method.

SPOT-5 is a satellite equipped with a High-Resolution Geometry (HRG1-2) sensor which acquires data in multispectral mode (HS) at  $DX_{SL} = 10$  m spatial resolution and in panchromatic mode (HMA) at  $DX_{SH} = 2.5$  m spatial resolution. The temporal shift between the HMA and HS acquisitions is  $DT = 2.04$  s. As shown in de Michele et al., 2013, this configuration makes it possible to compute

wave celerities corresponding by correspondence with the displacement of a cluster of pixels over time.

In conjunction with the HMA band, three multispectral bands (XS1-2-3) can be used to estimate wave celerity. The XS1 multispectral band (green) with a spectral bandwidth centered on  $0.55 \mu\text{m}$  has been chosen because it is the band whose spectral bandwidth best matches that of the HMA panchromatic band (for the ocean surface). This consideration is important to obtain good image cross-correlation scores Necsoiu et al., 2009. A spatial shift was found between the XS1 multispectral band and the HMA panchromatic band. Because it can be assumed that the land-based parts of both bands do not move in the temporal lag  $DT$  of 2.04 s, this spatial shift can be measured on land and then compensated for by applying a constant offset to the XS1 multispectral band.

#### Application of the method

Within the CWB method, several types of parameters must be set: some related to satellite-image characteristics, others from the site and from observed waves, and others using the conventional method. Table 1 contains all the parameter values associated with application of the method to the study site and use of SPOT-5 images.

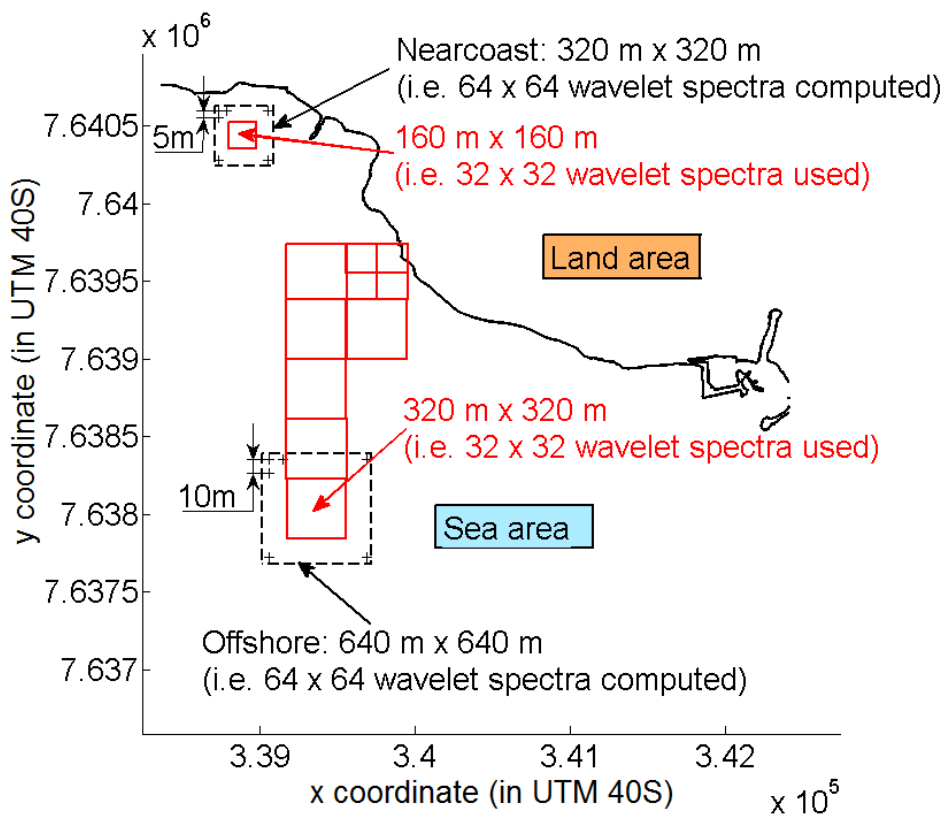


Fig. 4.5 7. Subscene dimension and resolution depending on distance from the coast.

The subscenes sizes ( $L_S$  ranging from 640 m offshore to 320 m nearshore) were estimated on the basis that the more energetic wavelengths typically range from approximately 250 m offshore to approximately 100 m near the coast where the bathymetry is much shallower, enabling consideration of at least two wave crests and two wave troughs for each subscene. Subscene dimensions and resolutions are shown in Fig. 4.5 7. In this application, the two images have different spatial resolutions ( $DX_{SH}$  and  $DX_{SL}$ ), meaning that computation of the dominant waves was done on the panchromatic image (resolution  $DX_{SH}$  of 2.5 m), and the multispectral image of resolution  $DX_{SL}$  (i.e., 10 m) was oversampled at the resolution  $DX_{SH}$  of the panchromatic images.

Theoretically, wavelet analysis makes it possible to compute wavelength spectra at the same resolution as the pixel the panchromatic pixels (i.e., 2.5 m), but to save time, this resolution was reduced to  $DX_{WA} = 10$  m offshore and to  $DX_{WA} = 5$  m near the shore. This resolution allows detecting modes with wavelengths superior to 20 m offshore and to 10 m near the coast. Then mean wavelength spectra were computed at a resolution  $DX_{WO}$  of 20 m. This means that the average took into account  $2 \times 2$  wavelength spectra offshore and  $4 \times 4$  wavelength spectra near the coast. This choice was made as a compromise between computation time and physical description of wave characteristics. Indeed, a preliminary analysis (not shown here) based on wavelength variograms showed that the 20 m value was always less than the correlation of the detected wavelength (from 100 to 200 m depending on the spatial areas considered for variogram analysis). This means that the subscenes overlap to cover the entire scene with regularly spaced wavelength spectra  $W_{\vec{x}}(\lambda, \theta)$  (20 m resolution). A representation of the corresponding wavelength spectrum  $W_{\vec{x}}(k_x, k_y)$  for point P1 is given in Fig. 4.5 4. In this case, the four following dominant waves were detected: (1)  $\lambda_1 = 102.5$  m,  $\theta_1 = 150^\circ$ ; (2)  $\lambda_2 = 122.9$  m,  $\theta_2 = 128^\circ$ ; (3)  $\lambda_3 = 49.4$  m,  $\theta_3 = 135^\circ$ ; (4)  $\lambda_4 = 45.1$  m,  $\theta_4 = 165^\circ$ .

For the maximum number of modes (i.e., clouds) for which bathymetric values were estimated, an  $N_{max}$  value of 5 was selected. For the maximum number of  $(\lambda, c)$  pairs per cloud, a value of  $M = 16$  was chosen. For the threshold  $TC$  related to the energy maxima of the  $(\lambda_n, c_n)$  couples, based on some preliminary tests, a value of 0.65 was selected. Fig. 4.5 2 provides an example of the clouds obtained for point P1 (location indicated in Fig. 4.5 3b). In this case, four dominant modes, and therefore four clouds, were identified. This provides a reasonable number of points to estimate the bathymetry  $h_n$  (illustration in Fig. 4.5 2). For the last step of water depth selection among the  $N$  values,  $C_c$  was set to 1 m/s, whereas the depth range  $DZ$  was set to [1 m - 100 m]. The thick line in Fig. 4.5 2 indicates the selected  $\hat{h}$  value for location P1, which was used for comparison with the dispersion curve obtained using the *in-situ* water depth (obtained from LIDAR and multi-beam measurements).

As a comment on the relevant  $N_{max}$  value, analysis of the selected water depth  $\hat{h}$  shows that most of the time, the first or second mode was selected for the final bathymetry estimation (Fig. 4.5 8), which indicates that there is no need to analyze more than  $N_{max} = 5$  dominant waves. From the CWB selection process (one criterion and two thresholds), long waves were most often selected. Note that the longest waves are most impacted by the bottom Holman et al., 2013.

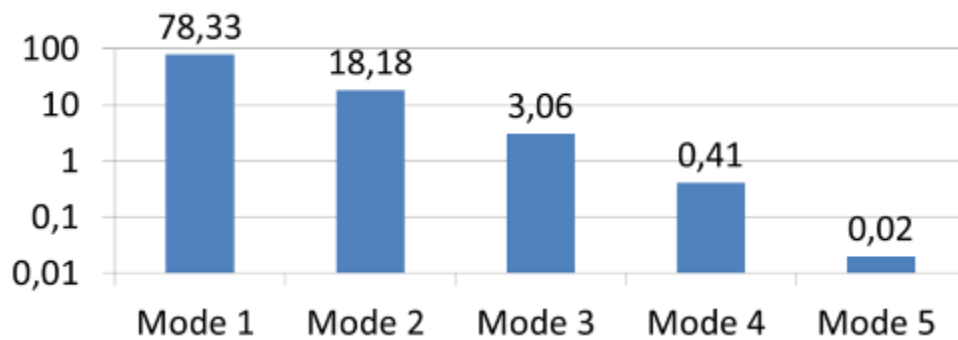


Fig. 4.5 8. Selection percentage of the modes. The modes are the maxima of spectral energy (Mode 1 (i.e.,  $n = 1$ ) being the most energetic and Mode 5 (i.e.,  $n = 5$ ) the least energetic).

### Results

The bathymetry  $\hat{h}$ , estimated from the SPOT-5 dataset, is shown in Fig. 6b on an 80 m × 80 m grid, which was obtained by spatially averaging the 20 m resolution bathymetric grid. It has also been corrected by taking tides into account, so that the vertical reference of the obtained bathymetry is the hydrographic zero (SHOM convention, corresponding more or less to the lowest tidal level). Indeed, the sea level was 0.51 m above the reference level (hydrographic zero) when the SPOT-5 satellite took the scenes on February 6, 2010, at 10.30 am. In Fig. 4.5 6b, the isobaths correspond to the *in-situ* measurements  $h_{in-situ}$ . It should be remembered that the area after wave breaking is not covered by the CWB method (in black in Fig. 4.5 6b). A qualitative good agreement with observations can be seen: the proposed method properly reproduces the main morphologic features. For instance, the short continental shelf is described, with a bathymetry reaching 50 m depth at 1 km from the coast. The estimated bathymetry  $\hat{h}$  decreases faster near the harbor (right part of the scene) than where the coast exhibits a concave curve (left part of the scene). Furthermore, the method succeeded in identifying the submerged headland at the  $(3.34 \times 10^5 \text{ m}, 76.36 \times 10^5 \text{ m})$  UTM location (Fig. 4.5 6b).

To quantify the quality of the results, maps of the absolute error ( $AE = \hat{h} - h_{in-situ}$ ) and the

relative error ( $RE = (\hat{h} - h_{in-situ})/h_{in-situ}$ ) are shown in Figs. 4.5 9a and 4.5 9b. The relative error is strongly non-uniform, ranging overall from  $-100\%$  to  $+100\%$ , with most values ranging from  $-50\%$  to  $+50\%$ . Errors very close to  $0\%$  can also be observed, and it corresponds to location where the CWB method works better because the dominant waves may clearly be identified on the scene.

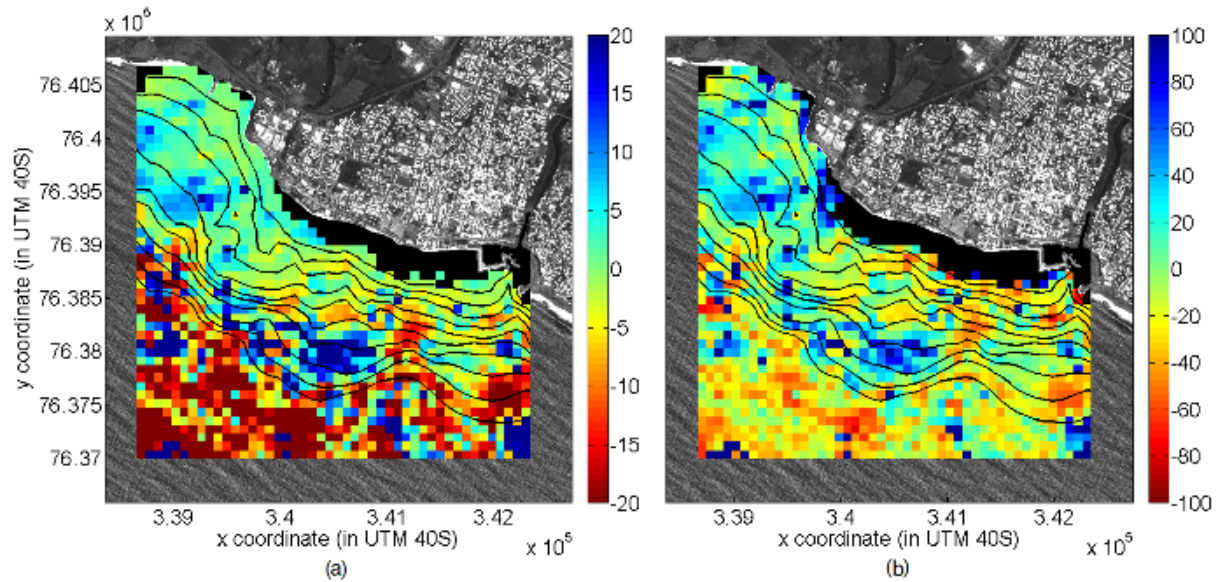


Fig. 4.5 9. Absolute (a) and relative (b) errors in bathymetry (in meters and in % respectively) on an  $80\text{ m} \times 80\text{ m}$  grid from the SPOT-5 dataset. The black curves represent the isobaths at each  $5\text{ m}$  until  $50\text{ m}$  given by the *in-situ* measurements. The black area near the coast is not covered by the method.

To analyze these errors versus water depth, for each  $80\text{ m} \times 80\text{ m}$  bathymetric cell,  $\hat{h}$  is plotted versus  $h_{in-situ}$  (Fig. 4.5 10a). First, the scatter decreases with water depth until approximately  $3\text{ m}$  and then increases with water depth. Second, with regard to quantile: (1) for water depth less than  $3\text{ m}$ , the estimated bathymetry overestimates the real bathymetry; (2) for water depth in the range  $[3\text{ m} - 20\text{ m}]$ , the estimated bathymetry exhibits fairly good agreement with *in-situ* observations; and (3) for water depth greater than  $20\text{ m}$ , the estimated bathymetry underestimates the real bathymetry. These discrepancies may be attributed to a non-optimal selection of the depth  $h_n$  among the  $N$  dominant waves at a given location or to an inaccurate estimate of the celerities. Furthermore, some dominant waves may not have been detected at several locations of the basic panchromatic scene (Fig. 4.5 3b) because of low wave amplitudes.

To complete the analysis of errors versus water depth, the average absolute error ( $ER_1 = 1/K \times \sum_{[h_1, h_2]} |AE|$ ) and the average relative error ( $ER_2 = 1/K \times \sum_{[h_1, h_2]} |RE|$ ) were computed for

several  $h_{in-situ}$  corresponding to the  $h_{in-situ}$  quantiles. Such error indicators were used to avoid negative and positive errors which counterbalance each other. Fig. 4.5 10b shows that absolute error first decreased with water depth for the first two quantiles, and then increased with water depth from 1.5 to 22 m, whereas the relative error remained almost constant, ranging from 20 to 30 %, except for the two smallest water-depth quantiles.

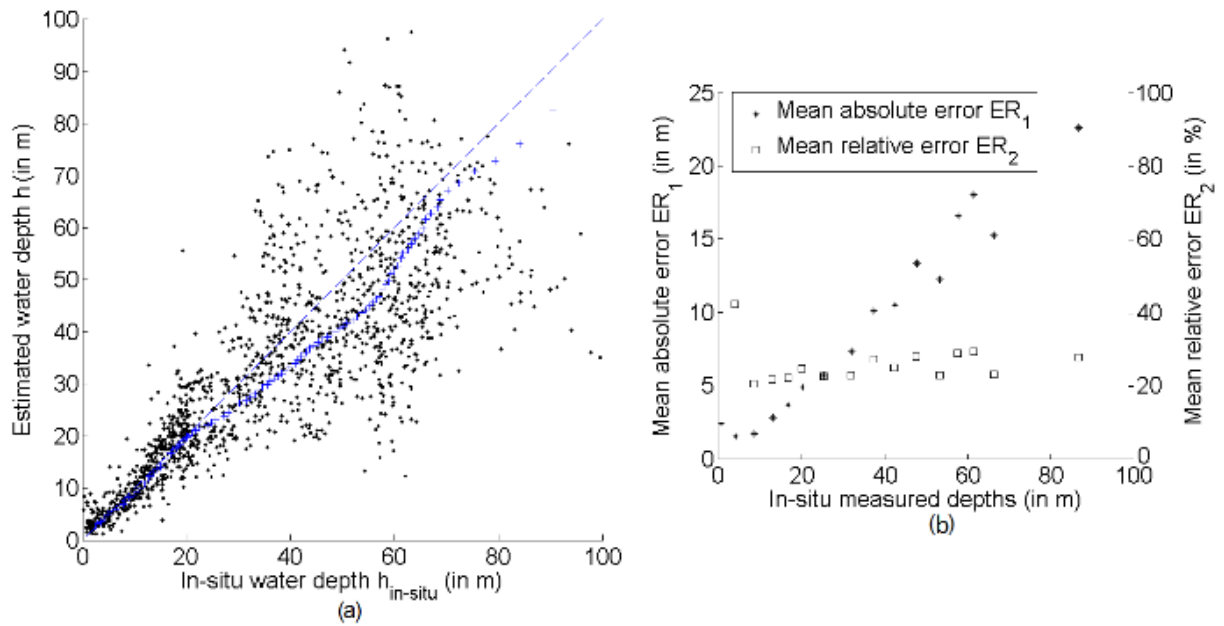


Fig. 10. (a) Water depths  $\hat{h}$  estimated from the satellite dataset versus *in-situ* measured water depths  $h_{in-situ}$  considering all the points of the **80 m × 80 m** grid. The blue crosses represent the 100 percentile ranks computed from  $h_{in-situ} = 2$  m. (b) absolute (\*) and relative (□) errors in bathymetry (in meters and in % respectively) for the 15 quantiles of *in-situ* measured depth.

### Discussion

This paper describes the preliminary development of a method which aims to provide bathymetric information from a single pair of satellite images without any *in-situ* observations and its application to a SPOT-5 dataset. First, the magnitude of the errors obtained will be discussed in comparison with the errors obtained in the study of Leu and Chang, 2005. To analyze the outcomes of the CWB method more thoroughly, the methodological choices made in this research will be discussed and justified using supplementary computations. The limits of the dispersion relation and the associated uncertainty propagation are also analyzed, before making recommendations for using such methods on other sites and with other images.

#### Discussion: Error comparison with Leu and Chang, 2005

Most bathymetric methods using optical satellite images are based on wavelength estimation and

assume a uniform wave period. Here, a comparison of the error magnitudes obtained with the CWB method and with the most widely used method will be presented. Differences in images, sites, investigated water-depth range, and wave characteristics make impossible any rigorous comparison of the quality of the results with the results obtained by other authors using other techniques. However, to make the various configurations as comparable as possible, the problem can be made partially dimensionless based on wavelength characteristics. This leads to the following dimensionless numbers:  $R1 = \hat{\lambda}/h_1$ ,  $R2 = \hat{\lambda}/h_2$  and  $R3 = \hat{\lambda}/dx$ , where  $\hat{\lambda}$  is a characteristic offshore wavelength,  $h_1$  and  $h_2$  the lower and upper bounds of the depth range for which the errors are quantified, and  $dx$  the bathymetric grid resolution. This approach is used to compare the results presented here to those of Leu and Chang, 2005 obtained assuming a uniform wave period. In that study, they obtained a mean relative error  $ER_2$  of 16.2 % in the [2 m, 20 m] range for local characteristics such that  $\hat{\lambda} \approx 60$  m,  $h_1 = 2$  m,  $h_2 = 20$  m, and  $dx = 200$  m; therefore:  $R1 = 30$ ,  $R2 = 3$ , and  $R3 = 0.3$ . Using these parameters for this study and considering an offshore characteristic value  $\hat{\lambda} \approx 150$  m, the results were  $h_1 = 2$  m,  $h_2 = 50$  m, and  $dx = 500$  m. Estimating  $ER_2$  with these characteristics ( $h_1, h_2, dx$ ) led to an error  $ER_2$  of 14.9 % in the [5 m, 50 m] range. This error is of the same order as that reported by Leu and Chang, 2005. However, it should be noted that the bathymetry in the Saint-Pierre area is particularly difficult to estimate because the bed slope is two to three times steeper than in Leu and Chang, 2005, the bathymetric lines are not parallel, and the sea bed is of coral origin and is therefore characterized by small-scale bathymetric heterogeneity.

#### Discussion: Methodological choices

The CWB method relies on several methodological choices made during its development. To analyse the outcomes of the proposed method more thoroughly, the added value of the following methodological choices will be illustrated: (C1) using  $(\lambda, c)$  couples rather than  $\lambda$  and assuming a uniform period to estimate bathymetry; (C2) using the real part of wavelet analysis rather than Fourier-filtered scenes to compute  $c$ ; (C3) considering clouds rather than a single pair  $(\lambda, c)$  to estimate the bathymetric values  $h_n$ ; (C4) choosing a “best” water depth  $\hat{h}$  among the  $N$  bathymetric values  $h_n$  rather than using all couples  $(\lambda, c)$  to estimate a single bathymetric value; and (C5) using  $c$ -STD (the celerity standard deviation) and bathymetric range thresholds to reject aberrant values rather than using only energy criteria. To investigate these choices, additional tests were performed on the study site using the same image dataset. Indeed, this test case is a very challenging one: it is characterized by non-linear bathymetric lines, strong bathymetric heterogeneity, and overlapping of swells and wind waves.

To assess the added value of choice C1 more thoroughly, the bathymetry was estimated using wavelength values only and assuming a uniform wave period. The wave period is usually obtained from offshore buoy measurements. On the study site, there is no offshore buoy. Therefore, the offshore wave period was estimated based on offshore wavelengths and celerities values (172.4 m and 16.1 m/s respectively). These values provided a period value of 10.7 s. This value is consistent with wave modeling results obtained in this area for the time of acquisition of the SPOT-5 images. Then the bathymetry was computed using the dominant mode wavelength. Fig. 4.5 11a shows that the relative errors of this method are generally larger than those associated with the CWB method (Fig. 4.5 8b).

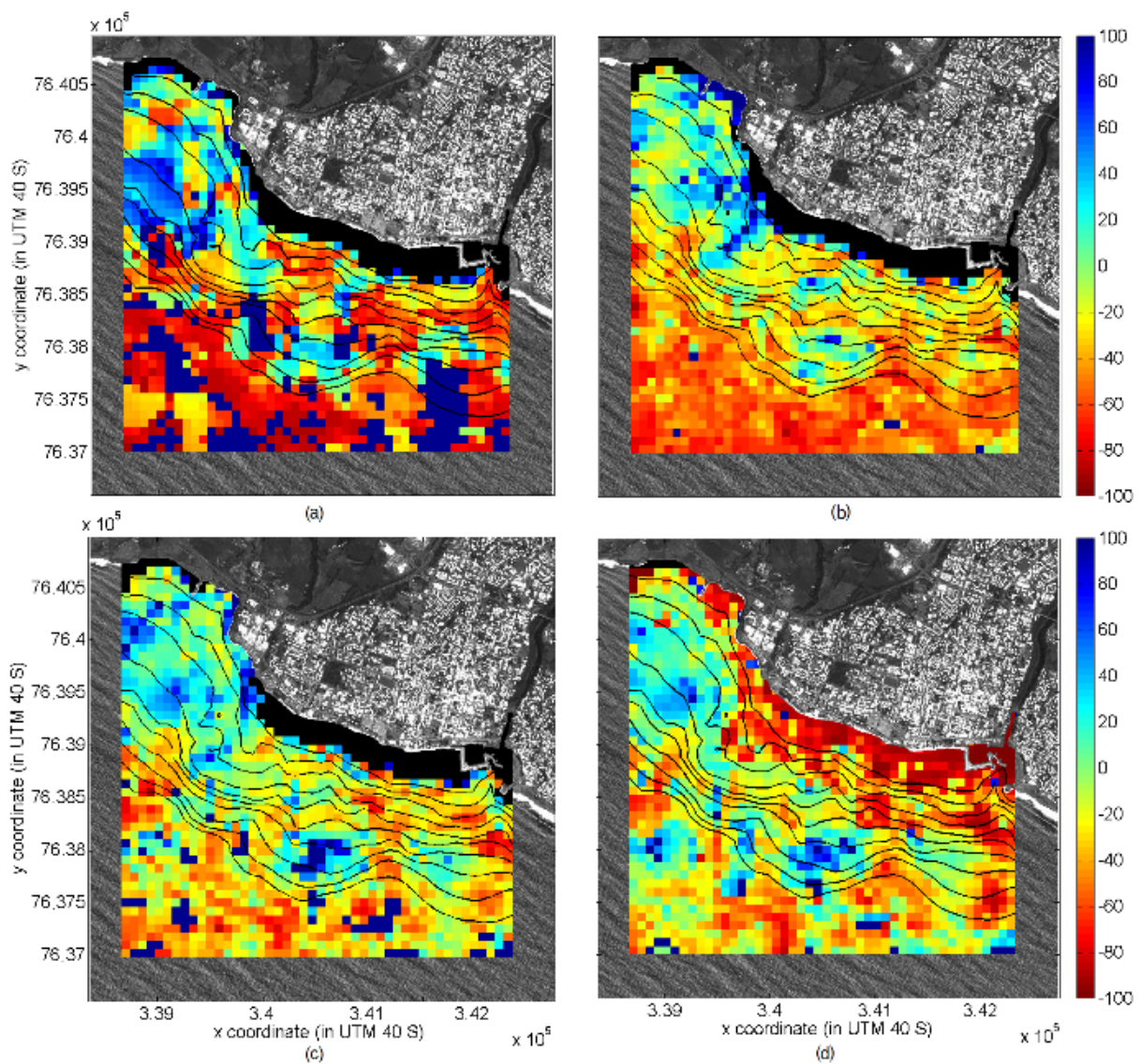


Fig. 4.5 11. Relative errors in bathymetry (in meters) on an **80 m × 80 m** grid from the SPOT-5 dataset for the following cases: (a) assuming a uniform wave period of **10.7 s** to compute the bathymetry, (b) using Fourier-filtered scenes and dominant waves only to compute the celerity, (c) using only dominant wave characteristics to compute the bathymetry, and (d) using all ( $\lambda, c$ ) clouds together to compute a single bathymetric value. The

black curves represent the isobaths each **5 m** until **50 m** given by the *in-situ* measurements. The black area near the coast is not covered by the method.

Focusing on specific areas, it is apparent that, for instance, in the NW, in the 20 – 25 m depth area, the simplified method overestimated the bathymetry by approximately 60 %, whereas the CWB method provided an error close to zero. In the center of the image, there is an area of approximate depth 15 – 20 m where the CWB method also provided an error close to zero, whereas the simplified method underestimated the bathymetry by approximately 60 %. This comparison illustrates the potential improvement provided by using  $(\lambda, c)$  couples over the most widely used method, which is based on the assumption of a uniform period.

As for the improvement obtained using choice C2, Figs. 4.5 11b and 4.5 11c show the bathymetric errors for the two following cases: considering only dominant waves and using Fourier-filtered scenes to compute the celerity (Fig. 4.5 11b), and considering only dominant waves, but using the real part of wavelet analysis to compute the celerity (Fig. 4.5 11c). This comparison shows that in the first case, water depths are strongly underestimated, especially offshore, whereas in the second case, the errors are smaller (globally reduced by a factor of two) than when considering only dominant waves and using Fourier-filtered scenes to compute the celerity. This illustrates the added value of using the real part of wavelet analysis for the subscenes correlation and thus for the celerity computations.

As for the improvements obtained using choice C3, Fig. 4.5 11c shows the bathymetric errors obtained when considering only dominant waves rather than clouds to compute each  $h_n$ . This figure should be analyzed in comparison with Fig. 9b, which provides the errors when clouds are used. Using only the dominant waves leads to larger errors, especially in water depths greater than 40 m and in steep areas.

As for choice C4, Fig. 4.5 11d shows the bathymetric errors when considering all clouds together to compute a single water depth. The relative errors are larger than those obtained using the CWB method (Fig. 4.5 9b), especially in water depths less than 40 m. Indeed, (not shown here) at some locations, the clouds can be very different. For instance, within a cloud, the celerity may appear to be severely underestimated compared with other clouds. In that case, the cloud method makes it possible to avoid mixing well-resolved and poorly-resolved clouds.

Finally, the influence of using thresholds on the  $c$ -STD and the bathymetric range  $DZ$  was investigated (see Table 1). Unlike previous comparisons which were made on the 80 m  $\times$  80 m grid, this analysis was done directly on the 20 m  $\times$  20 m grid.

First, using the  $c$ -STD threshold implies bathymetric change (i.e., a change in the selection of the “best” water depth) over 17 % of the bathymetric grid, mainly for water depths greater than approximately 40 m or where the bathymetric slope is steepest. Using the bathymetric range implies changes in  $\hat{h}$  over 19 % of the grid, mainly offshore (water depth greater than 40 m) and near the coast (water depth less than 1 m). Using both leads to changes over approximately 30 % of the grid, leading to a significant reduction in relative bathymetric errors, mainly offshore (water depth greater than 40 m) and near the coast (water depth less than 1 m). Focusing on the [1 m – 40 m] bathymetric area, using both thresholds leads to changes over approximately 5 % of the grid, mainly in the steepest areas. Therefore, these thresholds mainly contribute to improving the bathymetry near the coast and offshore, whereas they do not significantly modify it in the intermediate bathymetric range [1 m – 40 m]. For water deeper than 40 m, the waves which are no longer impacted by the bottom must be rejected to retrieve the bathymetry. The threshold on the  $c$ -STD is used to avoid using the shortest irrelevant waves. The second threshold based on  $DZ$  acts similarly. As the dispersion relation is no longer valid for water depth in the range  $\lambda/20 > h > \lambda/2$ , the corresponding waves shall not be used to retrieve the bathymetry. In presence of several superimposed waves the best option is to consider one (or several) wave(s) which corresponds better to the relation dispersion domain of validity rather than using all the detected waves.

This analysis illustrates the improvements brought about by: using  $(\lambda, c)$  pairs to estimate bathymetry (C1), using the real part of wavelet analysis to compute  $c$  (C2), considering clouds and estimating one bathymetric value per cloud (C3), choosing the “best” bathymetric value (C4), and using  $c$ -STD and bathymetric range thresholds to complement the “best” bathymetry selection obtained considering only spectral energy (C5).

#### Discussion on Dispersion relation: limits and uncertainty propagation

One source of uncertainty in the CWB method is related to the linear wave dispersion relation itself. This equation is based on the linear wave theory, which provides a linearized description of the gravity-wave propagation on the surface of a homogeneous fluid layer. One of the main assumptions is that the fluid layer has a uniform mean depth. In the present problem, the water depth is not uniform, meaning that in bathymetric estimation, this equation is being used beyond its theoretical. However, most of these studies (including this one) still provide reasonable estimates of water depths. For further discussion on the limitations of the linear dispersion equation, see Holland, 2001.

A second source of uncertainties is related to estimation of the wave characteristics used to compute the water depth. Some authors have investigated the sensitivity of the relative error in depth (estimated using the dispersion relation) to relative errors in frequency  $f$  and wavenumber  $k$  Dalrymple et al., 1998. They showed that the sensitivity of the relative error in depth to relative

errors in  $f$  and  $k$  increases with depth and is greater to relative errors in  $f$  than in  $k$ .

In the proposed method, the data used to estimate the bathymetry using this equation are the wave celerity  $c$  and the wavelength  $\lambda$ . Let us investigate the propagation of uncertainty in  $(\lambda, c)$  using the dispersion relation. Fig. 4.5 12a illustrates theoretical bathymetric variations as a function of  $(\lambda, c)$  values. To investigate uncertainty propagation, the coefficients  $C_C$  and  $C_L$  relating relative bathymetric errors and relative errors to wavelength and celerity respectively are computed numerically:

$$\frac{\Delta h}{h} = C_C(\lambda, c) \frac{\Delta c}{c} + C_L(\lambda, c) \frac{\Delta \lambda}{\lambda} \quad (4.5 5)$$

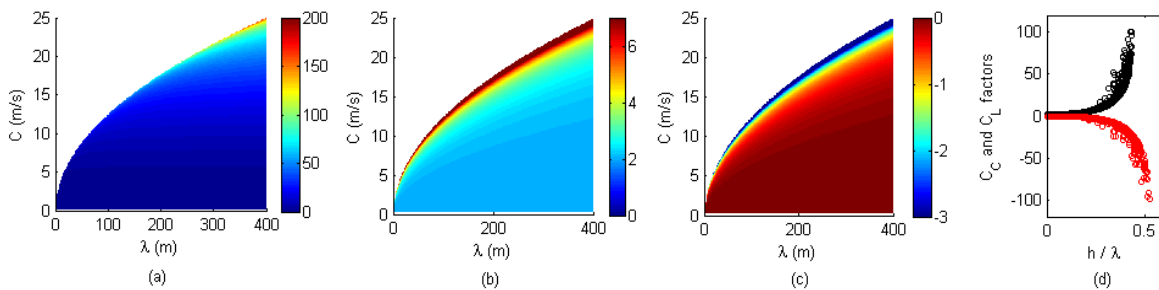


Fig. 4.5 12. (a) Theoretical water depth (in meters), (b) coefficient  $C_C$ , (c) coefficient  $C_L$ , (d) coefficients  $C_C$  (black) and  $C_L$  (red) versus water depth divided by wavelength, the linear dispersion being applicable for  $0.02 < h/\lambda < 0.5$ .

Figs. 4.5 12b and 4.5 12c show the patterns of  $C_C$  and  $C_L$ . First, the relative bathymetric errors are more sensitive to relative celerity error than to relative wavelength error:  $|C_C|$  is generally larger than  $|C_L|$ .  $C_C$  is characterized by a minimum value of 2, meaning that a relative celerity error of 50 % leads to bathymetric errors of at least 100 %. This minimum value corresponds to a wavelength much greater than the water depth (i.e.,  $h/\lambda \rightarrow 0$ ).  $C_C$  increases exponentially with the wave celerity  $c$  (and therefore water depth), decreases with wavelength, and increases exponentially with the ratio  $h/\lambda$ . For instance, at the point  $(\lambda, c) = (100 \text{ m}, 10 \text{ m/s})$ ,  $C_C$  is equal to 2.86, so that an error of 2 m/s (i.e., 20 %) contributes to the relative error in bathymetry by 57 %. The minimum value of  $C_L$  is equal to 0. This can be explained by the asymptote of the dispersion equation, where  $\lambda$  is much larger than  $h$ : in this case, the water depth  $h$  is controlled only by the wave celerity  $c$ .  $C_L$  increases with wave celerity, decreases with wavelength, and its absolute value increases exponentially with the ratio  $h/\lambda$ . For instance, at the point  $(\lambda, c) = (100 \text{ m}, 10 \text{ m/s})$ ,  $C_L$  is equal to

–0.48, so that an error of 20 m (i.e., 20 %) contributes to the relative error in water depth by 10 %.

This investigation highlights that the CWB method is highly sensitive to the quality of the wave celerity estimate. First, even with such high sensitivity, in the [5 m – 40 m] range, the estimated bathymetry is realistic, with a relative error of approximately 25 % (Fig. 4.5 10b) compared to the range of the  $C_C$  factor (generally 2 to 3 in this bathymetric range). Assuming that the wavelength estimation is perfect as well as assuming the linear wave theory, this implies that the relative error of the estimated celerity is approximately 10 %. Reducing the relative celerity error to 5 % should lead to a significant reduction of the relative bathymetric error (by a factor of two). To reduce these celerity errors, it could be interesting to consider the current effect in the dispersion relation even for areas covered by slight currents. As another perspective on reducing celerity errors, it would be worthwhile to investigate the use of sub-pixel displacement methods (de Michele et al., 2013, Michel and Avouac, 2002 and Leprince et al., 2007). Still another perspective would involve applying the procedure to data from higher-resolution sensors keeping acceptable time delay  $DT$ , resulting in better correlation efficiency for a given displacement value.

#### Limitations and recommendations for using the proposed method to analyse satellite images

As shown in Table 1, the CWB method relies on several parameters, some depending on satellite image characteristics ( $DT$ ,  $DX_{SH}$ ,  $DX_{SL}$ ), others on the site (i.e., the wave characteristics at the location and date of image acquisition), and still others on the choice of method, for instance the number of clouds and the number of pairs per cloud. Researchers have no control over the satellite image characteristics, whereas some tuning of site-specific parameters might be possible. In this study, these parameters were selected based mainly on physical considerations (overall wavelengths and variograms) and computation time. Even without any sensitivity analysis, the method provides reasonable results, considering that it is based on only one image pair. This means that it is possible to obtain reliable bathymetry without any tuning. Of course, when possible, a sensitivity analysis should make it possible to obtain better bathymetry. However, it must be recalled that the initial objective was to estimate bathymetry where no data are available, and therefore no reference against which to tune parameters.

As guidelines for using this approach in other areas and on other satellite image types, the following recommendations can be made. As a preliminary condition, the waves should be visible on the images (for instance, bathymetry cannot be retrieved from quiet wave conditions or during rain and storm events). Second, the satellite specific parameters should enable description of the waves, i.e., not too large  $DX_{SL}$  (to enable proper detection of the wavelengths in the wavelet analysis), not too large  $DT$  (to avoid ambiguity in the wave-displacement estimate), and not too small  $DT$  with respect to  $DX_{SH}$  (to enable detection of displacement in the cross-correlation step). This means that

physically, for the procedure presented here, the image/sensor characteristics should be such that:

$$[ DX_{SL} < \lambda/2 \ ; \ DX_{SH} < 2 c DT \ ; \ DT < \lambda/2c ] \quad (4.5\ 6)$$

The first inequality defines the minimum wavelength that can be reliably estimated given the sensor characteristics; the two others define the acceptable celerity range. Equation (4.5 6) provides the critical limit of application of the CWB method. For instance, as  $DX_{SL}$  becomes small, the results will be reliable, but for  $DX_{SL} \geq \lambda/2$ , the wavelength  $\lambda$  will not be detected at all. Therefore, if conditions (4.5 6) are not satisfied, the proposed method cannot be used. If they are satisfied, then the site-specific parameters should be chosen so that the subscenes of dimension  $L_S \times L_S$  contain at least two crests and two troughs (which can be determined by visual inspection), and the grid resolution for wavelet analysis should be small enough to describe spatial wavelength variations properly.

As illustrated in Section III, SPOT-5 images satisfy the application constraints of the CWB method for typical wave characteristics encountered around the world (in open sea, waves have wavelengths and celerities of the same order of magnitude as those encountered on the study site). However, many other systems can potentially provide estimates of bathymetry using such an approach. Among others, the Pléiades system provides panchromatic (multispectral) images of 0.7 m (2.8 m) resolution characterized by a time lag of 0.16 s (CNES, personal communication). With such characteristics, conditions (4.5 6) are satisfied because the expected celerities are greater than 3 – 4 m/s. It is worth noting fact using combinations of stereo pairs instead of bands from the same acquisition would not satisfy the condition. For instance, the minimal  $DT$  between a Pléiades stereo pair of images is approximately 15 s; this means that the celerity at a 100 m wavelength cannot be reliably detected if the celerity is greater than 3.3 m/s . The higher resolution of Pléiades (or equivalent, e.g., SPOT 6/7) will provide a better precision in the correlation computation and better  $(\lambda, c)$  estimates for the shortest wavelengths (in particular in the 5 – 20 m range) by using smaller subscene sizes, providing a more complete representation of the dispersion curve.

In an effort to improve the recommendations, an in-depth sensitivity analysis with respect to wave conditions, image quality, and parameter values should be done. It would be worthwhile to do it on a synthetic case, using hydrodynamic which can simulate wave dynamics and provides instantaneous images of the wave field. This initiative falls outside the scope of this paper, which was to test the feasibility of estimating bathymetry from single-satellite image pairs, under real conditions, without any specific parameter tuning.

Finally, the CWB method has been developed assuming that currents were equal to 0. Such a hypothesis was justified on the application site which is characterized by surface current weaker than 0.14 m/s. To extend the applicability of the CWB method, it would be worthwhile to add currents as

an unknown in the algorithm. The CWB method appears well suited for such integration as it is based on the study of several waves superimposing on each other. Then, as the manner of Piotrowski and Dugan, 2002, once the water depth estimated with the selected dominant wave and, if it exists, the contribution of the current is that direction, we could use the other waves to estimate the current in other directions. This would provide better estimates of bathymetry in areas subject to significant currents, thus extending the field of application, but would also yield estimates of the currents themselves.

<b>Parameter Type</b>	<b>Parameter</b>	<b>Parameter Description</b>	<b>Application specific value</b>
Satellite specific	$DT$	Time lag between images	2.04 s
	$DX_{SH}$	Spatial resolution of the higher-resolution image	2.5 m
	$DX_{SL}$	Spatial resolution of the lower-resolution image	10 m
Site-Wave specific	$L$	Subscene size	640 m (offshore) to 320 m (nearshore)
	$DX_{WA}$	Spatial resolution of images for wavelet analysis	10 m (offshore) to 5 m (nearshore)
	$DX_{WO}$	Spatial resolution of mean wavelength grid	20 m
	$TC$	Threshold related to energy maxima	0.65
	$C_c$	Celerity threshold	1 m/s
	$DZ$	Bathymetric range of research	[1 – 100 m]
	Method specific	$N_{max}$	Maximum number of modes (or cloud)
$M$		Number of $(\lambda, c)$ pairs per cloud	16

Table 3.5 1. Parameters to be estimated for method applications. The values are those corresponding to the SPOT-5 images in the Saint-Pierre area, February6, 2010.

### Conclusions

This study has investigated whether a single SPOT-5 dataset can be used to retrieve bathymetry from space with reasonable accuracy and precision and without any in-situ measurements. To tackle this issue a new method (called CWB) was developed based on wave celerity and wavelength estimates. This method jointly uses: (1) wavelet analysis and cross-correlation to provide  $(\lambda, c)$  clouds (one per detected dominant wavelength), (2) the linear dispersion relation to estimate one bathymetric value per cloud, and (3) criteria to select the “best” estimated bathymetric value at each location. Application of the CWB method to the Saint-Pierre coastal area (La Réunion Island) using one SPOT-5 panchromatic image and the corresponding green multispectral image showed that a single SPOT-5 dataset could be used to retrieve bathymetry from space with reasonable accuracy and precision (absolute relative error of approximatively 20 to 30 % for water depths ranging from 3 to

80 m, with local areas providing errors fairly close to 0 %). A sensitivity analysis to choices made in the CWB method illustrated the improvements brought about by using  $(\lambda, c)$  couples rather than  $(\lambda)$  assuming a uniform period to compute the bathymetry; by using the real part of wavelet analysis rather than Fourier-filtered scenes to compute  $(c)$ ; by considering clouds rather than a single  $(\lambda, c)$  pair to estimate the bathymetric values  $h_n$ ; and by choosing a “best” water depth  $\hat{h}$  among the  $N$  bathymetric values  $h_n$  rather than using all couples  $(\lambda, c)$  to estimate a single bathymetric value. Analysis of the sensitivity of the relative bathymetric errors to the relative errors in celerity and wavelength highlighted the strong sensitivity to celerity errors and the potential for improvement by reducing error in the celerity estimate.

Some guidelines and recommendations have been provided for using the proposed approach on other sites and images. Other systems with higher resolution, such as Pléiades, could provide images, making it possible to extend the measured  $(\lambda, c)$  domain towards shorter wavelengths, thus reducing bathymetric errors.

In comparison with more traditional approaches based on LIDAR, multi-beam echo sounders, or high-frequency time series of ground-based images, the results are coarse at the moment. However, they can certainly be improved in the near future. Being able to estimate bathymetry from space without any *in-situ* measurements opens new perspectives such as, accessing remote and past bathymetries in many areas around the world; completing existing catalogues (e.g., extending the bathymetric catalogues further offshore, or very close to the coast); estimating bathymetry before and between existing *in-situ* acquisitions; and implementing a multi-temporal bathymetric dataset.

## 5. PERSPECTIVES

The forthcoming years will be fruitful for new developments and applications of satellite remote sensing in Earth sciences, and especially solid Earth. I foresee perspectives essentially in

### 1) Deformations of the Earth surface

Improved monitoring of seismotectonic processes using the new generation of observation systems, such as the Copernicus Sentinels. In particular, Sentinel 1 allows global remote sensing measurement of tectonic strain accumulation and release. Enhanced time scale understanding of tectonic processes, such as the improved mapping of spatio-temporal evolution of shallow fault creep, is now possible with the improved temporal sampling of Sentinel 1 and size of the swaths. The challenges in this field can be synthesized into the abilities to perform near term, mid term and long term analysis, from a global scale to local scale. This issue is today associated intrinsically with the issue of computing capacity and information technology. The improved spatial and temporal coverage of Sentinel 1 is an asset. Nonetheless, we need an unprecedented computational capacity to be able to fully exploit the Sentinel 1 archive for the scope of repeat-time mapping of the displacement field of the Earth surface. On the one hand, this represents an opportunity to build and share computational capacity at a national or supranational scale. Embryonic initiatives in this field are ongoing today (2018). On the other hand, the need for important computational resources could be a handicap for a single university laboratory or independent researchers belonging to small albeit creative research units.

Complementary to Sentinel 1 InSAR, we plan to keep on using high spatial resolution SAR data such as the X band TerraSAR-X as well as the L band ALOS 2 PALSAR and the future NISAR. This data will be used in complement with the offset tracking methods applied both to SAR amplitude and to optical data, particularly Sentinel 2 and Landsat 8 for present and future events. The 2016 Kaikoura earthquake in New Zealand reminded us how InSAR line of sight alone is insufficient to measure the full 3D displacement field of an earthquake since the sensor is blind in the azimuth direction. Also a UP fault motion combined with a strike slip motion could compensate each other in the InSAR LOS signal. Therefore, combination of InSAR and offset tracking (SAR and optical) is essential.

The study sites will be the ones I am already involved in.

In collaboration with UPMC and extra-EU universities (Berkeley, Caltech) I will continue the investigation of the San Andreas fault at the transition between the Parkfield and the Cholame sections, because this area, thanks to the amount of accumulated knowledge and the instrumental coverage, is of major importance for studying the spatio-temporal evolution of the strain field in a fault zone. The North Anatolian Fault at the Ganos section, already investigated during the EU

MARSITE project, with the Bogazici University, Kandilli Observatory and Earthquake Research Institute, is another exceptional natural laboratory. New Zealand earthquakes, in particular those of the past decade in the south island, Kaikoura, Christchurch, Canterbury, constitute another puzzle for the next years, where I foresee fruitful collaboration with the New Zealand Institute of Geological and Nuclear Sciences (GNS science).

## 2) Multi temporal (differential) bathymetric measurements with Sentinel 2

This project is conceived for understanding dynamic bathymetry to support 1) underwater earthquake displacement measurements through differential bathymetry and underwater faults mapping 2) improved tsunami modelling through better estimation of near shore bathymetry 3) underwater depth measurements for bathymetric cinematic processes mapping.

Available satellite-based approaches for bathymetry retrieval provide accurate results only over very shallow waters (do not exceed 20 m), major limitations are imposed by the local environmental conditions (water turbidity, in particular). While several Earth Observation missions exist, the Copernicus Sentinel-2, operated by the European Space Agency (ESA), is a game changer. The Sentinel-2 mission comprises twin polar-orbiting satellites in the same orbit, phased at 180°. The satellite constellation carries optical instrument payload (MSI, Multi Spectral Imager) that sample 13 spectral bands. The major advantages of Sentinel-2 mission is its systematic monitoring over wide orbital swath width of 290 km, coupled with high revisit time (5 days at the equator and 2-3 days at mid-latitudes) and high spatial resolution (four multispectral bands at 10m). In this context, an innovative and robust method to retrieve maps of the coastal bathymetry from quasi simultaneous Sentinel-2 imagery is being developed from our team. The innovation of the approach is two folded and lies within the parameters considered for extraction of bathymetry and the Earth Observation (EO) data utilized. Our methodology allows to measure directly both swell celerities ( $c$ ) and swell wavelengths  $\lambda$  from a satellite optical dataset, where  $c$  and  $\lambda$  are jointly used in an inversion procedure to retrieve robustly the depth of the coastal seafloor. Swell celerity describes the phase velocities of superimposed ocean waves, each of which has a particular wavelength (*i.e.* the distance between two successive crests). As swell velocity and wavelength are controlled by bathymetry, quantifying these parameters from space allows for robust retrieval of water depths independently of water turbidity, which usually hampers our capacity for robust measurements or limits the maximum reachable water depths. Furthermore, it is the Sentinel-2 mission characteristics of unprecedented spatial coverage, short temporal repeatability and systematic acquisitions at sufficient resolution, which pave the way for advanced scientific developments. The combination of the above mentioned specifications, an innovative scalable approach and the availability of systematically acquired and archived satellite data, would possibly allow for routine bathymetric

mapping of shallow-depth coastal areas at global scale. The method preferably applies to the zone between the coast and an area of depth less than or equal to half the wavelength of the waves (up to a hundred meters deep maximum), with the exception of the wave breaking zone. Thus, it extends considerably our previous capability for monitoring coastal regions’ dynamics.

### 3) Volcanic clouds.

Within the broad topic of volcanology, besides volcano deformation, I foresee to develop a research axis on the remote sensing of volcanic clouds. Still, the understanding of the link between the pressure in the magmatic chamber and volcanic plume injection heights need to be quantified and, on the other side, how the injection height influences dispersion of volcanic cloud particles and local (or global ?) climate is an interesting and new research topic that merit to be investigated further. In this context, we have developed two original remote sensing approaches. The first, investigates the detection of volcanic plumes in cloudy sky conditions based on SAR data. The second extracts a digital elevation model of a given volcanic plume, based on the stereoscopy of quasi synchronous optical images. SAR detection of volcanic plumes is based on the Doppler anomalies induced on the SAR signal by volcano-related phenomena, during the SAR focusing. This method, improved during the MIAVITA, APHORISM and MEDSUV projects, has the potential to detect volcanic clouds in cloudy sky conditions. As every young methodology and given the sparse exploitable SAR acquisitions, it needs to be assessed further. Notably, we need to assess the topographic contribution to the sub-aperture Doppler shift as a potential source of errors. Besides, many kinematic phenomena related to an eruptive volcano are potentially a source of SAR Doppler shifts; notably lahars, particle motions in the atmosphere, plume refraction properties. Today, we need to develop robust procedures to discriminate among these different phenomena. For this, we need to increment the number of exploitable SAR observations and to have also a strategy for ground data acquisition and ground truth, which will require focusing our effort on specific targets during the development of the methods. One of those targets will be Etna, the most active volcano in Europe. The frequent repeat cycle of Sentinel 1 will help in this sense as well as the combined SAR acquisitions from multiple sensors, present-day and future constellation of microsatellites missions.

In terms of optical data, there is a need to study the technical characteristics of the focal planes of different past, present day and near-future sensors to extract plume elevation models (PEMs). On this subject, the improved repeat cycle of Sentinel 2 data is potentially an asset for temporally dense plume height measurements. Dense measurements, by combining multiple sensors acquisitions, are crucial in volcano monitoring. Collaboration in this field is foreseen with ENS Paris, University of Oxford, INGV Roma-Catania, the Icelandic meteorological office and the University of Reykjavik.



## 6. CITED BIBLIOGRAPHY

- Aarnes, J.E. , H.E. Krogstad, “Partitioning sequences for the dissection of directional ocean wave spectra: A review,”. Part of work package 4 (WP4) of the EnviWave (EVG-2001-00017) research programme under the EU Energy, Environment and Sustainable Development programme, 2001.
- Abileah, R., 2011, “Methods for mapping depth and surface current”, USA Patent Application, N°: 13091345, filed April 21, 2011.
- Abileah, R., 2013 “Mapping near shore bathymetry using wave kinematics in a time series of WorldView-2 satellite images” presented at *IGARSS*, Melbourne, Austria, July 21-26, 2013.
- Arason, P., Bjornsson, H., Petersen, G. N., Jónasdóttir, E. B., & Oddsson, B. (2015). Plume height during the 2014-2015 Holuhraun volcanic eruption. *Proceedings of the European Geosciences Union, General Assembly 2015*, EGU2015-11498, Vienna, Austria, 12–17 April 2015.
- Arason, P., Petersen, G. N., & Bjornsson, H. (2011). Observations of the altitude of the volcanic plume during the eruption of Eyjafjallajökull, April-May 2010. *Earth System Science Data*, 3, 9-17, doi:10.5194/essd-3-9-2011.
- Ardhuin, F., Collard, F., & Chapron, B., 2004. Wave Spectra from ENVISAT’s Synthetic Aperture Radar in Coastal Areas. Proceedings of the 14<sup>th</sup> (2004) International Offshore and Polar Engineering Conference, Toulon, France, May 23-28.
- Beal, R. C., Tilley, D. G., & Monaldo, F. M., 1983. Large and small scale spatial evolution of digitally processed ocean wave spectra from SEASAT Synthetic Aperture Radar. *J. Geophys. Res.*, 88, 1761-1778.
- Berthier, E., Vadon, H., Baratoux, D., Arnaud, A., Vincent, C., Feigl, K.L., Rémi, F., & Legrésy, B., 2005. Surface motion of mountain glaciers derived from satellite optical imagery. *Remote Sensing of Environment*, 95, 14-28.
- Binet, R., & Bollinger, L., 2005. Horizontal coseismic deformation of the 2003 Bam (Iran) earthquake measured from SPOT-5 THR satellite imagery. *Geophys. Res. Lett.*, 32(2), doi:10.1029/2004GL021897.
- Boccia, V., A. Renga, A. Moccia, S. Zoffoli, “Tracking of Coastal Swell Fields in SAR Images for Sea Depth Retrieval: Application to ALOS L-Band Data,” *IEEE Journal of selected topics in applied earth observations and remote sensing*, doi: 10.1109/JSTARS.2015.2418273.
- Booij, N., Ris, R.C., & Holthuijsen, L.H., 1999. A third-generation wave model for coastal regions, Part I, Model description and validation. *J. Geophys. Res.*, 104(C4), 7649-7666.
- Breit, H., M. Eineder, J. Holzner, H. Runge, and R. Balmer, “Traffic monitoring using SRTM Along-Track Interferometry,” Proceeding of the 2003 IEEE International Geoscience and Remote Sensing Symposium, 21-25 July, Toulouse, France, 2003.

- Breivik, L. A., Reistad, M., Schyberg, H., Sunde, J., Krogstad, H., & Johnsen, H., 1998. Assimilation of ERS SAR wave spectra in an operational wave model. *J. Geophys. Res.*, 103(C4), 7887-7900.
- Briole, P., De Natale, G., Gaulon, R., Pingue, F. and Scarpa, R., 1986, Inversion of geodetic data and seismicity associated with the Friuli earthquake sequence (1976–1977), Italy. *Annales Geophysicae*, 4B, pp. 481–492.
- Camus, G., A. Gourgaud, P.C. Mossand-Berthommier, and P. M. Vincent, “Merapi (Central Java, Indonesia): An outline of the structural and magmatological evolution, with a special emphasis to the major pyroclastic events,” *Journal of Volcanology and Geothermal Research*, vol. 100, pp.139–163, 2000.
- Capo, S., V. Marieu, D. Bru, B. Lubac, P. Bonneton, “Decadal morphodynamics evolution of a mixed-energy inlet using multispectral SPOT imagery,” *Coastal Dynamics*, pp. 283–294, 2013.
- Carboni, E., Grainger, R., Walker, J., Dudhia, A., & Siddans, R. (2012). A new scheme for sulphur dioxide retrieval from IASI measurements: application to the Eyjafjallajökull eruption of April and May 2010. *Atmospheric Chemistry and Physics*, 12, 11417–11434, doi:10.5194/acp-12-11417-2012.
- Chapron, B., Collard F., & Ardhin F., 2005. Direct measurements of ocean surface velocity from space: Interpretation and validation. *J. Geophys. Res.*, 110, doi:10.1029/2004JC002809.
- Chapron, B., Collard, F., & Kerbaol, V., 2004. Satellite Synthetic Aperture Radar sea surface Doppler measurements, in Proceedings of 2<sup>nd</sup> Workshop on Coastal and Marine Applications of Synthetic Aperture Radar, ESA SP-565, pp. 133– 141, Eur. Space Agency, Paris.
- Chuang, L. Z.- H. , L.- C. Wu, D.- J. Doong, C. C. Kao, “Two-dimensional continuous wavelet transform of simulated spatial images of waves on a slowly varying topography,” *Ocean Engineering*, vol. 35, no. 10, pp. 1039–1051, 2008.
- Collard, F., Arduin F., & Chapron B., 2005. Extraction of Coastal Ocean Wave Fields From SAR Images. *IEEE Journal of Oceanic Engineering*, 30(3), 526-533.
- Corradini, S., Merucci, L., Prata, A. J., & Piscini, A. (2010). Volcanic ash and SO<sub>2</sub> in the 2008 Kasatochi eruption: Retrievals comparison from different IR satellite sensors, *Journal of Geophysical Research*, 115, D00L21, doi:10.1029/2009JD013634.
- Costantini, M. and Rosen, P.A., 1999, A generalized phase unwrapping approach for sparse data. *Proceedings, IGARSS '99*, Hamburg, Germany, 28 June–2 July, 267–269.
- Crippen, R. E., 1992. Measurements of sub resolution terrain displacements using Spot panchromatic imagery. *Episodes*, 15, 56-61.
- Crocker, R. I., Matthews, D. K., Emery, W. J., & Baldwin, D. G., 2007. Computing Coastal Ocean Surface Currents From Infrared and Ocean Color Satellite Imagery. *IEEE Transactions on Geoscience and Remote Sensing*, 45(2).

- Cumming, I., G. Wong F., H., *In Digital Processing of Synthetic Aperture Radar*, Artech House, Norwood, Ma (USA), ed. 2005, ch 13, pp. 567-586.
- Dalrymple, R.A., A. Kennedy, J.T. Kirby, Q. Chen, "Determining depth from remotely sensed images", Proc. 26th International Conference on Coastal Engineering, Copenhagen, June 22-26, 2395-2408, 1998.
- de Michele M., & Briole, P., 2007. Deformation between 1989 and 1997 at Piton de la Fournaise volcano retrieved from correlation of panchromatic airborne images. *Geophys. J. Int.*, 169, 357–364, doi: 10.1111/j.1365-246X.2006.03307.x.
- de Michele M., Leprince S., Thiebot J., Raucoules D., Binet R., Direct measurement of ocean waves velocity field from a single SPOT-5 dataset, *Remote Sensing of Environment*, 119, 266-271 (2012).
- de Michele M., Raucoules, D., Aochi, H., Baghdadi, N., & Carnec, C., 2008. Measuring coseismic deformation on the northern segment of the Bam-Baravat escarpment associated with the 2003 Bam (Iran) earthquake, by correlation of very-high-resolution satellite imagery. *Geophys. J. Int.*, 173(2), 459-464.
- de Michele, M., D. Raucoules, and P. Arason (2016), Volcanic plume elevation model and its velocity derived from Landsat 8, *Remote Sens. Environ.*, 176, 219–224.
- de Michele, M., D. Raucoules, C. Lasserre, E. Pathier, Y. Klinger, J. Van Der Woerd, J. de Sigoyer, X. Xu, The Mw 7.9, 12 May 2008 Sichuan earthquake rupture measured by sub-pixel correlation of ALOS PALSAR amplitude images, *Earth Planets Space*, doi:10.5047/eps.2009.05.002, in press (2010).
- DeBella-Gilo M., & Kaab A., 2011. Sub-pixel precision image matching for measuring surface displacements on mass movements using normalized cross-correlation. *Remote Sensing of Environment*, 115, 130-142.
- Delacourt, C., Allemand, P., Casson, B., & Vadon, H., 2004. Velocity field of « La Clapiere » landslide measured by correlation of aerial and Quickbird satellite images. *Geophys. Res. Lett.*, 31, L15619.
- DeMets, C., Gordon, R.G., Argus, D.F. and Stein, S, 1990, Current plate motions. *Geophysical Journal International*, 101, pp. 425–478.
- Dobson, F. W., & Vachon, P. W., 1994. The Grand Banks ERS-1 SAR wave spectra validation experiment: program overview and data summary. *Atmosphere-Ocean*, 32(1), 7-29.
- Dominguez, S., Avouac, J.P., & Michel, R., 2003. Horizontal coseismic deformation of the 1999 Chi-Chi earthquake measured from SPOT satellite images: implications for the seismic cycle along the western foothills of central Taiwan, *J. Geophys. Res.*, 108, B2 2083 doi:10.1029/2001JB000951.
- Donelan, M. A., W. M. Drennan, A. K. Magnusson, "Non-stationary analysis of the directional properties of propagating waves," *Journal of Physical Oceanography*, vol. 26, pp. 1901–1914, 1996.

- Dugan J. P., Suzukawa H. H., Forsyth C. P., & Faber M. S., 1996. Ocean Wave Dispersion Surface Measured with Airborne IR Imaging Systems. *IEEE Transactions on Geoscience and Remote Sensing*, 14(5), 1282-1284.
- Dugan, J. P., & C. C. Piotrowski, 2003. Surface current measurements using airborne visible image time series. *Remote Sensing of Environment*, 84, 2, 309-319.
- Emery, W. J., Thomas, A. C., & Collins, M. J., 1986. An Objective Method for Computing Advective Surface Velocities From Sequential Infrared Satellite Images. *Journal of Geophysical Research*, 91(C11), 12,865-12,878.
- EMSC, 2011, Mw 5.1 LORCA (Spain) on May 11th 2011 at 16:47 UTC. Available online at [www.emsc-csem.org](http://www.emsc-csem.org) (accessed July 2011).
- ESA, 2011, Implementation of Envisat extension orbit in October 2010. Available online at <http://envisat.esa.int> (accessed online July 2011)
- Feng, X. , Y. Yan, W. Zhang, “Application of two-dimensional wavelet transform in near-shore X-band radar images,” *J. of Hydrodynamics*, vol. 23, no. 2, pp. 179–186, 2011.
- Ferretti A., C. Prati, F. Rocca, Permanent scatterers in SAR interferometry, *IEEE Trans. On Geoscience and Remote Sensing*, 39, 1, 8-20, 2001.
- Fialko Y., D. Sandwell, M. Simons, P. Rosen, Three dimensional deformation caused by the Bam, Iran, earthquake and the origin of shallow slip deficit, *Nature*, 435/19, 295-299, 2005.
- Frontera, T., Concha, A., Blanco, P., Echeverria, A., Goula, X., Arbiol, R., Khazaradze, G., Perez, F., and Surinach, E., 2011, DInSAR coseismic deformation of the May 2011 Mw 5.1 Lorca earthquake, (Southern Spain). *Solid Earth*, 3, pp. 111-119.
- Galindo-Zaldívar, J., González-Lodeiro, F. and Jabaloy, A., 1993, Stress and paleostress in the Betic-Rif cordilleras (Miocene to the present). *Tectonophysics*, 227, pp. 105–126.
- Garcia, C. A. E., & Robinson, I. S., 1989. Sea Surface Velocities in Shallow Seas Extracted From Sequential Coastal Zone Color Scanner Satellite Data. *Journal of Geophysical Research*, 94(C9), 12,681-12,691.
- Gelpi C. G., Shuraytz B. C. & Husman, M. E., 2001. Ocean wave height spectra computed from high-altitude, optical infrared images. *Journal of Geophysical Research*, 106(C11), 31403-31413.
- Gertisser, R., S. J. Charbonnier, V.R. Troll, J. Keller, K. Preece, J.P. Chadwick, J. Barclay, and R.A. Herd, “Merapi (Java, Indonesia): anatomy of a killer volcano,” *Geology Today*, vol. 27, no. 2, pp. 57-62, 2011.
- Gettelman, A., Schmidt, A., & Kristjánsson, J. E. (2015). Icelandic volcanic emissions and climate. *Nature Geoscience*, 8, 243, doi:10.1038/ngeo2376.
- Giner-Robles, J. L., Perez-Lopez, R., Silva Barroso, P., Rodriguez-Pascua, M. A., Martin-Gonzalez, F. and Cabanas, L., 2012, Analisis estructural de danos orientados en el terremoto de Lorca del 11 de

- mayo de 2011. Aplicaciones en arqueosismología. *Boletín Geológico y Minero*, 123, pp. 503-513, ISSN: 0366-0176
- González, P. J., Tiampo, K. F., Palano, M., Cannavó, F. and Fernández J., 2012, The 2011 Lorca earthquake slip distribution controlled by groundwater crustal unloading, *Nature Geoscience*, 5, pp. 821–825, doi:10.1038/ngeo1610.
- González, P.J. and Fernández, J., 2011, Drought-driven transient aquifer compaction imaged using multitemporal satellite radar interferometry. *Geology*, 39, pp. 551–554.
- Gorman, R. M., D. M. Hicks, “Directional wavelet analysis of inhomogeneity in the surface wave field from aerial laser scanning data,” *Journal of Physical Oceanography*, vol. 35, pp. 949–963, 2005.
- Gray, A., L. Mattar, and K. E. Sofko, “Influence of Ionospheric Electron Density Fluctuations on Satellite Radar Interferometry,” *Geophys. Res. Lett.*, vol. 27, no. 10, pp. 1451-1454, 2000.
- Haddadi, B., Moune, S., Sigmarsson, O., Gauthier, P.-J., & Gouhier, M. (2015). Pre-eruptive volatile and erupted gas phase characterization of the 2014 basalt of Bárðarbunga volcanic system, Iceland. *Proceedings of the European Geosciences Union, General Assembly 2015*, EGU2015-9572, Vienna, Austria, 12–17 April 2015.
- Hampson, R. W. , J. T. Kirby, J. H. Mac Mahan, “Video-based nearshore depth inversion using WDM method,” Center for applied coastal research, University of Delaware, Research Report CACR-08-02, 101 p, 2008.
- Hanssen, R. F., Radar Interferometry Data Interpretation and Error Analysis, Remote Sensing and Digital Image Processing Series, Volume 2, Kluwer Academic Publishers, The Netherlands, ISBN 0-7923-6945-9, 2001.
- Holland, T. K., “Application of the linear dispersion relation with respect to depth inversion and remotely sensed imagery,” *IEEE Transactions on Geoscience and Remote Sensing*, vol. 39, no. 11, pp. 2060–2071, 2001.
- Holman, R., N. Plant, T. Holland, “cBathy: A robust algorithm for estimating nearshore bathymetry,” *Journal of geophysical research. Oceans*, vol. 118, no. 5, pp. 2595–2609, 2013.
- Hooper, A. J., Persistent Scatterers Radar Interferometry for crustal deformation studies and modeling of volcanic deformation, Ph.D dissertation of the Stanford University (USA), 124 pages, AAT 3219289, ISBN 9780542706905, Nov 2006.
- Houlié, N., P. Briole, A. Nercessian, M. Murakami, “Sounding the plume of the 18 August 2000 eruption of Miyakejima volcano (Japan) using GPS,” *Geophys. Res. Lett.*, vol. 32, doi:10.1029/2004GL021728, 2005.
- Hreinsdottir, S., Sigmundsson, F., Roberts, M. J., Bjornsson, H., Grapenthin, R., Arason, P., Arnadottir, T., Holmjarn, J., Geirsson, H., Bennett, R. A., Gudmundsson, M. T., Oddsson, B., Ofeigsson, B. G.,

- Villemin, T., Jonsson, T., Sturkell, E., Hoskuldsson, A., Larsen, G., Thordarson, T., & Oladottir, B. A. (2014). Volcanic plume height correlated with magma pressure change at Grímsvötn volcano, Iceland. *Nature Geoscience*, 7, 214–218, doi:10.1038/ngeo2044.
- Johannessen, J. A., Chapron, B., Collard, F., Kudryavtsev, V., Mouche, A., Akimov, D., & Dagestad, K. F., 2008. Direct ocean surface velocity measurements from space: Improved quantitative interpretation of Envisat ASAR observations. *Geophysical Research Letters*, 35 (L22608), doi:10.1029/2008GL035709.
- Kääb, A., & Leprince, S. (2014). Motion detection using near-simultaneous satellite acquisitions. *Remote Sensing of Environment*, 154, 164–179, doi:10.1016/j.rse.2014.08.015.
- Kääb, A., & Prowse, T., 2011. Cold-regions river flow observed from space. *Geophysical Research Letters*, 38, (L08403), doi:10.1029/2011GL047022.
- Kääb, A., Lamare, M., & Abrams, M. (2013). River ice flux and water velocities along a 600 km-long reach of Lena River, Siberia, from satellite stereo. *Hydrology and Earth System Sciences*, 17, 4671–4683, doi:10.5194/hess-17-4671-2013.
- Kanamori, H., 1977, The energy released in great earthquakes. *Journal of Geophysical Research*, 82, pp. 2981–2987.
- Klinger Y., Michel, R., & King, G. C. P., 2006. Evidences for an earthquake barrier model from Mw ~7.8 Kokoxili (Tibet) earthquake slip distribution. *Earth and Planetary Science Letters*, 242, 354-364.
- Knight, E. J., & Kvaran, G. (2014). Landsat–8 operational land imager design, characterization, and performance. *Remote Sensing*, 6, 10286–10305, doi:10.3390/rs61110286.
- Larouche P., & Lavoie A., 1996. La télédétection appliquée à l’étude des océans. In F. Bonn (Ed.), *Précis de Télédétection, Vol. 2, Application Thématiques* (pp. 347-392). Quebec ; Presses de L’Université du Québec.
- Latry C., Rougé, B., & Baillarin, S., 2001. La chaîne d’image SPOT5 THR: un exemple d’optimisation globale. 18<sup>e</sup> Colloque sur le traitement du signal et des images, Groupe d’Etudes du Traitement du Signal et des Images (GRETSI), Toulouse, France, p184-187 (in French).
- Le Mouélic, S., Raucoules, D., Carnec, C. and King, C., 2005, A least-squares adjustment of multi-temporal InSAR data: application to the ground deformation of Paris. *Photogrammetric Engineering and Remote Sensing*, 71, pp. 197–204.
- Leprince, S., Barbot, S., Ayoub, F., & Avouac, J.-P. (2007). Automatic and precise orthorectification, coregistration, and subpixel correlation of satellite images, application to ground deformation measurements. *IEEE Transactions on Geoscience and Remote Sensing*, 45, 1529–1558, doi:10.1109/TGRS.2006.888937.

- Leu, L. H. Chang, “Remotely sensing in detecting the water depths and bed load of shallow waters and their changes,” *Ocean Eng.*, vol. 32, pp. 1174–1198, 2005.
- Lopez-Comino, J. A., Mancilla, F.L., Morales, J., Stich, D., 2012, Rupture directivity of the 2011, Mw 5.2 Lorca earthquake (Spain). *Geophysical Research Letters*, 39, doi:10.1029/2011GL050498.
- Mai S., & Latry C., 2009. Digital Elevation Model computation with SPOT5 panchromatic and multispectral images using low stereoscopic angle and geometric model refinement. Proceedings of the 2009 IEEE international Geoscience and Remote Sensing Symposium, 12-17 July, Cape Town, South Africa.
- Martinez-Diaz, J. J., Alvarez-Gomez, J. A., Garcia-Mayordomo, J., Insua-Arevalo, J. M., Martin-Gonzalez, F. and Rodriguez-Peces, M. J., 2012b, Interpretacion tectonica de la fuente del terremoto de Lorca de 2011 (MW 5,2) y sus efectos superficiales. *Boletín Geológico y Minero*, 123, pp. 441-458, ISSN: 0366-0176.
- Martínez-Díaz, J. J., Bejar-Pizarro, M., Álvarez-Gómez, J. A., Mancilla, F. de L., Stich, D., Herrera, G. and Morales, J., 2012., Tectonic and seismic implications of an intersegment rupture: The damaging May 11th 2011 Mw 5.2 Lorca, Spain, earthquake. *Tectonophysics*, 546-547, pp. 28-37. doi:10.1016/j.tecto.2012.04.010.
- Martinez-Diaz, J., 2002, Stress field variation related to fault interaction in a reverse oblique-slip fault: the Alhama de Murcia fault, Betic Cordillera, Spain. *Tectonophysics*, 356, pp. 291–305.
- Masana, E., Martinez-Diaz, J.J., Hernández-Enrile, J.L., and Santanach, P., 2004, The Alhama de Murcia fault (SE Spain), a seismogenic fault in a diffuse plate boundary: seismotectonic implications for the Ibero-Magrebien region. *Journal of Geophysical Research*, 109, doi:10.1029/2002JB002359.
- Massonnet, D. and Feigl, K.L., 1998, Radar interferometry and its application to changes in the Earth’s surface. *Review of Geophysics*, 36, pp. 441–500.
- Massonnet, D., Giros A., & Breton E., 1997. Forming Digital Elevation Models from single pass Spot data : results on a test site in the Indian Ocean. Proceedings of the 1997 IEEE international Geoscience and Remote Sensing Symposium, 03-08 August, Singapore.
- Massonnet, D., M. Rossi, C. Carmona, F. Adragna, G. Peltzer, K. Feigl, T. Rabaute, The displacement field of the Landers earthquake mapped by radar interferometry, *Nature*, 364, 138-142, 1993.
- Mastin, L. G., Guffanti, M., Servranckx, R., Webley, P., Barsotti, S., Dean, K., Durant, A., Ewert, J. W., Neri, A., Rose, W. I., Schneider, D., Siebert, L., Stunder, B., Swanson, G., Tupper, A., Volentik, A., & Waythomas, C. F. (2009). A multidisciplinary effort to assign realistic source parameters to models of volcanic ash–cloud transport and dispersion during eruptions. *Journal of Volcanology and Geothermal Research*, 186, 10–21, doi:10.1016/j.jvolgeores.2009.01.008.

- Matthews, J. P., & Awaji, T., 2010. Synoptic mapping of internal-wave motions and surface currents near the Lombok Strait using the Along Track Stereo Sun Glitter technique. *Remote Sensing of Environment*, 114(8), 1765-1776.
- Matthews, J., 2005. Stereo Observation of Lakes and Coastal zones using ASTER imagery. *Remote Sensing of Environment*, 99, 16-30.
- Meijninger, B.M.L. and Vissers, R.L.M., 2006, Miocene extensional basin development in the Betic Cordillera, SE Spain, revealed through analysis of the Alhama de Murcia and Crevillente Faults. *Basin Research*, 18, doi:10.1111/j.1365-2117.2006.00308.x.
- Meyer, F., Performance Requirements for Correction of Ionospheric Signals in L-band SAR Data, 3rd ALOS Joint PI Symposium, 9-13 Nov. 2009, Kona, USA.
- Michel R., & Avouac, J. P., 2002. Deformation due to the 17 August 1999 Izmit, Turkey, earthquake measured from SPOT images. *Journal of Geophysical Research*, 107(B4), doi:10.1029/2000JB000102.
- Michel, R., & Avouac, J. P., 2006. Coseismic surface deformation from air photos: The Kickapoo step over in the 1992 Landers rupture. *J. Geophys. Res.*, 111(B03408), doi: 10.1029/2005JB003776.
- Michel, R., E. Rignot, Flow of Glaciar Moreno, Argentina, from repeat-pass Shuttle Imaging Radar images: a comparison of the phase correlation method with radar interferometry. *J. Glaciol.* 45, 93-100, 1999.
- Michel, R., J. P. Avouac, J. Taboury, Measuring ground displacements from SAR amplitude images: Application to the Landers earthquake, *Geophys. Res. Lett.*, vol. 26, no. 7, pp. 875–878, Apr. 1999.
- Michel, R., J.P. Avouac,. “Deformation due to the 17 August 1999 Izmit, Turkey, earthquake measured from SPOT images,” *Journal of Geophysical Research*, vol 107(B4), doi:10.1029/2000JB000102., 2002.
- Necsoiu, M., Leprince, S., Hooper, D. M., Dinwiddie, C. L., McGinnis, R. N., & Walter, G. R., 2009. Monitoring migration rates of active subarctic dune field using optical imagery. *Remote Sensing of Environment*, 113, 2441-2447.
- Nocquet, J.M. and Calais, E., 2003, Crustal velocity field of Western Europe from permanent GPS array solutions, 1996–2001. *Geophysical Journal International*, 154, pp. 72–88.
- Okada, Y., 1985. Surface deformation due to shear and tensile faults in a half space. *Bulletin of the Seismological Society of America*, 75, pp. 1135–1154.
- Oppenheimer, “The 2010 explosive eruption of Java’s Merapi volcano – a “100-year” event,” *Jorunal of Volcanology and Geothermal Research*, in press, doi: 10.1016/j.jvolgeores.2012.06.018, 2012.
- Petersen, G. N., Bjornsson, H., Arason, P., & von Löwis, S. (2012). Two weather radar time series of the altitude of the volcanic plume during the May 2011 eruption of Grímsvötn, Iceland. *Earth System Science Data*, 4, 121–127, doi:10.5194/essd-4-121-2012.

- Piotrowski, C. C., J. P. Dugan, “Accuracy of Bathymetry and Current Retrievals From Airborne Optical Time-Series Imaging of Shoaling Waves,” *IEEE Transactions on Geoscience and Remote Sensing*, vol. 40, no. 12, pp. 2606-2618, 2002.
- Plant, N. G., K. T. Holland, Haller, M. C. “Ocean Wavenumber Estimation from Wave-Resolving Time Series Imagery,” *IEEE Transactions on Geoscience and Remote Sensing*, vol. 46(9), pp. 2644–2658, 2008.
- Plant, W.J., & Keller, W. C., 1990. Evidence of Bragg scattering in microwave Doppler spectra of sea return. *Journal of Geophysical Research*, 95(C9), 16299-16310.
- Pleskachevsky, A., S. Lehner, “Estimation of Underwater Topography using Satellite High Resolution Synthetic Aperture Radar Data,” in *Proc. of 4e TerraSAR-X Meeting*, Oberpfaffenhofen, Germany, 14–16 Feb. 2011, pp. 1–19.
- Populus, J., Aristaghes, C., Jonsson, J L., Augustin, J. M., & Pouliquen, E., 1991. The Use of SPOT Data for Wave Analysis. *Remote Sensing of the Environment*, 36, 55 – 65.
- Poupardin, A., Idier, D., de Michele, M., & Raucoules, D. (2015). Water depth inversion from a single SPOT-5 dataset. *IEEE Transactions on Geoscience and Remote Sensing*, accepted for publication.
- Poupardin, A., M. de Michele, D. Raucoules, D. Idier, 2014, “Water depth inversion from satellite dataset,” presented at *IGARSS*, Québec City, Canada, July 13-18, 2014.
- Raucoules, D., de Michele, M., Malet, J.-P., Ulrich, P. Time-variable 3D ground displacements from high-resolution synthetic aperture radar (SAR). Application to La Valette landslide (South French Alps). *Remote Sens. Environ* 2013, 139, 198–204.
- Raucoules, D., M. de Michele, “Assessing ionospheric influence on L-band SAR data: Implications on co seismic deformation measurements of the 2008 Sichuan Earthquake,” *Geosciences and Remote Sensing Letters*, vol. 7, no. 2, pp. 286-290, 2011.
- Riazanoff S., 2002. Spot Geometry Handbook, 74 pages, ed. SPOT-IMAGE, 5 rue des Satellites, 31030 Toulouse Cedex 4, France, January 2002.
- Ris, R.C., Booij, N., & Holthuijsen, L. H., 1999. A third-generation wave model for coastal regions, Part II, Verification. *J. Geophys. Res.*, 104(C4), 7667-7681.
- Robock, A. (2000). Volcanic eruptions and climate. *Reviews of Geophysics*, 38, 191–219, doi:10.1029/1998RG000054.

- Scherler D., Leprince, S., & Strecker, M. R., 2008. Glacier-surface velocities in alpine terrain from optical satellite imagery - accuracy improvement and quality assessment. *Remote Sensing of Environment*, 112, 3806-3819.
- Scollo, S., Prestifilippo, M., Pecora, E., Corradini, S., Merucci, L., Spata, G., & Coltelli, M. (2014). Eruption column height estimation of the 2011–2013 Etna lava fountains. *Annals of Geophysics*, 57, S0214, doi:10.4401/ag-6396.
- Sigmundsson, F., Hooper, A., Hreinsdóttir, S., Vogfjörð, K. S., Ófeigsson, B., Heimisson, E. R., Dumont, S., Parks, M., Spaans, K., Guðmundsson, G. B., Drouin, V., Árnadóttir, T., Jónsdóttir, K., Gudmundsson, M. T., Högnadóttir, T., Fridriksdóttir, H. M., Hensch, M., Einarsson, P., Magnússon, E., Samsonov, S., Brandsdóttir, B., White, R. S., Ágústsdóttir, T., Greenfield, T., Green, R. G., Hjartardóttir, Á. R., Pedersen, R., Bennett, R., Geirsson, H., LaFemina, P., Björnsson, H., Pálsson, F., Sturkell, E., Bean, C. J., Möllhoff, M., Braidon, A., & Eibl, E. P. S. (2015). Segmented lateral dyke growth in a rifting event at Bárðarbunga volcanic system, Iceland. *Nature*, 517, 191–195, doi:10.1038/nature14111.
- Simpson, J. J., McIntire, T., Jin, Z., & Stitt, J. R. (2000). Improved cloud top height retrieval under arbitrary viewing and illumination conditions using AVHRR data. *Remote Sensing of Environment*, 72, 95–110, doi:10.1016/S0034-4257(99)00095-4.
- Sparks, R. S. J., Bursik, M. I., Carey, S. N., Gilbert, J. S., Glaze, L. S., Sigurdsson, H., & Woods, A. W. (1997). *Volcanic Plumes*. John Wiley & Sons, Chichester. 559 pp.
- Spinetti, C., Barsotti, S., Neri, A., Buongiorno, M. F., Doumaz, F., & Nannipieri, L. (2013). Investigation of the complex dynamics and structure of the 2010 Eyjafjallajökull volcanic ash cloud using multispectral images and numerical simulations, *Journal of Geophysical Research – Atmospheres*, 118, 4729–4747, doi:10.1002/jgrd.50328.
- Splinter, K. D., R. A. Holman, “Bathymetry Estimation From Single-Frame Images of Nearshore Waves,” *IEEE Transactions on Geosciences and Remote Sensing*, Vol. 47, N. 9, pp. 3151-3160, 2009.
- Storey, J., Choate, M., & Lee, K. (2014). Landsat–8 operational land imager on-orbit geometric calibration and performance. *Remote Sensing*, 6, 11127–11152, doi:10.3390/rs6111127.
- Strozzi, T., A. Luckman, T. Murray, U. Wegmuller, C.L. Werner, Glacier motion estimation using SAR offset-tracking procedures, *IEEE Transactions on Geoscience and Remote Sensing*, 40, 11, 2384 - 2391, 2002.

- Su, H., H. Liu, L. Wang, A. M. Filippi, W. D. Heyman, R. A. Beck, “Geographically Adaptive Inversion Model for Improving Bathymetric Retrieval From Satellite Multispectral Imagery,” *IEEE Transactions on Geoscience and Remote Sensing*, vol. 52, pp. 465-476, 2013.
- Surono, P. Jousset, J. Pallister, M. Boichu, M-F Buongiorno, A. Budisantoso, F. Costa, S. Andreastuti, F. Prata, D. Schneider, L. Clarisse, H. Humaida, S. Sumarti, C. Bignami, J.. Griswold, S. Carn, and C. Tarantola, A. and Valette, B., 1982, Inverse problems: quest for information. *Journal of Geophysics*, 50, pp. 159–170.
- Thompson, D. R., Gotwols, B. L., & Keller, W. C., 1991. A comparison of Ku-band Doppler measurements at 20° incidence with predictions from a time-dependent scattering model. *J. Geophys. Res.*, 96(C3), 4947–4955.
- Tobita, M., Murakami, M., Nakagawa, H., Yarai, H., & Rosen, P.A., 2001. 3-D surface deformation of the 2000 Usu eruption measured by matching of SAR images. *Geophys. Res. Lett.*, 28, 4291-4294.
- Tolman, H. L., 1991. A third-generation model for wind waves on slowly varying, unsteady and inhomogeneous depths and currents. *J. Phys. Oceanogr.*, 21, 782-797
- Tolman, H. L., 2009. User manual and system documentation of WAVEWATCH III version 3.14. NOAA / NWS / NCEP / MMAB Technical Note 276, 194 pp.
- Urai, M. (2004). Sulfur dioxide flux estimation from volcanoes using Advanced Spaceborne Thermal Emission and Reflection Radiometer – a case study of Miyakejima volcano, Japan, *Journal of Volcanology and Geothermal Research*, 134, 1–13, doi:10.1016/j.jvolgeores.2003.11.008.
- Vadon, H., 2003. 3D Navigation over merged Panchromatic-Multispectral high resolution SPOT5 images. Proceedings of the 2003 ISPRS symposium, in The International Archives of the Photogrammetry, Remote Sensing and Spatial Information Sciences, Vol. XXXVI, 5/W10.
- Valade, S. and F. Donnadieu, “Ballistics and ash plumes discriminated by Doppler radar,” *Geophysical Research Letters*, 38, L22301, doi:10.1029/2011GL049415, 2011.
- Van Puymbroeck, N., Michel, R., Binet, R., Avouac, J.P., & Taboury, J., 2000. Measuring earthquakes from optical satellite images, *Applied Optics*, 39(20), 3486-3494.
- Vissers, R.L.M. and Meijninger, B.M.L., 2011, The 11 May 2011 earthquake at Lorca (SE Spain viewed in a structural-tectonic context. *Solid Earth*, 2, pp. 199-204.
- Wegmüller, U., C. Werner, T. Strozzi, and A. Wiesmann, “Ionospheric electron concentration effects on SAR and INSAR,” Proc. IGARSS 2006, Denver, Colorado, USA, 31- Jul. – 4. Aug., 2006.
- Werner, C., U. Wegmüller, T. Strozzi, and A. Wiesmann, “Gamma SAR and Interferometric Processing Software,” Proceedings of ERS-ENVISAT Symposium, Gothenburg, Sweden, 16-20 Oct, 2000.
- Werner, C., Wegmüller, U. and Strozzi, T., 2002, Processing strategies for phase unwrapping for InSAR applications. *Proceedings, EUSAR Conference*, June 4–6, Cologne, Germany, unpaginated CD-ROM.

Wu, L. C. , L. Z. H. Chuang, D. J. Doong, C. C. Kao, “Ocean remotely sensed image analysis using two-dimensional continuous wavelet transforms,” *Int. J. Remote Sens.*, vol. 32, no. 23, pp. 8779–8798, 2011.

7. EXEMPLAIRES des TRAVEAUX SCIENTIFIQUES publiés ou inédits (on usb key)